DEVELOPMENT AND CHARACTERISATION OF ALUMINA-TITANIUM CARBIDE CUTTING TOOLS

PhD Dissertation

Ahmet Oğuzhan TURHAN

Eskişehir 2025

DEVELOPMENT AND CHARACTERISATION OF ALUMINA-TITANIUM CARBIDE CUTTING TOOLS

Ahmet Oğuzhan TURHAN

PhD Dissertation

Department of Advanced Technologies

Programme in Nanotechnology

Supervisor: Prof. Dr. Alpagut KARA

Eskişehir

Eskişehir Technical University

Institute of Graduate Programs

August 2025

This thesis has been supported by the project TÜBİTAK, through the 2244 – Industrial PhD Fellowship Program with the project number 118C152, which is approved by the SRP Committee.

FINAL APPROVAL FOR THESIS

This thesis titled DEVELOPMENT AND CHARACTERISATION OF ALUMINA-TITANIUM CARBIDE CUTTING TOOLS has been prepared and submitted by Ahmet Oğuzhan TURHAN in partial fulfillment of the requirements in "Eskişehir Technical University Directive on Graduate Education and Examination" for the Degree of PhD in Advanced Technologies Department has been examined and approved on 11/08/2025.

Committee Members		**Title, Name and Surname**	**Signature**
Member	:	Prof. Dr. Alpagut KARA	
Member	:	Prof. Dr. Ferhat KARA	
Member	:	Prof. Dr. Hilmi YURDAKUL	
Member	:	Prof. Dr. Hakan GAŞAN	
Member	:	Assoc. Prof. Dr. Ali ÇELİK	

Prof. Dr. Harun BÖCÜK
Director of the Institute of Graduate Programs

11/08/2025

SUPERVISOR APPROVAL

PhD student Ahmet Oğuzhan TURHAN, whom I supervise, has completed this thesis titled DEVELOPMENT AND CHARACTERISATION OF ALUMINA-TITANIUM CARBIDE CUTTING TOOLS. According to my inspections, the work is scientifically and ethically appropriate for the student to the thesis defense exam.

Supervisor

Prof. Dr. Alpagut KARA

ABSTRACT

DEVELOPMENT AND CHARACTERISATION OF ALUMINA-TITANIUM CARBIDE CUTTING TOOLS

Ahmet Oğuzhan TURHAN

Department of Advanced Technologies

Programme in Nanotechnology

Eskişehir Technical University, Institute of Graduate Programs, August 2025

Supervisor: Prof. Dr. Alpagut KARA

This study focuses on the development and characterisation of Al_2O_3–TiC-based ceramic cutting tools produced with advanced sintering techniques. Alumina–titanium carbide composites were prepared with varying TiC and ZrO_2 contents and sintered under controlled Gas Pressure Sintering (GPS) conditions. The effects of rare earth oxide (REO) additives (Er_2O_3, Yb_2O_3, Y_2O_3, Sm_2O_3 and CeO_2) on densification, microstructure, hardness and fracture toughness were systematically investigated. Characterisation commercial products were analyzed for comparison. Microstructural characterisation was performed using SEM, EDS and XRD analyses, while mechanical properties were evaluated with hardness and fracture toughness tests. The results demonstrate that optimized compositions with appropriate REO additions and sintering parameters achieve improved densification and mechanical performance. This work provides insights into designing high-performance Al_2O_3–TiC cutting tools suitable for demanding machining applications.

Keywords: Alumina, Titanium carbide, Ceramic cutting tools, Gas pressure sintering, Rare earth oxide.

ÖZET

ALÜMİNA TİTANYUM KARBÜR KESİCİ UÇLARIN GELİŞTİRİLMESİ VE KARAKTERİZASYONU

Ahmet Oğuzhan TURHAN

İleri Teknolojiler Anabilim Dalı

Nanoteknoloji Bilim Dalı

Eskişehir Teknik Üniversitesi, Lisansüstü Eğitim Enstitüsü, Ağustos 2025

Danışman: Prof. Dr. Alpagut KARA

Bu çalışma, ileri sinterleme teknikleri kullanılarak üretilen Al_2O_3–TiC esaslı seramik kesici uçların geliştirilmesi ve karakterizasyonuna odaklanmaktadır. Farklı TiC ve ZrO_2 içeriklerine sahip kompozitler hazırlanarak Gaz Basınçlı Sinterleme (GPS) yöntemiyle sinterlenmiştir. Er_2O_3, Yb_2O_3, Y_2O_3, Sm_2O_3 ve CeO_2 gibi nadir toprak oksit katkılarının yoğunlaşma, mikro yapı, sertlik ve kırılma tokluğu üzerindeki etkileri sistematik olarak araştırılmıştır. Karşılaştırma amacıyla ticari ürünler de analiz edilmiştir. Mikroyapısal karakterizasyon SEM, EDS ve XRD analizleri ile gerçekleştirilmiş; mekanik özellikler sertlik ve kırılma tokluğu testleriyle değerlendirilmiştir. Sonuçlar, uygun nadir toprak oksit katkıları ve sinterleme parametreleriyle optimize edilen bileşimlerin daha iyi yoğunluk ve mekanik performans sağladığını göstermektedir. Bu çalışma, zorlu işleme uygulamaları için yüksek performanslı Al_2O_3–TiC kesici uç tasarımına yönelik önemli bilgiler sunmaktadır.

Anahtar Sözcükler: Alümina, Titanyum karbür, Seramik kesici uçlar, Gaz basınçlı sinterleme, Nadir toprak oksitleri.

ACKNOWLEDGEMENTS

I want to express my deepest gratitude to all the individuals and institutions who contributed to completing this dissertation.

First and foremost, I would like to thank the **TÜBİTAK 2244 Industrial PhD Fellowship Program** for their support, **MDA Advanced Ceramic Inc.** and its dedicated employees for their collaboration and the opportunities they provided through this study.

I sincerely thank my supervisor, **Prof. Dr. Alpagut Kara,** for his invaluable guidance and expertise. Also, grateful to **Prof. Dr. Ferhat Kara** and Assoc. **Prof. Dr. Ali Çelik** for their continuous support during this study.

I also extend my heartfelt thanks to my beloved **family**.

Above all, I am profoundly indebted to my dearest wife, **Ruken Turhan,** who stood by me through every challenge, kept my motivation alive and has been my greatest source of strength during my doctoral studies.

Ahmet Oğuzhan TURHAN

11/08/2025

STATEMENT OF COMPLIANCE WITH ETHICAL PRINCIPLES AND RULES

I hereby truthfully declare that this thesis is an original work prepared by me; that I have behaved in accordance with the scientific ethical principles and rules throughout the stages of preparation, data collection, analysis and presentation of my work; that I have cited the sources of all the data and information that could be obtained within the scope of this study, and included these sources in the references section; and that this study has been scanned for plagiarism with "scientific plagiarism detection program" used by Eskişehir Technical University, and that "it does not have any plagiarism" whatsoever. I also declare that, if a case contrary to my declaration is detected in my work at any time, I hereby express my consent to all the ethical and legal consequences that are involved.

Ahmet Oğuzhan TURHAN

CONTENTS

Page

LIST OF TABLES

Page

LIST OF FIGURES

Page

LIST OF IMAGES

Page

GLOSSARY OF SYMBOLS AND ABBREVIATIONS

Al_2O_3	:	Alumina
BN	:	Boron nitride
BUE	:	Built-up edge
CBN	:	Cubic boron nitride
CeO_2	:	Cerium oxide
CIP	:	Cold isostatic press
CMC	:	Ceramic matrix composite
EDS	:	Energy dispersive X-ray spectroscopy
Er_2O_3	:	Erbium oxide
GPS	:	Gas pressure sintering
HIP	:	Hot isostatic press
HP	:	Hot-press
HSS	:	High speed steel
MMC	:	Metal matrix composite
PCA	:	Process control agent
PMC	:	Polymer matrix composite
PSD	:	Particle size distribution
REO	:	Rare-earth oxide
SEM	:	Scanning electron microscopy
Si_3N_4	:	Silicon nitride
SiC	:	Silicon carbide
Sm_2O_3	:	Samarium oxide
SPS	:	Spark plasma sintering
TiC	:	Titanium carbide
TiN	:	Titanium nitride
XRD	:	X-ray diffraction
Y_2O_3	:	Yttrium oxide
Yb_2O_3	:	Ytterbium oxide
ZrO_2	:	Zirconia

1. INTRODUCTION

Advanced ceramics have become essential engineering materials due to their excellent mechanical strength, chemical stability and resistance to high temperatures and wear. Among these, alumina (Al_2O_3) stands out as a widely used ceramic for cutting tool applications thanks to its high hardness, good chemical inertness and relatively low cost. However, the inherent brittleness of monolithic alumina limits its widespread use under demanding machining conditions where fracture toughness is critical.

Composite systems that combine alumina with hard reinforcing phases have been extensively explored to overcome these limitations. Titanium carbide (TiC) is a particularly attractive reinforcement owing to its high hardness, excellent thermal stability and good chemical compatibility with alumina. Al_2O_3-TiC composites have improved toughness and wear resistance compared to pure alumina, making them suitable candidates for cutting tool inserts in metal machining.

However, the processing of Al_2O_3-TiC composites requires careful control of powder characteristics, forming methods and sintering conditions to achieve dense, homogeneous microstructures with minimal defects. Traditional sintering methods often struggle to fully densify these composites without excessive grain growth, which can deteriorate mechanical properties. Therefore, advanced sintering techniques, such as Hot Press (HP) and Spark Plasma Sintering (SPS), have achieved near-theoretical density with controlled microstructures.

Furthermore, minor additives, such as zirconia (ZrO_2), have been shown to influence grain boundary behavior, densification kinetics and mechanical properties.

Despite these advances, there is still a need for systematic studies that evaluate the combined effects of composition design, sintering parameters and additive incorporation on the microstructural and mechanical performance of Al_2O_3-TiC cutting tools. Such studies can provide critical insights into optimizing manufacturing routes for industrial applications.

This thesis focuses on the development and characterization of Al_2O_3-TiC-based cutting tools. The research systematically examines commercial characterisated products, investigates the influence of TiC and ZrO_2 content on composite properties and explores the effects of various rare earth oxide additives (Er_2O_3, Yb_2O_3, Y_2O_3, Sm_2O_3 and CeO_2) under controlled GPS sintering conditions. Through detailed microstructural analyses, density measurements and mechanical testing, hardness and fracture toughness

evaluations. This work aims to identify optimal compositions and processing routes for high-performance ceramic cutting tools.

1.1. Ceramic Materials

The word "ceramic" originates from the ancient Greek word *keramikos* (Callister Jr and Rethwisch, 2014) or *keramos* (Richerson and Lee, 2018), both meaning "burnt stuff." This term highlights that producing materials with desired characteristics often involves heat treatment at very high temperatures. The idea of ceramics goes back to ancient times when people mixed clay with water, formed it into shapes, dried it in the sun and then fired it. The hard and brittle material created through this process was the earliest form of ceramic, today known as "earthenware." (Richerson and Lee, 2018)

Ceramics are important as engineering materials because they are widely available in nature and have mechanical and physical properties different from those of metals (Groover, 2010). Ceramics can be defined as solid compounds composed of at least two elements, including one nonmetallic or metallic element, that are formed by applying heat or a combination of heat and pressure (Barsoum, 2020), (Callister Jr and Rethwisch, 2014). The atomic bonds in these compounds are either purely ionic or predominantly ionic with some covalent characteristics.

Ceramics can be grouped into two main types: traditional and advanced. Traditional ceramics are usually made from natural materials like clay, silica and feldspar. On the other hand, advanced ceramics are produced from pure or almost pure compounds such as alumina (Al_2O_3), silicon carbide (SiC) and silicon nitride (Si_3N_4) (Smith and Hashemi, 2019).

Traditional ceramics are generally hard and brittle, with low resistance to cracking and little flexibility. Advanced ceramics are even harder, stronger and more resistant to breaking. However, all ceramics have the common problem of low flexibility. Ceramics are usually very good at blocking electricity and heat. Also, their strong atomic bonds give them high melting points and stability in difficult environments (Smith and Hashemi, 2019).

1.2. Ceramic Processing

As shown in fig. 1.1, ceramics are processed differently depending on the microstructure and properties needed. Advanced ceramics start as fine powders pressed

and heated at high temperatures. This creates a uniform microstructure with very small grains, low porosity and few added materials. In ceramic matrix composites (CMCs), a second material—particles, whiskers, or fibers—is often added. These materials must be correctly aligned and protected during heating to prevent damage (Kulik et al., 2004). Because ceramic products are so varied, they require very specialized production methods, but they all begin with ceramic powders.

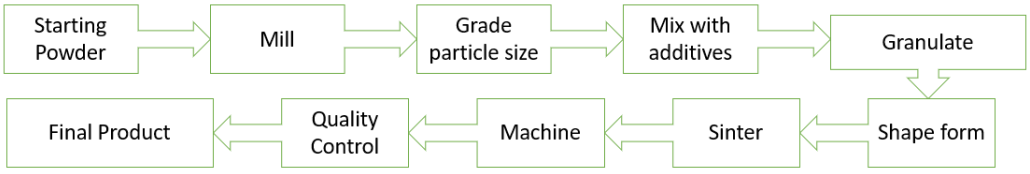

Figure 1.1. *Steps required to produce ceramics that meet the specifications of the intended applications. (Richerson and Lee, 2018)*

As shown in fig. 1.1, several steps and checks are needed between getting the starting powders and delivering the final product. At first, these powders usually do not have the right size or size distribution for the next steps. Therefore, they must be milled or heated (calcined) and then tested to ensure the correct size has been reached.

In many applications, having a uniform microstructure made of small grains is important. This microstructure depends on many factors, such as the composition of the starting powders, the size and distribution of the particles, how well the particles are packed and the time and temperature of the sintering process. These must be carefully checked to get the desired properties in the final product. As mentioned earlier, choosing the right material means matching the ceramic's properties and design to the application's needs. This choice affects the whole production process—from selecting the powder to using it in the product. Advanced ceramics often aim to have a strong microstructure with very fine grains. Even tiny impurities (at parts per million levels) can greatly affect the final product's properties.

1.2.1. Powder selection criteria

Powder processing is a very sensitive step. The raw material type strongly affects a ceramic part's final properties. Factors such as purity, particle size distribution, reactivity, availability and cost must all be carefully considered and managed.

High-temperature properties such as strength, resistance to breaking under stress and protection against oxidation are strongly affected by the material's purity. The impact of an impurity depends on its chemistry, how it interacts with the main material, how it is spread in the material and how the component is used (such as time, temperature, stress and environment). Impurities can greatly affect mechanical properties, but they may have an even bigger effect on electrical, magnetic and optical properties. These special properties are usually adjusted for specific uses by adding a small amount of another material, called a dopant, under strict control. Even small changes in the amount or position of the dopant can change the material's behavior. Likewise, unwanted contaminants can reduce the effect of the dopant and cause the device to work incorrectly.

The particle size distribution is important, depending on the shaping or consolidation method used. In most cases, the goal of consolidation is to pack the particles as closely as possible and keep the structure uniform. This helps reduce shrinkage and control porosity during densification. Using only one particle size does not pack the material efficiently. Even when particles are packed well, more than 30% of the space remains empty. Adding particles that fit into the largest spaces can reduce the space to 26%. Adding a third group of smaller particles can reduce the space to about 23%. Therefore, a mixture of different particle sizes is needed to achieve optimal particle packing.

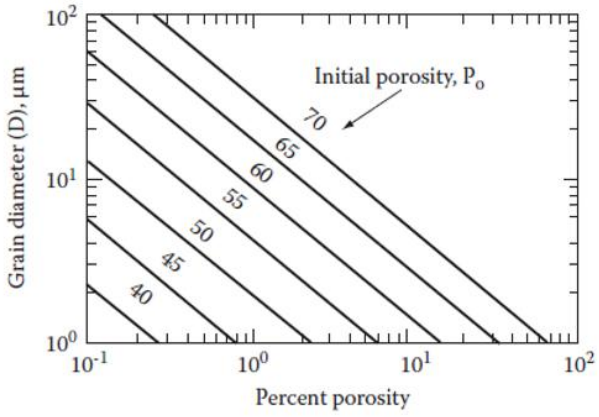

Figure 1.2. *Effects of porosity in the powder compact on the porosity and grain size of Al_2O_3 after densification. (Richerson and Lee, 2018)*

The reactivity of the starting powder is another important factor. When powder is heated, the change in surface energy helps the particles come closer and become denser.

Very small particles with a large surface area have high surface energy. Because of this, they try to reduce their surface area by joining together. Particles smaller than 1 μm can be pressed into a porous shape and then heated to reach a density close to the ideal. Almost all pores larger than 0.4 μm must be removed to achieve transparency after sintering. This is because light, which has a wavelength of around 0.4 to 0.8 μm, is scattered by these larger pores and cannot pass through. Using a highly reactive Al_2O_3 powder with an average particle size of 0.3 μm helps remove these larger pores and improves transparency.

The powder mixture's particle size distribution and reactivity are very important when deciding the temperature and how long it should be applied during sintering. In general, powders with smaller grains and larger surface area require lower temperatures and shorter times for densification. This can greatly affect the strength of the final product. However, keeping the material at high temperatures for too long can make the grains grow larger and reduce strength. Using powders that densify rapidly with minimal grain growth is preferable to achieve optimal strength.

1.2.2. Powder preparation

Controlling particle size and particle size distribution (PSD) is important to achieve optimal application properties. Each application has its own specific needs. For example, high-strength ceramics need very fine particles (usually around 1 μm) to create a microstructure with minimal defects. Refractory materials, which must handle high heat, often use a mix of large and small particles, some of which can be hundreds of microns wide. Abrasive materials must be made in many different sizes, with each size falling into a narrow range. Many methods have been developed to appropriately produce and classify powders to meet these needs.

1.2.2.1. Ball milling

In most cases, the desired particle size distribution (PSD) cannot be reached by only screening, classifying, or washing the raw material. It is often necessary to reduce the size of the particles, a process called comminution. One of the most widely used techniques is ball milling. In this method, the material to be ground (called the "charge") is placed into a rotating cylinder along with grinding tools such as balls, short cylinders, or rods (Lü L., 1995). As the cylinder turns, these tools move and crush the ceramic particles.

The particles are fractured as they become trapped between the moving tools or between the tools and the cylinder wall. This process is illustrated in the fig. 1.3.

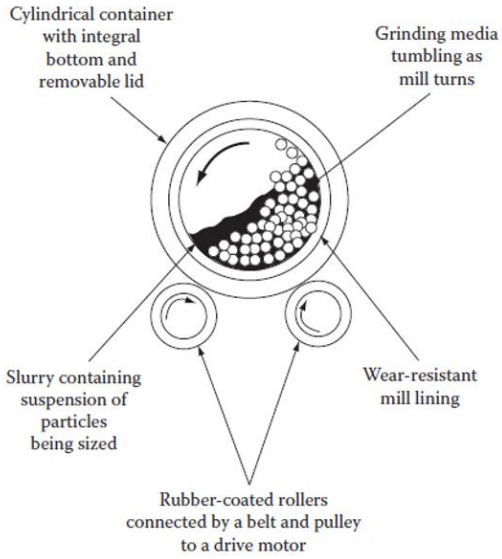

Figure 1.3. *Schematic cross-section showing the key elements of a typical ball mill. (Richerson and Lee, 2018)*

1.2.2.2. Planetary ball milling

A planetary ball mill is named after the planet-like movement of its vials. It is suitable for laboratory use because it only needs a small amount of powder— sometimes only a few grams. The vials are placed on a rotating support disk and spin on their axes. A special drive system creates this motion. Combining the spinning vials and the rotating disk creates centrifugal forces that act on the material and the grinding balls inside the vials. Since the vials and the disk move in opposite directions, the direction of the force changes repeatedly. This causes the grinding balls to first slide along the inside wall of the vial due to friction, then lift and move freely, hitting the opposite wall. The balls also collide increasing the grinding effect (Suryanarayana, 1999).

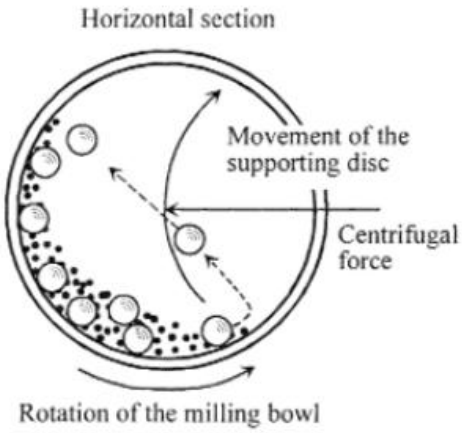

Figure 1.4. *A schematic view of the motion of the balls and powder mixture. (Richerson and Lee, 2018)*

1.2.2.3. Attrition milling

Fig. 1.5 illustrates the structure of an attrition mill. It is similar to a ball mill because it is also a cylinder with grinding balls or media inside. However, small balls are moved by stirring arms attached to a central shaft instead of the whole cylinder rotating. According to Herbell et al. (Herbell and Glasgow, 1978), attrition milling is faster than ball milling, produces finer particles and causes less contamination. It is also easy to use in different conditions—dry, wet, vacuum, or inert gas atmosphere.

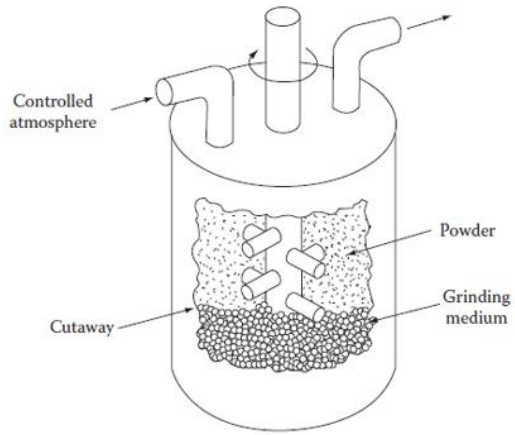

Figure 1.5. *Schematic of an attrition mill (Richerson and Lee, 2018)*

1.2.3. Process controlling agents

Additives are essential in the ceramic forming process. Ceramic powders need special treatment before shaping to create a uniform final product. When very ductile powder particles can stick together through cold welding during the milling process. To

reduce cold welding and stop the particles from clumping, process control agents (PCAs) are added during milling. PCAs can be either organic or inorganic. They are usually grouped into four main types: solvents, dispersants, binders and plasticizers (Suryanarayana, 2004).

Solvents are used to mix additives into the powder and to ensure their uniform distribution. Dispersants, also called deflocculants, increase the repelling forces between particles. This keeps the mixture stable and prevents the particles from sticking together. Binders are usually long-chain polymers. Their primary function is to strengthen the shaped but unfired ceramic (the green body) by forming bridges between particles. In certain shaping methods, binders also enhance flexibility. Plasticizers are organic substances with a lower molecular weight than binders. They soften the binder when it is dry, increasing the green body's flexibility. Organic additives are often used in advanced ceramics because they can be completely removed by heating before sintering (Rahaman, 2003).

1.2.4. Spray drying

Spray dryers are often used in ceramic production to make uniform and easy to handle powders. Fig. 1.6 illustrates a spray dryer equipped with a twin-fluid nozzle. Before drying, the powder is mixed with additives to form a slurry. This slurry enters the nozzle at low pressure through one outlet. At the same time, compressed gas (usually air) enters through the other outlet. The gas atomizes the liquid into small droplets. These droplets dry rapidly in hot air, forming soft, spherical granules. The size of the granules can be controlled by changing the air flow, the amount of slurry fed into the system and the thickness (viscosity) of the slurry (Richerson and Lee, 2018).

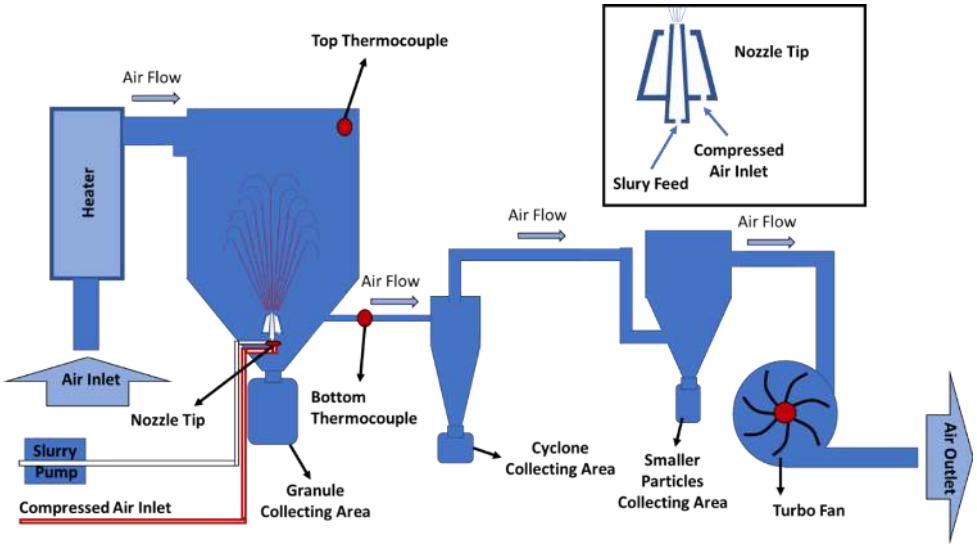

Figure 1.6. *Schematic view of a spray dryer equipped with a twin-fluid nozzle*

1.2.5. Shape forming processes

Most ceramic products are made using agglomerated (clustered) particles. The type of raw materials used depends on the final properties needed for the ceramic part. The powders and additives can be mixed either in dry or wet form. Mixing with water is common for products that do not require advanced performance characteristics, such as ordinary bricks. Sometimes, both wet and dry methods are used together. For example, in the production of high-alumina (Al_2O_3) insulators, the raw powders are mixed with water and a binder to create a slurry. This slurry is then spray-dried to form small, round particles.

Ceramic products made from agglomerated particles can be formed in different conditions—dry, plastic, or liquid—using various methods. Most ceramic forming methods are cold-forming processes, but there are also hot-forming techniques. Common methods to shape ceramics include pressing, slip casting and extrusion (Smith and Hashemi, 2019).

Table 1.1. *Feed materials and shapes of the green body for the common ceramic forming methods (Rahaman, 2003)*

Forming method	Feed material	Shape of green body
Die compaction	Powder or free-flowing granules	Small simple shapes
Isostatic pressing	Powder or fragile granules	Larger, more intricate shapes
Slip casting	Free-flowing slurry with low binder content	Thin intricate shapes
Extrusion	Moist mixture of powder and binder solution	Elongated shapes with uniform cross-section

Compaction is a high-pressure method of shaping powders into a desired form. The powder is placed in a mold (die) and pressed between two punches. This forms a part called a "green body," which means it has not yet been fully processed. The green body is denser than the loose powder but still weaker than the final sintered product. The pressure helps the particles move into a better arrangement with fewer gaps and more contact points. At higher pressures, the particles start to deform slightly, which increases contact and reduces pores. Different pressing methods are used to perform compaction, such as uniaxial and isostatic pressing. These methods require powders mixed with binders and lubricants to ensure proper flow and formability.

1.2.5.1. Uniaxial pressing

Uniaxial pressing is a method of shaping powders by applying pressure from one direction only. During this process a rigid punch presses the powder into a fixed mold (called a die). This method is performed using mechanical or hydraulic presses. Mechanical presses are more commonly used due to their higher operating speeds and ease of automation.

The process starts by placing the punches into the die to create a cavity. This cavity is filled with free-flowing powder, usually containing binders, moisture and lubricant. The powder is selected for its good flowability and ability to achieve uniform mold filling. First, light pressure is applied from both the top and bottom punches. This step removes air and slightly compacts the powder. Then, full pressure is applied and the punches move to a set position to form the final shape.

After compaction, the shaped part is pushed out of the die and the process starts again. Depending on the type of press and the part being made, this cycle can repeat 6 to 100 times per minute. Most presses used for this process can apply forces between 910

and 18,200 kilograms (1 to 20 tons). Some larger presses can reach up to 91,000 kilograms (100 tons) of force (Richerson and Lee, 2018).

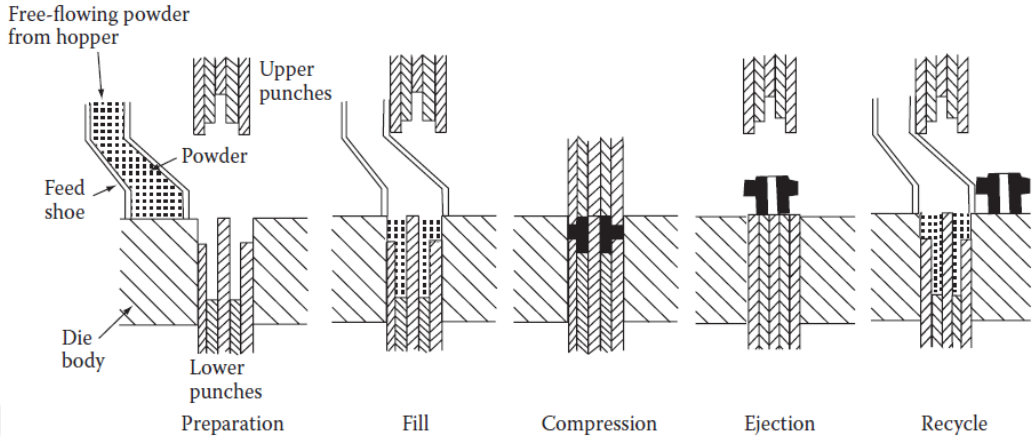

Figure 1.7. *Schematic illustrating automated uniaxial pressing (Kingery, 1963)*

1.2.5.2. Isostatic pressing

Certain limitations of uniaxial pressing can be addressed by applying pressure uniformly from all directions. This method is called isostatic pressing or cold isostatic pressing. It was developed to achieve more uniform compaction and improve shape formation (Richerson and Lee, 2018). The ceramic powder is placed in a flexible, airtight container—usually rubber. The container is placed in a chamber filled with hydraulic fluid. When pressure is applied, it exerts force uniformly on all sides of the container, resulting in even compaction of the powder. After compaction, the container is removed, yielding a ceramic part with a uniform shape (Smith and Hashemi, 2019).

Ceramics made by isostatic pressing are often used in products like refractories, bricks, spark plug insulators, radomes, carbide tools, crucibles and bearings. Although this method uses less extreme pressure than die compaction, it can cause problems like cracks or layer separation (delamination). These issues generally arise from "spring back", when the material slightly expands upon pressure release, particularly if the pressure is reduced too rapidly. (Rahaman, 2003)

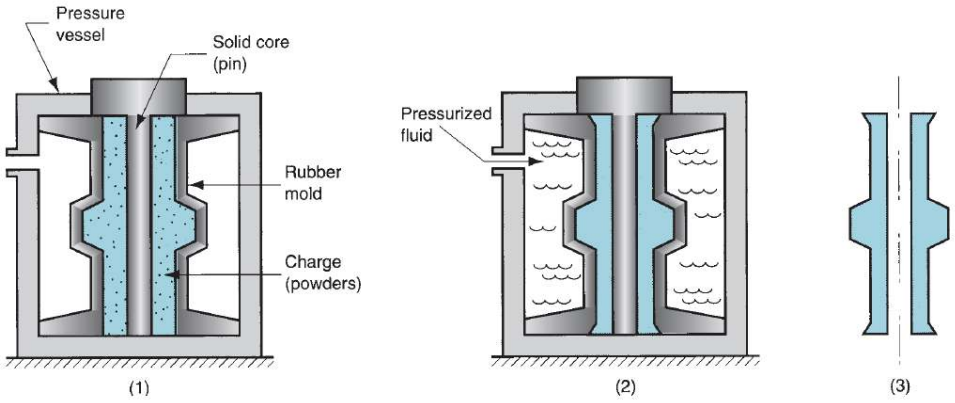

Figure 1.8. *Cold isostatic pressing: (1) powders are placed in the flexible mold; (2) hydrostatic pressure is applied against the mold to compact the powders; and (3) pressure is reduced and the part is removed. (Groover, 2010)*

1.2.6. Binder removal

Debinding is the process of removing organic additives and binders from the green body before sintering. This step is critical for removing binders while maintaining particle packing integrity. If any leftover materials or defects remain after debinding, they can affect how the ceramic structure forms during sintering. This can lead to weaker final properties in the ceramic part.

Debinding becomes particularly critical when the green body contains a high binder content. Three main methods are used for debinding: capillary extraction, solvent extraction and thermal decomposition. Thermal decomposition, also called thermal debinding, is the most common method due to its high effectiveness in binder removal (Groover, 2010).

In thermal debinding, the binder is removed as vapor by heating the green body at normal pressure. This can be done in an oxidizing or non-oxidizing atmosphere, or under partial vacuum. The process is affected by both chemical and physical factors. Chemically, the type of binder affects the temperature at which it breaks down and what gases are released. Physically, the success of binder removal depends on how well heat enters the body and how easily the gases from the binder can leave the material.

Binder systems usually include at least two different materials, each with its own evaporation rate and way of breaking down during heating. This process becomes more complex because the ceramic powder can also affect how the binder breaks down. As a result, the speed or success of binder removal may change depending on the ceramic material used (Rahaman, 2003).

1.2.7. Sintering

Ceramic processing presents challenges due to the heat resistance and brittleness of ceramics. Unlike glass, most ceramics are not made by melting but by using fine powders. These powders go through steps such as milling, mixing, shaping (molding) and finally heat treatment or firing to form strong, dense solids.

Sintering is critical in transforming compacted powder into a strong, dense ceramic through heating. After forming the green body, the powder particles touch each other but are not yet fully bonded. During sintering, the particles bond together, making the material denser and reducing or removing pores. This process usually occurs at 80% to 90% of the material's melting temperature (Groover, 2010). Sintering requires two essential conditions: a mechanism for material transport and sufficient energy to initiate and sustain this movement. (Richerson and Lee, 2018)

The sintering mechanism varies depending on the type of ceramic. Diffusion and viscous flow are the two main ways materials move during sintering. Heat provides the energy needed for these processes. In advanced ceramics, densification mostly happens through mass diffusion. In traditional ceramics, a glassy phase forms during heating, facilitating grain bonding.

During sintering, atoms or ions move (diffuse) along the edges of grains and from the inside of the material to the contact points between particles, called necks. This movement causes the pores to become smaller and the material to become denser. Also, atoms or ions can evaporate from the surface of pores and then either stick to other surfaces or move along the pore surface. Both processes help the ceramic become denser (Askeland and Wright, 2016).

Modern sintering methods include careful control of the furnace atmosphere. This control has several purposes: to protect materials from oxidation, create a reducing atmosphere, add carbon to the material (carburizing) and help remove pressing additives. Common gases used for these atmospheres include inert gases, nitrogen-based gases, dissociated ammonia, hydrogen, natural gas and sometimes vacuum environments (Groover, 2010).

1.2.7.1. Stages of sintering

The sintering process proceeds in distinct stages characterized by physical changes in the material, such as particle bonding and pore elimination. This process is usually

described in three stages. In the initial stage, particles begin to form bonds with one another. In the intermediate stage, most of the densification takes place. In the final stage, porosity is reduced to a minimum and the material gains full strength.

During the initial stage of sintering, the contact areas between particles grow and necks form at these contact points, as illustrated in fig. 1.9. As a result, the relative density increases to about 60–65% (Barsoum, 2020). Different mechanisms, such as plastic and viscous flow, vapor transport and diffusion, help the necks grow faster during sintering. These processes lead to shrinkage and densification of the material as the necks develop.

The initial stage continues until the neck radius reaches about 0.4 to 0.5 times the radius of the particles (Rahaman, 2003). At this point, densification mechanisms become more noticeable. The material shrinks by about 3% to 5%. As a result, the density increases to around 65% of the theoretical maximum.

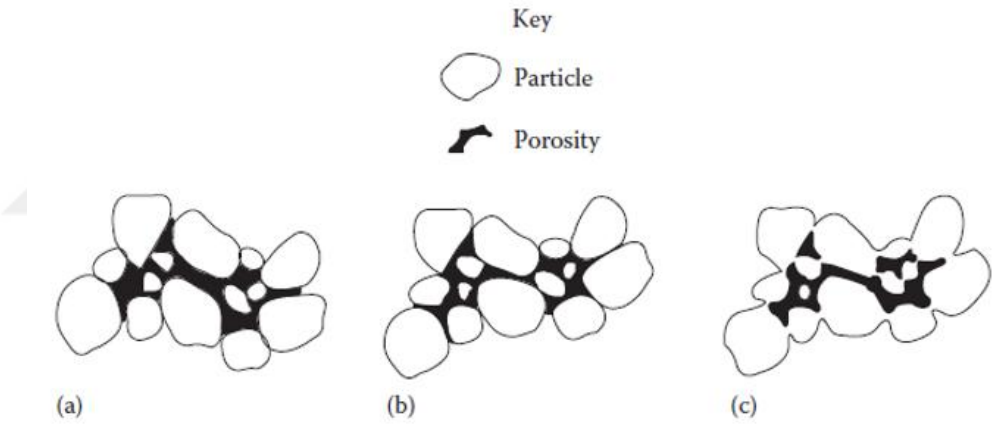

Figure 1.9. *Changes occur during the initial stage of sintering. (a) Starting particles, (b) rearrangement and (c) neck formation*

Continuous pore channels along the grain boundaries mark the intermediate stage of sintering. During this stage, the material's density increases from about 65% to 90% of its theoretical density (Rahaman, 2003). Material is transported toward the pores through diffusion, which eliminates vacancies. This process promotes neck growth between particles, reduces porosity and brings particle centers closer together (Richerson and Lee, 2018), as illustrated in fig. 1.10. The material shrinks in proportion to the decrease in porosity. Grain boundaries also migrate, allowing one grain to grow at the expense of its neighbor. This stage ends when the pores become isolated. Most of the

shrinkage occurs during this stage, which is critical for densification. As a result, the relative density of the material reaches around 90% of its theoretical value.

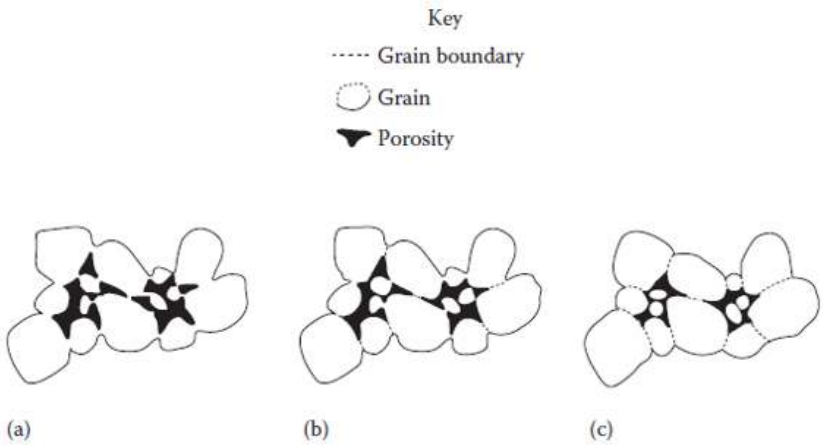

Figure 1.10. *(a) Neck growth and volume shrinkage, (b) lengthening of grain boundaries and (c) continued neck growth and grain boundary lengthening, volume shrinkage and grain growth.*

The final stage of sintering is initiated as the pores close and the pore channels disappear. At this point, vacancy diffusion along the grain boundaries helps eliminate remaining pores. Grain boundary movement and grain growth also support pore elimination and vacancy diffusion, as shown in fig. 1.10. However, if the grains grow too quickly, the boundaries advance more rapidly than the rate at which pores can be eliminated. As a result, some pores become trapped inside the grains and remain as isolated pores.

Isolated pores adopt different morphologies depending on their location. If they are at the grain boundaries, they become lenticular (lens-shaped). If trapped inside the grains, they become round (Barsoum, 2020). As the grains grow, these isolated pores are pushed away from the grain boundaries, making them harder to remove. For this reason, controlling grain growth is critical for complete pore elimination and achieving full densification of the material.

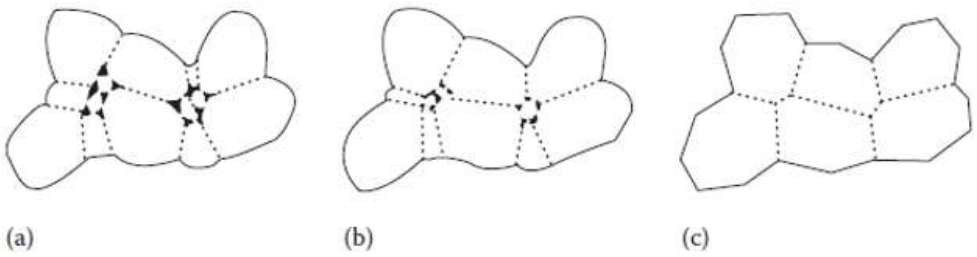

Figure 1.11. *(a) Grain growth with discontinuous pore phase, (b) grain growth with porosity reduction, (c) grain growth with porosity reduction and (c) grain growth with porosity elimination.*

1.3. Composite Materials

Composites are another main type of material, along with traditional metals, ceramics and polymers. They are usually defined as materials made by combining two or more different substances to create new properties that the individual materials cannot provide alone. The different parts of a composite must be chemically different and clearly separated by an interface (Chung, 2010).

The purposeful development of multiphase materials—such as fiberglass-reinforced polymer in the early 20th century—marked the beginning of composites as a separate class of materials (Callister Jr and Rethwisch, 2014). Composites are made of a strong reinforcement phase surrounded by a weaker matrix phase. When combined, these materials exhibit superior properties compared to their individual constituents. They can be harder, stronger, tougher, lighter, more resistant to heat and corrosion and may also exhibit enhanced conductivity. The primary objective is to integrate the desirable properties of each constituent into a superior overall material.

Throughout history, composite materials have been used in diverse applications. In ancient times, people used wood and mud to build structures or improve weapons. Today, composites are critical in fields such as the aerospace and sports equipment because they can be engineered with tailored properties for specific applications.

Although composites have many advantages, they also have some disadvantages. Many composites are anisotropic, which means their properties change depending on the direction of the force. Additionally, most polymer-based composites exhibit high chemical sensitivity. In addition, they are often expensive to produce and shape because the manufacturing processes are slow and costly (Groover, 2010).

Composites integrate the most desirable properties of different materials. An optimized set of properties can be achieved by carefully selecting and combining these materials. This makes composites useful in today's engineering and manufacturing fields (Shackelford, 2023).

1.3.1. Classification of composites

Composites can be grouped based on the type of matrix material. These groups include metal matrix composites, polymer matrix composites and ceramic matrix composites. They can also be classified by the type of reinforcement they contain, such as particle-reinforced composites, fiber-reinforced composites and structural composites.

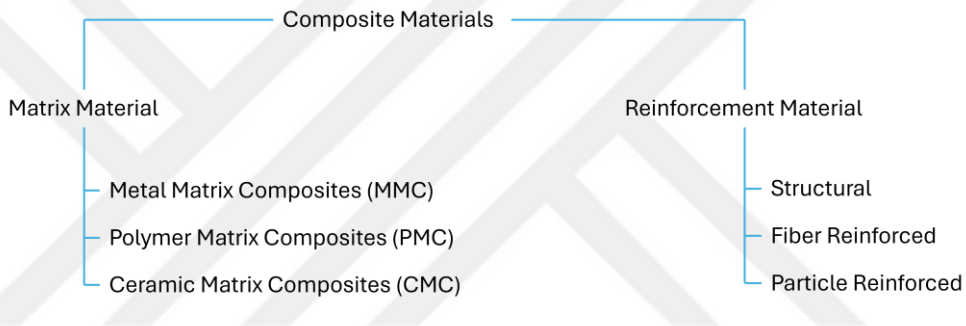

Figure 1.12. *Classification of composite materials*

Metal matrix composites (MMCs) consist of a ductile metal or alloy matrix reinforced with ceramic particles, continuous or short fibers, or whiskers derived from various materials. MMCs offer several advantages over polymer matrix composites (PMCs). They do not break down in contact with organic liquids, are not flammable, and can operate at elevated temperatures. However, MMCs are more expensive than PMCs because they require high temperatures during machining. For this reason, their use is limited to specific areas.

Polymer matrix composites (PMCs) can be grouped based on the type of polymer they use—either thermoset or thermoplastic. In general, thermoset matrix composites are more common. However, thermoplastic matrix composites are becoming more popular because they cost less, can be reused and have other advantages. Nevertheless, they present limitations, such as requiring higher machining temperatures and offering fewer suitable processing methods.

Ceramic matrix composites (CMCs) were developed to address the limitations of other composites while retaining their advantageous properties. CMCs are made of a ceramic matrix and a reinforcement phase, which usually includes fibers. However, they still face certain challenges, including ensuring thermal and chemical compatibility of components and limitations in manufacturable geometries.

1.4. Manufacturing and Machining

The word 'manufacturing' comes from 'manufacture,' which originally meant 'to make by hand.' In the past, this referred to making products using only hand tools. However, as technology developed and hand tools became limited, manufacturing became an industrial process. Today, it mainly uses machines to turn raw materials into finished products. Modern manufacturing includes many methods, such as forming, casting, welding and machining, as shown in fig. 1.13. These methods help shape materials efficiently and accurately.

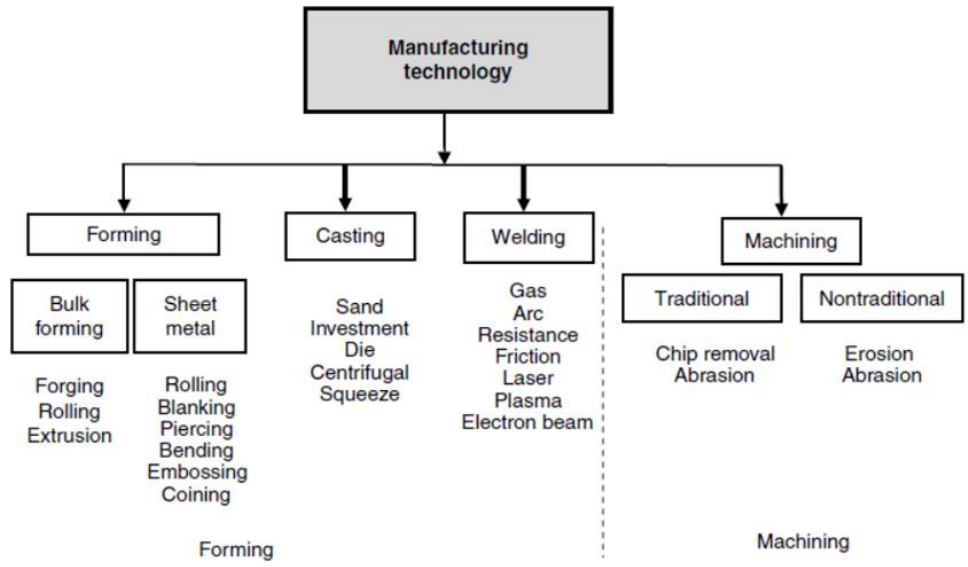

Figure 1.13. *Classification of manufacturing technologies (Youssef, 2016)*

Machining technology is divided into two main groups: traditional and non-traditional. Traditional machining can also be divided into chip removal and abrasion. Turning, milling and drilling are part of the chip removal subgroup and are the main machining methods used in industry (Youssef, 2016).

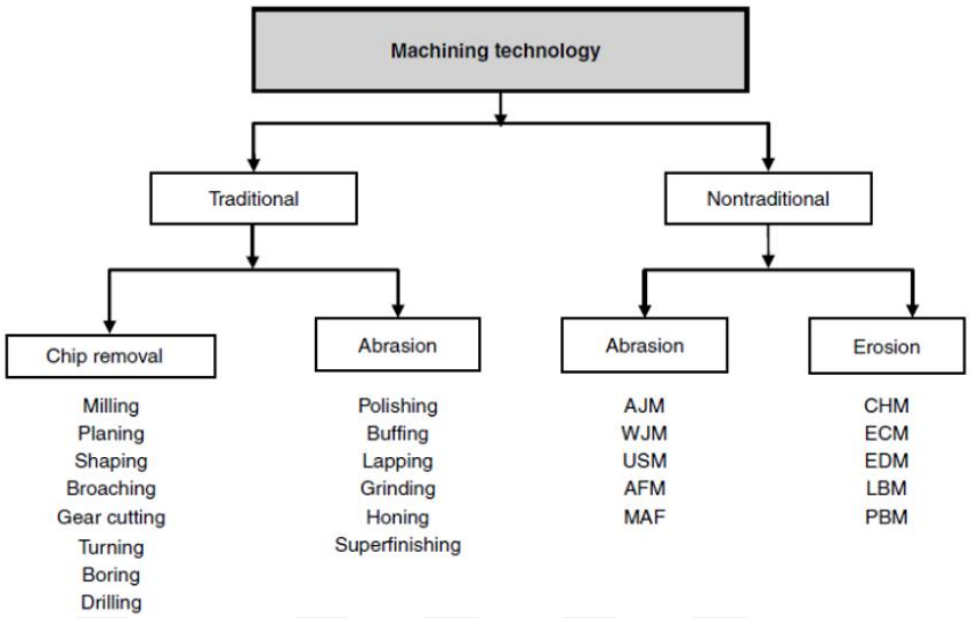

Figure 1.14. *Classification of machining technologies (Youssef, 2016)*

Turning is a machining process in which material is removed from a rotating workpiece using a single point cutting tool to produce a cylindrical shape. In milling, material is removed from a stationary workpiece using a rotating cylindrical tool with multiple cutting edges. Drilling is another machining process that uses a cylindrical tool, called a drill or drill bit, to create a circular hole in the workpiece. These machining methods are shown in fig. 1.15. They are commonly used in the processing of steel and iron in industry.

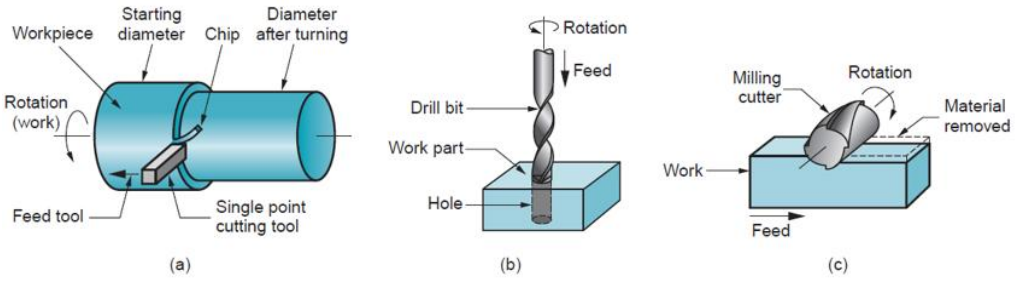

Figure 1.15. *Common machining operations: (a) turning operation, (b) drilling operation, (c) milling operation (Groover, 2010)*

1.4.1. Metals

Metals, ceramics and polymers are the three main groups of engineering materials. Metals are made of one or more metallic elements such as iron, aluminum, copper, or

titanium. They frequently contain small quantities of nonmetallic elements such as carbon, nitrogen, or oxygen. Metals are usually denser than ceramics and polymers. They are stiff, strong, ductile and fracture resistant (Callister Jr and Rethwisch, 2014). Alloys, which are made of two or more elements (with at least one being a metal), are commonly used in manufacturing. Metals and alloys are generally divided into two categories: ferrous metals and nonferrous metals.

Ferrous metals are metals that are mainly made from iron. This group includes steel and cast iron. Commercially, they represent the most significant class of metals. On the other hand, nonferrous metals include metals and their alloys that do not contain iron, such as aluminum, copper, gold and magnesium.

Pure iron has no commercial use. Iron is the main element in all commercial ferrous metals and is combined with carbon and other alloying elements to achieve desired properties. The main difference between wrought iron, cast iron and steel is the amount of carbon they contain. The approximate carbon content limits for each are as follows (Karwa, 2006);

- Cast iron: $C > 2\%$
- Steel: $0.1 < C < 2\%$
- Wrought iron: $C < 0.1\%$

1.4.1.1. Steels

Steels are iron–carbon alloys that contain different amounts of carbon by weight. They may also include other alloying elements such as manganese, chromium and nickel. However, it is the carbon content that transforms iron into steel. Different sources define various types of steel, but steels are generally divided into two main groups: low-alloy steels and high-alloy steels. Low-alloy steels are further classified into low-carbon, medium-carbon and high-carbon steels.

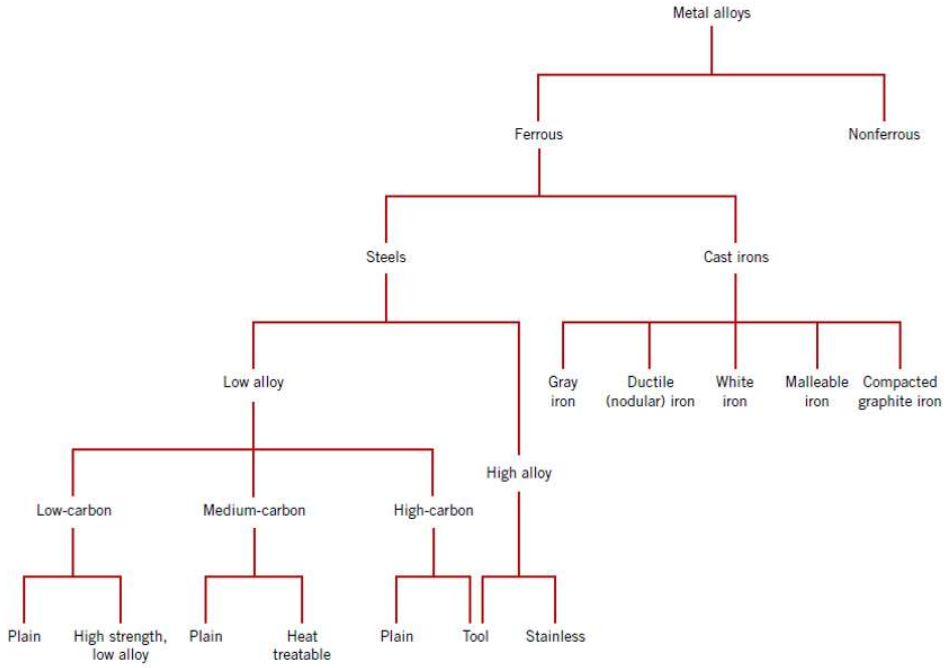

Figure 1.16. *Classification of ferrous metals (Callister Jr and Rethwisch, 2014)*

Low-carbon steel contains less than 0.20% carbon by weight and is the most used type of steel. They are used in automobile body parts, steel plates and railroad rails. Because they are easy to manufacture, low-carbon steels are suitable for applications where extremely high strength requirements are not critical.

Medium-carbon steels contain between 0.20% and 0.50% carbon by weight. They are used in applications that require more strength than low-carbon steels. Common uses include machine parts and engine components such as crankshafts and connecting rods.

High-carbon steels contain more than 0.50% carbon by weight. They are used in applications requiring high strength, stiffness and hardness. Examples include springs, cutting tools, blades and parts that must resist wear.

Plain carbon steels contain only small amounts of elements other than carbon, mostly as impurities. These include about 0.4% manganese and smaller amounts of silicon, phosphorus and sulfur. As the carbon content increases, the strength of plain carbon steel also increases.

Stainless steels are steel alloys that contain a high amount of chromium. They are known for their resistance to corrosion, high strength and flexibility. They are called "stainless" because, when exposed to oxygen, they form a thin, colorless, hard layer of chromium oxide that protects the surface and keeps it shiny. If the surface is scratched,

this protective film forms again. The steel must contain at least 10.5% chromium by weight for passivation.

Stainless steel is difficult to cut because of its low thermal conductivity, high thermal expansion, high ductility and high work hardening rate. Its low thermal conductivity raises the temperature of the cutting tool, which shortens the tool's life. The combination of high work hardening and low thermal conductivity affects chip formation, often resulting in segmented chips. In addition, the high thermal expansion of stainless steel makes it challenging to maintain precise machining tolerances. Its high ductility also causes built-up edge (BUE) on the cutting tool, which damages surface quality and increases vibration and chatter.

A critical factor in achieving optimal machining performance for stainless steel is selecting the appropriate cutting speed and tool. Effective implementation requires a comprehensive understanding of how cutting speed influences the material's mechanical and thermal properties.

1.4.2. Cutting tools

Cutting tools are used to carry out machining operations. During these processes, the tool is exposed to elevated stress and temperature. If the cutting force exceeds critical limits, the tool may fracture. The tool material can soften and fail if the temperature gets too high. Even if these failures do not occur, the cutting edge will inevitably experience wear over time. Two key factors in cutting tool technology are the tool material and the tool shape. The first focuses on developing materials that can handle the forces, heat and wear during machining. The second involves designing the tool's shape to match the material and the specific operation (Groover, 2010).

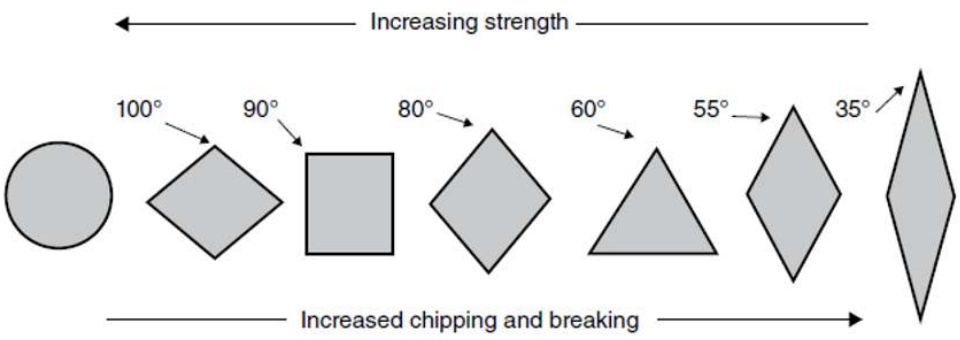

Figure 1.17. *The geometries of cutting tools (Youssef, 2016)*

Toughness, hot hardness and wear resistance are three important properties of a cutting tool material. The material must be tough enough to prevent breaking during cutting. Toughness is a combination of strength and ductility in the tool material. Hot hardness is the ability of a material to maintain its hardness at elevated temperatures. Since cutting tools work in hot environments, this property is considered critical. The material must also resist wear. To prevent abrasive wear, the tool must be hard. Hardness is one of the most important requirements for all cutting tool materials (Youssef, 2016).

At the beginning of the 20th century, Taylor replaced carbon steel tools with high-speed steel, which tripled cutting speeds. In 1926, Krupp developed a very hard sintered carbide material called Widia, allowing cutting and forming speeds 3 to 6 times faster than high-speed steel. By 1950, ceramic tools were introduced, reaching speeds 6 to 8 times higher than high-speed steels. Recently, tool materials like coated carbides and cubic boron nitride (CBN) have been developed. Today, polycrystalline diamond tools are mainly used for finishing with cutting speeds over 2 kilometers per minute (Youssef and El-Hofy, 2008). Although traditionally high speed steels (HSS) and hard metal (carbide) tools have been widely used, ceramic-based tools have been developed for higher cutting speed and machining difficult materials.

1.4.2.1. Ceramic cutting tools

Ceramics are made by combining metallic and nonmetallic materials, with oxides, nitrides and carbides being the most common types. Ceramic materials are generally characterized by high stiffness and strength. They also exhibit exceptional hardness. However, ceramics have long been known for being brittle and easy to crack due to their lack of ductility. Today, newer ceramics are being developed to enhance fracture resistance. Because of these properties, ceramics are suitable for machining metals at high cutting speeds and without cutting fluids. The most common ceramic materials used in cutting tools are alumina (Al_2O_3), silicon nitride (Si_3N_4) and SiAlON (a mix of silicon, aluminum, oxygen and nitrogen).

Image 1.1. *Ceramic cutting tools*

Aluminum oxide is wear-resistant but brittle and it is mostly used for machining hardened steel. Another type is silicon nitride, which is used for machining cast iron and offers lower hardness but greater toughness. Between these two materials is a group of ceramics called SiAlONs, which combine their properties. A higher amount of aluminum oxide makes the material harder, while a higher amount of silicon nitride makes it tougher (Yin Z. et al., 2015).

1.4.2.2. Alumina based (Al_2O_3 -) cutting tools

The main aluminum source is bauxite, mostly hydrated aluminum oxide ($Al_2O_3 \cdot H_2O$) and other oxides. The extraction of aluminum from bauxite can be summarized in three main steps:

- Washing and crushing the ore into fine powder.
- The Bayer process, in which the bauxite is converted to pure alumina (Al_2O_3)
- Electrolysis, in which the alumina is separated into aluminum and oxygen gas (O_2)

The Bayer process, named after the German chemist who developed it, involves dissolving bauxite powder in a solution of caustic soda (NaOH) under pressure. Then, pure aluminum oxide (Al_2O_3) is separated from the solution by precipitation.

Aluminum oxide cutting tools perform well when turning cast iron and steel at high speeds. They are mostly used for finishing turning of hardened steels, with high cutting speeds, low feed rates and shallow cutting depths. Although alumina is inexpensive and widely available, the processing cost is high; therefore, ceramic tools are less economical

than carbide tools. They are highly resistant to crater wear and usually do not require a coolant. Their tool life is like carbide tools when used at double the cutting speed.

To maximize the advantages of ceramic tools, rigid tool holders and machine tools are required. Ceramics remain chemically stable (inert) up to very high temperatures, making them suitable for machining steels, semi-hard steels and cast iron at cutting speeds up to 600 m/min and feed rates up to 0.25 mm/rev. They maintain their cutting performance at temperatures up to 1200°C. Even higher speeds and feeds are possible when machining nonferrous metals.

However, due to their low toughness, ceramics are not recommended for heavy interrupted cutting operations. Oxides such as titanium, magnesium, chromium, or zirconium can be evenly distributed within the alumina matrix to improve their toughness. In conventional machining, ceramic tools are usually used as inserts. Materials like aluminum and titanium react chemically with alumina and are unsuitable for ceramic machining. Among ceramic types, alumina-based ceramics are more suitable for machining stainless steel than silicon nitride ceramics (Cutler and Hurford, 1988).

Al_2O_3-TiC (alumina-titanium carbide) based composite cutting tools have an important role in today's production thanks to their superior heat and wear resistance. Al_2O_3-TiC cutting tools are composite ceramics containing 30-40% titanium carbide (TiC) particles in an alumina matrix.

Al_2O_3-TiC ceramic cutting tools belong to mixed oxide and carbide-based materials. This composite has a higher hardness than pure alumina. (Grigoriev et al., 2019) This high hardness can be maintained at temperatures up to 800 °C. Ensuring that the cutting edge is resistant to deformation even at high temperatures.

The brittleness of ceramics is a factor that limits their use. Al_2O_3-TiC composite has higher fracture toughness than pure alumina (approximately 5.4 MPa $m^{1/2}$, pure alumina ~4.5 MPa $m^{1/2}$). TiC particles have a deflection effect, making crack propagation more difficult and increasing toughness to some extent. However, toughness is still low compared to metal-based materials, meaning there is a fracture risk in interrupted cutting or vibrating conditions. (Zmak et al., 2025)

Al_2O_3-TiC cutting tools offer significant advantages, particularly in machining steel materials. These advantages came from the material's superior performance against the high temperature, hardness and wear conditions encountered during steel machining. Carbide, which makes up more than ~80% tool inserts used today, is used in many ways

because of its balance of toughness and wear resistance. However, carbide inserts typically have a hardness of ~16-18 GPa and their performance degrades at high temperatures (above 700-800 °C) due to softening of the bond material (Zmak et al., 2025). Al_2O_3-TiC ceramics do not contain metal binders such as cobalt. Therefore, they retain their hardness at higher temperatures and resist thermal softening.

Additionally, ceramics are more chemically inert and less likely to react with steel. However, carbides are superior to ceramics in terms of toughness. They do not break under sudden impact and are more durable than ceramics in interrupted cutting.

On the other hand, silicon nitride (Si_3N_4) based ceramics are tougher and more resistant to thermal shock than alumina ceramics. Therefore, they are advantageous in interrupted cutting, especially in cast-iron machining. However, the chemical stability of Si_3N_4 ceramics is not as good as alumina. They can react with steel and wear rapidly. They interact chemically with the workpiece and result in the formation of an interlayer phase.

Al_2O_3-TiC based cutting tool composites have long been preferred because TiC has low friction coefficients and can suppress abnormal grain growth during sintering (Yin Z. et al., 2015). The addition of 3-4 wt.% TiH_2 in the Al_2O_3-30 wt.% TiC system by pressureless sintering provided >99% relative density, >22 GPa hardness and >600 MPa flexural strength (Cuttler, Hurford and Virkar, 1988). Chae and Kim (1993) investigated the effect of Y_2O_3 addition on the densification behavior of the Al_2O_3-30 wt.% TiC composite. Because achieving full density at high temperatures is difficult due to gas-forming reactions between Al_2O_3 and TiC, the sinter + HIP method was used in the study. Optimum results were achieved with 0.35 wt.% Y_2O_3 addition, achieving a relative density of 97% after sintering at 1700 °C and the open pores were closed. (Cai et al., 2002) investigated the preparation, microstructure and properties of Al_2O_3-TiC composites. Samples produced using powder metallurgy were evaluated under different sintering conditions and it was observed that the density and mechanical properties of the composites changed with increasing TiC content. The results indicated that 30 wt.% TiC content optimized the density and mechanical properties of the composites with hardness values reaching approximately 20 GPa and fracture toughness reaching 5 MPa $m^{1/2}$. Densification became more difficult and porosity increased at higher TiC content. (Kasuriya and Atong, 2006) studied Al_2O_3-30 wt.% TiC composites and investigated the effects of MgO (0.5 wt.%) and Y_2O_3 (0.3-1 wt.%) additives on material properties under

pressureless sintering conditions at different temperatures. The results showed that the sample sintered at 1800 °C containing 0.5 wt.% MgO-0.3 wt.% Y_2O_3 reached 97% relative density. In the study of (Yang and Roberts, 2005), Al_2O_3-TiCN composites obtained by gas pressure sintering exhibited a density over 99%, reached a hardness of 19.2 GPa and a fracture toughness of 5.1 MPa $m^{1/2}$.

The objectives of this thesis are to systematically reveal the sinterability of Al_2O_3-TiC composites by Gas Pressure Sintering (GPS) method and to quantitatively determine the effects of rare earth oxide (REO) additions (Er_2O_3, Yb_2O_3, Y_2O_3, Sm_2O_3, CeO_2) on densification, microstructure and mechanical performance. In this context, the relationship between sintering parameters, microstructure and properties in Al_2O_3-TiC composition with varying TiC and ZrO_2 content processed by GPS in a 5 bar Ar atmosphere at 1875-1900 °C for 30-90 min is to be observed. The aim is to determine the microstructures corresponding to hardness and fracture toughness and to compare them with commercial products. The goal is to propose a validated process recipe for Al_2O_3-TiC-based inserts that offer high relative density, increased hardness and improved fracture toughness by optimizing GPS parameters and REO additives.

2. MATERIALS AND METHODS

In this study, different compositions were prepared using various weight percentages of TiC (20, 30, 40 and 55), as suggested in the literature, to determine the optimal TiC content in the Al_2O_3-TiC composite. The optimal TiC ratio was identified. After that, ZrO_2 was incorporated at two different weight percentages (3.5 and 5) to enhance the toughness of the composite and the optimal ZrO_2 ratio was also determined.

To further improve the mechanical properties of the Al_2O_3-TiC-ZrO_2 composite (referred to as ATZ), rare earth oxides (REOs) such as Er_2O_3, Y_2O_3, Yb_2O_3, CeO_2 and Sm_2O_3 were added in 3.5% and 5% by weight. The effects of these additions were also investigated. The specifications of the powders used in sample preparation at the laboratory scale were listed in Table 2.1.

Table 2.1. *The powders used for the study, the supplier company of these powders and their purity*

Powders	Supplier/Country	Purity
Al_2O_3	Alteo, France	>99.8%
TiC	Zhuzhou, China	>99%
ZrO_2	Inframat, USA	>99,9+%
Er_2O_3	Treibacher, Austria	>99.9+%
Y_2O_3	REEtec, Norway	>99.89%
Yb_2O_3	Treibacher, Austria	>99.9%
CeO_2	Treibacher, Austria	>99.9+%
Sm_2O_3	Treibacher, Austria	>99.9+%

2.1. Powder Preparation

The starting powders, totaling 60 grams, were milled and mixed in a planetary ball mill using 125 ml of 99.8% pure isopropanol and 75 grams of ZrO_2 balls at 300 rpm for 2 hours. After mixing, the slurry was dried using an evaporator at 50°C with a rotation speed of 45 rpm. The dried powder was then kept in an oven overnight at 90°C. Finally, the powders were sieved using a 250 μm sieve.

The starting powders were prepared for granule production by mixing 60% solid by weight with pure water. ZrO_2 balls, equal to twice the total weight of the mixture, were added. A dispersant was also included at 4% by weight. The mixture was stirred in an attrition mill at 1000 rpm for 2 hours. After milling, the slurry was transferred to a propeller mixer using a peristaltic pump and passed through a 32 μm sieve. Appropriate amounts of binder, lubricant and plasticizer were incorporated in the propeller mixer.

The prepared ceramic slurry was dried using a Nubilosa LTC-2 model spray dryer. The slurry was pumped into the dryer at a speed of 30 rpm using a peristaltic pump and sprayed with air pressure set at 1.1 bar. To avoid burning the organic components in the slurry, the dryer's outlet temperature was set to 110°C and the inlet temperature to 240°C.

The weight percentage of all the compositions prepared through the study is provided in Table 2.2.

Table 2.2. *Weight percentage of all the compositions*

Composition Name	Al_2O_3	TiC	ZrO_2	Er_2O_3	Y_2O_3	Yb_2O_3	Ce_2O_3	Sm_2O_3
T20	80	20	0	0	0	0	0	0
T25	75	25	0	0	0	0	0	0
T30	70	30	0	0	0	0	0	0
T40	60	40	0	0	0	0	0	0
T55	45	55	0	0	0	0	0	0
AT-0ZrO_2	70	30	0	0	0	0	0	0
AT-3.5ZrO_2	66.5	30	3.5	0	0	0	0	0
AT-5ZrO_2	65	30	5	0	0	0	0	0
ATZ-3.5Er	63	30	3.5	3.5	0	0	0	0
ATZ-5Er	61.5	30	3.5	5	0	0	0	0
ATZ-3.5Y	63	30	3.5	0	3.5	0	0	0
ATZ-5Y	61.5	30	3.5	0	5	0	0	0
ATZ-3.5Yb	63	30	3.5	0	0	3.5	0	0
ATZ-5Yb	61.5	30	3.5	0	0	5	0	0
ATZ-3.5Ce	63	30	3.5	0	0	0	3.5	0
ATZ-5Ce	61.5	30	3.5	0	0	0	5	0
ATZ-3.5Sm	63	30	3.5	0	0	0	0	3.5
ATZ-5Sm	61.5	30	3.5	0	0	0	0	5

2.2. Shape Forming Process

The powders were pressed using a hand press and a 12 mm die at different pressures to study the effect of pressure on the composite. Afterwards, they were cold isostatically pressed at 300 MPa to increase green density and form pellets. All powder mixtures followed the same processing steps, except for the granules. The granules

produced by the spray dryer were shaped using a fully automatic press (Komage S-20XT, Germany) under different pressures to examine how pressure affects the composite.

2.3. Binder Removal

The organic binders incorporated during granule preparation must be eliminated before sintering. An atmosphere-controlled thermal debinding method was employed to achieve this. If this process is done in an oxygen atmosphere, there is a risk that TiC in the mixture could oxidize and turn into TiO_2. To prevent this, the thermal debinding was carried out in an argon (Ar) atmosphere, holding the temperature at 550 °C for 1 hour. A Protherm PLF 110/45 model furnace was used for the process.

2.4. Sintering

This study used two different sintering methods: Spark Plasma Sintering (SPS) and Gas Pressure Sintering (GPS). First, the sintering behavior of the composites was examined in SPS experiments with holding times of 5, 10 and 15 minutes at temperatures between 1500–1800 °C. The results from the SPS tests were then used to define the sintering conditions for the GPS process.

GPS experiments were carried out at higher temperatures, ranging from 1800–1950 °C, with 30, 60 and 90 minutes holding times. A two-step sintering method was applied in the GPS process to improve densification. In the first step, sintering was done under 5 bar of argon gas and under 90 bar of argon gas in the second step,.

2.5. Characterization of Compositions

2.5.1. Density

The Archimedes method was used to measure the density of the produced samples. This method is based on the principle that the difference between a material's dry weight and its weight in liquid equals the buoyant force acting on it (ASTM-311).

The samples were boiled in pure water for 3 hours to remove air from the pores. Then, the suspended weight (W1) and wet weight (W2) were measured at room temperature. After that, the samples were placed in an oven preheated to 80 °C for 1 hour to remove the water inside the pores. Finally, the dry weight (W3) was recorded. Bulk density (B.D.) and open porosity (O.P.) were calculated using the equations given below.

$$Bulk\ Density\ \left(\frac{g}{cm^3}\right) = \frac{W_3}{W_2 - W_1} \times \rho_{water} \quad (2.1)$$

$$Open\ Porosity\ (\%) = \frac{W_2 - W_3}{W_2 - W_1} \times 100 \quad (2.2)$$

The theoretical densities of compositions were calculated using the rule of mixtures method to enable comparison. The formula is provided below.

$$\rho_c = \rho_1 v_1 + \rho_2 v_2 \quad (2.3)$$

where, ρ_c is the density of composite, ρ_1 is the density of "substance1", v_1 is the volume fraction of "substance1", ρ_2 is the density of "substance2", v_2 is the volume fraction of "substance2".

2.5.2. Phase analysis

Phase analysis of the samples was performed using an X-Ray Diffraction (XRD) device (Rigaku-Rint 2000, Japan) with copper as the target metal (λCuKα = 1.54 nm). After sintering, the samples were ground into powder using a ring mill. XRD analysis was then carried out on these powders.

2.5.3. Microstructure and chemical analysis

The sintered samples were cut using a precision cutting machine (Struers-Secotom 1, Denmark). After cutting, they were mounted in Bakelite molds with their cross-sections facing upward. This was done using a hot mounting device (Struers-LaboPress 3, Denmark) at 180 °C for 4 minutes under a 10 kN load. The mounted samples were then polished using an automatic polishing machine (Struers-TegraPol 25, Denmark).

The polishing process consisted of two stages: coarse polishing and fine polishing. Appropriate polishing disks and diamond particle solutions of 9, 6, 3 and 1 μm were used during fine polishing. After polishing, the sample surfaces were coated with a thin layer of gold-palladium alloy in a vacuum for 7 seconds. This coating improved conductivity and prevented surface charging before microstructure analysis.

Microstructure and fracture surface analyses were performed using a scanning electron microscope (Zeiss-Supra 50 VP, Germany). Chemical analysis of the samples was carried out using an energy-dispersive X-ray (EDS) detector (Oxford Instruments, UK) attached to the microscope.

2.5.4. Hardness and fracture toughness

Hardness measurements of the polished cross-sections were performed using the Vickers microhardness method (Emcotest-M1C 010, Austria). A square pyramid-shaped diamond tip with a top angle of 136° was used for indentation. The tests were carried out under a 49 N load for 6 seconds. The results were calculated using the equations below (Charles and Evans, 1976). Measurements were taken at five different points on each sample to ensure accuracy and the average values were then calculated.

$$HV_5 = 0.47\frac{P}{a^2} \tag{2.4}$$

Where HV_5 is Vickers hardness, P is the applied load and a is the half of the diagonal length of the mark made by the diamond tip.

Fracture toughness was calculated by measuring the crack lengths resulting from Vickers indentation under an optical microscope and using the formula suggested by Charles and Evans (Charles and Evans, 1976).

$$K_{1c} = 0.15\ x\ \left(H\sqrt{a}\right)\ x\ \left(\frac{c}{a}\right)^{-1.5} \tag{2.5}$$

Where, K_{1c} is the fracture toughness ($MPa \cdot m^{0.5}$), H is the Vickers hardness (GPa), a is the half of the diagonal length made by the diamond tip (μm) and c is the crack length (μm).

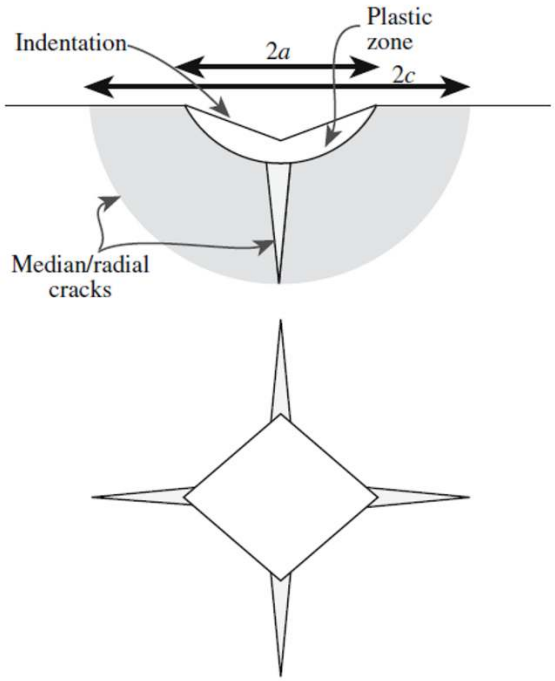

Figure 2.1. *Cracks at an indent allow determination of K_{Ic}. (Carter and Norton, 2007)*

3. RESULTS AND DISCUSSIONS

3.1. Characterisation of Commercial Products

Al_2O_3-TiC ceramic cutting tools from three different commercial companies were characterized. The densities of the products were measured using the Archimedes method and were presented in Table 3.1.

Table 3.1. *Commercial products and their densities*

Product Name	Density (g/cm^3)
C1	4.2829
C2	4.6604
C3	4.2928

Considering the density results, it is possible to say that C1 and C3 were products with similar compositions. The density of the C2 product differs from the others due to the TiN coating on its surface.

Backscattered SEM images of three different commercial Al_2O_3-TiC composite products were shown in fig. 3.1. The C1 sample (fig. 3.1.a) has a coarser and more heterogeneous structure than the others. Clear boundaries between dark and light gray areas and the TiC particles appear more unevenly and coarsely distributed. The C2 sample (fig. 3.1.b) shows a homogeneous, fine-grained structure. TiC particles were smaller and more evenly spread within the Al_2O_3 matrix. The C3 sample (fig. 3.1.c) displays a microstructure where the TiC phase is dense and separated from the Al_2O_3 matrix. The amount of TiC appears to be higher than in the other samples. The sharp phase boundaries suggest that this sample may have high hardness, but possibly lower fracture toughness.

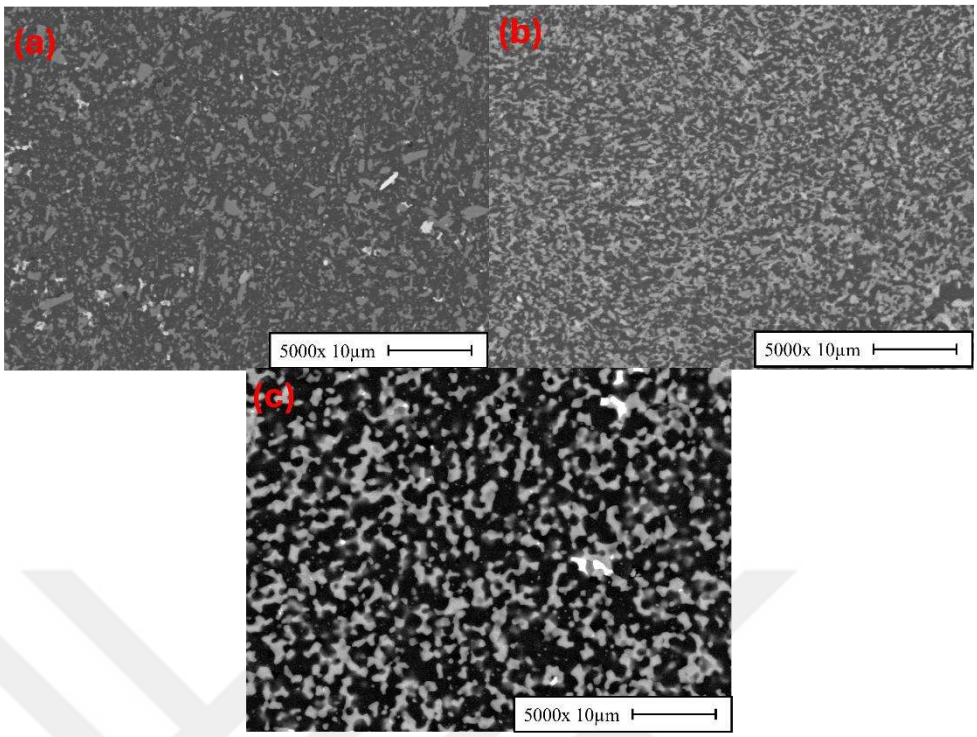

Figure 3.1. *Representative backscattered SEM images taken from polished surface of commercial products. C1 (a), C2 (b) and C3 (c)*

The EDS analysis result of the C1 sample is shown in fig. 3.2. The analysis confirms that aluminum (30.82 wt.%) and titanium (19.71 wt.%) were the main elements in the composite. These values indicate that the TiC phase is added to the Al_2O_3 matrix in the C1 sample. The oxygen content (42.76 wt.%) supports the presence of a high amount of Al_2O_3. The carbon content is measured at 4.42 wt.%. Small amounts of cobalt (0.49 wt.%) and ytterbium (1.79 wt.%) were also detected. These elements may have been used as binders, additives in the production process, or special components added by the manufacturer to improve the material's properties.

Element	Weight%	Atomic%
C	4.42	7.98
O	42.76	57.93
Al	30.82	24.76
Ti	19.71	8.92
Co	0.49	0.18
Yb	1.79	0.22

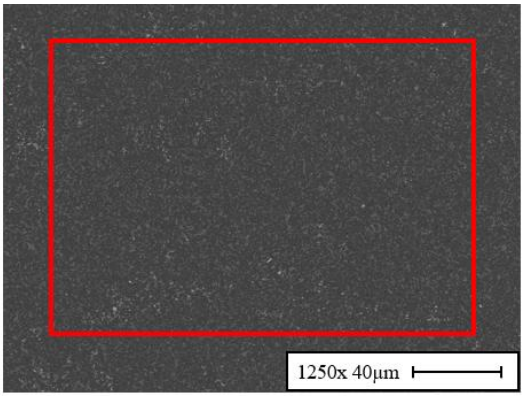

Figure 3.2. *Representative backscattered SEM image and EDS analysis taken from the polished surface of C1*

The EDS analysis result of the C2 sample is shown in fig. 3.3. The analysis confirms that aluminum (23.17 wt.%) and titanium (18.07 wt.%) were the main elements in the composite. The oxygen content (37.25 wt.%) indicates a high amount of Al_2O_3. Other noteworthy elements were molybdenum (Mo, 8.40 wt.%) and zirconium (Zr, 2.78 wt.%). These elements may have been intentionally added to stabilize the microstructure, control grain growth and improve mechanical properties. A small amount of magnesium (0.12 wt.%) was also detected, possibly in the form of MgO, which may have been used as a sintering aid.

Element	Weight%	Atomic%
C	10.23	18.77
O	37.25	51.30
Mg	0.12	0.11
Al	23.17	18.92
Ti	18.07	8.31
Zr	2.78	0.67
Mo	8.40	1.93

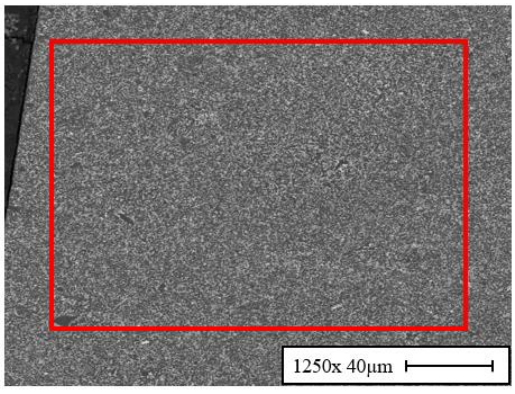

Figure 3.3. *Representative backscattered SEM image and EDS analysis taken from the polished surface of C2*

The EDS analysis result of the C3 sample is shown in fig. 3.4. The analysis confirms that aluminum (30.55 wt.%) and titanium (20.36 wt.%) were the main elements in the composite. The oxygen content (42.59 wt.%) supports the presence of a high amount of Al_2O_3. Small amounts of zirconium (1.87 wt.%) and magnesium (0.24 wt.%) were also

detected. These elements may have been added to improve the material's mechanical properties and support the sintering process.

Element	Weight%	Atomic%
C	4.39	7.92
O	42.59	57.68
Mg	0.24	0.22
Al	30.55	24.53
Ti	20.36	9.21
Zr	1.87	0.44

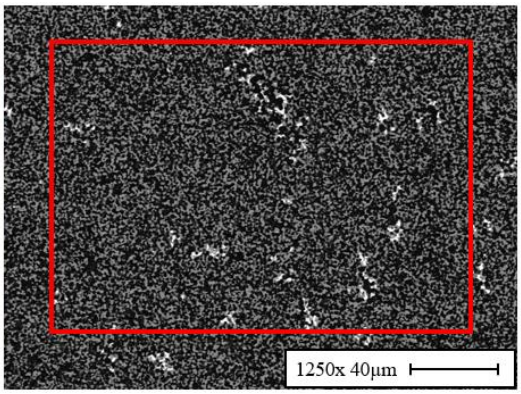

Figure 3.4. *Representative backscattered SEM image and EDS analysis taken from the polished surface of C3*

The C3 is an advanced composite that largely follows the Al_2O_3-TiC system in its chemical composition, but it is modified with small amounts of Zr and Mg. When the SEM image and EDS data were evaluated together, it can be said that this product is a ceramic material with high sintering quality, strong structural integrity and suitable properties for engineering applications.

A comparison of the hardness and fracture toughness of the C1, C2 and C3 samples is shown in fig. 3.5. The highest hardness value belongs to the C2 sample (~20.5 GPa). C3 ranks second with a hardness of about 20 GPa. The C1 sample has the lowest hardness, around 18 GPa. This lower value may be due to the more noticeable and irregular TiC clusters in its SEM image.

The order is reversed when it comes to fracture toughness. The C1 sample has the highest fracture toughness at approximately 6.0 $MPa \cdot m^{1/2}$. CW2015 has the lowest value, around 4.5 $MPa \cdot m^{1/2}$, while C3 is in the middle with about 5.2 $MPa \cdot m^{1/2}$. Despite its high hardness, C2 shows low toughness, which suggests that its structure is more brittle.

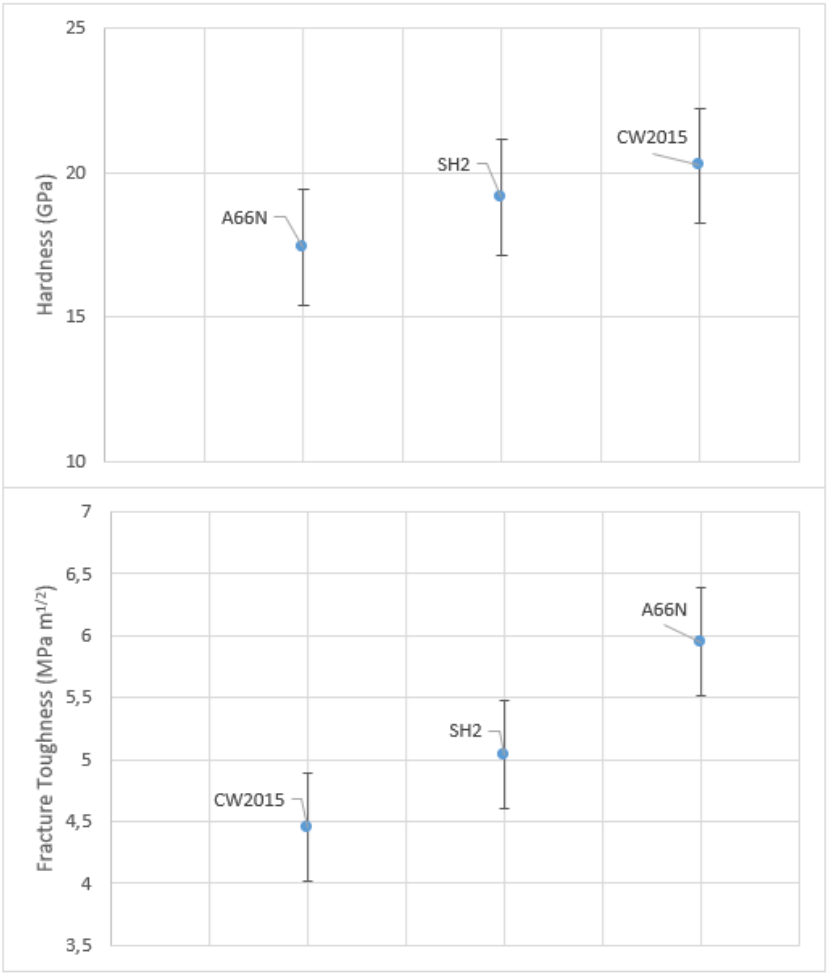

Figure 3.5. *Representative hardness and fracture toughness of C1, C2 and C3 samples*

When a general evaluation is made, the C2 sample stands out regarding hardness, while the C1 sample shows the highest fracture toughness. The C3 sample balances between these two mechanical properties, with medium-high hardness and moderate fracture toughness.

Depending on the application area, C2 can be preferred in environments where high wear resistance is needed, C1 is suitable where impact resistance is important and C3 is a good option for systems that require a balance between hardness and toughness.

3.2. Determination of Al_2O_3 and TiC Content in Composition

In this study, the mechanical properties, microstructural behavior and sintering process of Al_2O_3-TiC composites were investigated and compared with findings from the literature. Four different compositions (T20, T30, T40 and T55) were prepared, containing between 20% and 55% TiC by weight. The hardness, fracture toughness and

relative density results were analyzed and similarities and differences with previous studies were discussed.

The particle size of the starting powders (1.2 μm for Al_2O_3 and 2.3 μm for TiC) played an important role in achieving a homogeneous microstructure. Compared with literature, the Spark Plasma Sintering (SPS) method used in this study showed advantages over the commonly used Hot Pressing (HP) method. Table 3.2 presents the Al_2O_3-TiC compositions, relative densities, hardness values and fracture toughness results from selected studies.

Table 3.2. *Properties of Al_2O_3-TiC compositions in the relevant literature*

Compositions	Relative Density (%)	Hardness (GPa)	Fracture Toughness (MPa $m^{1/2}$)
Al_2O_3-30wt.%TiC (Cutler and Hurford, 1988)	4.26	19.9 ± 0.7	4.01 ± 0.46
Al_2O_3-30vol.% TiC (Ezugwu and Tang, 1995)	4.29	22.3	4.5
Al_2O_3-30wt.%TiC (Mao, et al., 1997)	97.4	20.73	5.2
Al_2O_3-30wt.%TiC (Liu, et al., 2004)	Densified	21.11	5.14
Al_2O_3-TiC (1:1vol.%) (Deng, Can, and Sun, 2005)	-	20	5.2
$Al_2O_3$30wt.%TiCN (Yang and Roberts, 2005)	99.5	19.6	5.85
Al_2O_3-30wt.TiC (You, et al., 2005)	99.6	21.9	6.12
Al_2O_3-45wt.%TiC (Chen and Kny, 2000)	-	20	4.6
Al_2O_3-40wt.%TiC (Zhang, Ling, and Li, 2005)	99.3	20.5	4.87
Al_2O_3-30wt.%TiC (Goldstein and Singurindi, 2000)	98.2	20.10	4.38
Al_2O_3-20wt.%TiC (Meir, Kalabukhov and Hayun, 2014)	99.5	21	8.3
Al_2O_3-40vol.%TiC (Grigoriev, et al., 2018)	99	23.3	7.8
Al_2O_3-40vol.%TiC (Yin et al., 2013)	94	16.7	6
Al_2O_3-30vol.%TiC (Fei et al., 2014)	-	20.75	6.4
Al_2O_3-55wt.%TiC (Xing, et al., 2014)	-	23.5	5.04

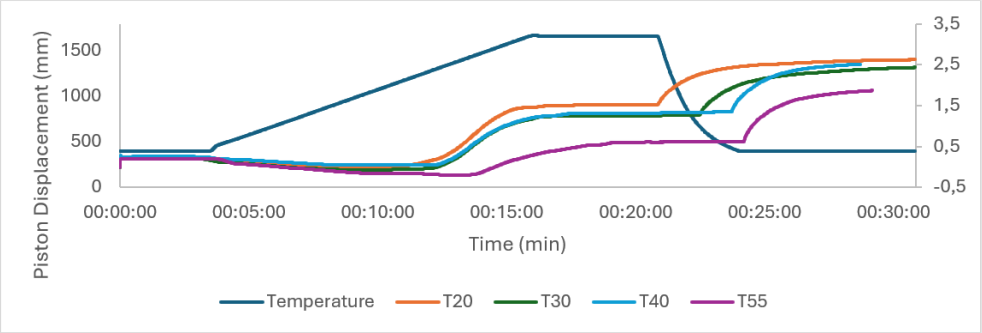

Figure 3.6. *Representative SPS sintering curves of prepared compositions.*

The SPS graph of the prepared compositions was shown in fig. 3.6. The specific sintering temperature for each composition was determined by analyzing the punch displacement curve as a function of temperature during sintering. The temperature at which the displacement curve began to rise was defined as the shrinkage start temperature. The point where the curve became stable was defined as the sintering temperature.

The sintering process was stopped when the piston reached the sintering temperature (T_{sin}), with a heating rate of 100 °C/min and under 16 MPa of uniaxial pressure, held for 5 minutes. Densification began at 1885 °C for T55, 1800 °C for T40, 1685 °C for T30 and 1665 °C for T20.

It was observed that decreasing the titanium carbide content led to a lower sintering temperature. The densities of the samples produced by Spark Plasma Sintering were measured using Archimedes' method. Hardness and fracture toughness were determined using the Vickers indentation method. The results were presented in Table 3.3.

Table 3.3. *Sintering temperatures and mechanical properties of the investigated compositions*

Composition	Sintering Temperature (°C)	Relative Density (%)	Hardness (GPa)	Fracture Toughness (MPa $m^{1/2}$)
T55	1885	98.98	20.85	5.11
T40	1800	98.94	20.23	4.43
T30	1685	99.34	19.05	4.66
T20	1665	99.42	18.77	3.94

The T20 composition showed the highest relative density, with a value of 99.42%. This suggests that the low TiC content helped reduce porosity during sintering, leading to higher density. A similar result was reported by Meir et al. (Meir, Kalabukhov and

Hayun, 2014) for an Al_2O_3-TiC composition containing 20 wt.% TiC, which had a relative density of 99.5%, hardness of 21 GPa and fracture toughness of 8.3 $MPa \cdot m^{1/2}$. In this study, the T20 composition showed a hardness of 18.77 GPa and fracture toughness of 3.94 $MPa \cdot m^{1/2}$.

The T30 composition performed similarly to T20 in terms of density, with a relative density of 99.34%. In the study by You et al. (2005), an Al_2O_3-TiC composition containing 30 wt.% TiC showed comparable results, with a hardness of 21.9 GPa, fracture toughness of 6.12 $MPa \cdot m^{1/2}$ and a relative density of 99.6%. In this study, the T30 composition had a hardness of 19.05 GPa and a fracture toughness of 4.66 $MPa \cdot m^{1/2}$.

The T40 composition showed a slightly lower density than T20 and T30, with a relative density of 98.94%. In the study by Grigoriev et al. (2018), an Al_2O_3-TiC composition with 40 vol.% TiC achieved a relative density of 99%, a hardness of 23.3 GPa and a fracture toughness of 7.8 $MPa \cdot m^{1/2}$. In this study, the T40 composition had a hardness of 20.23 GPa and a fracture toughness of 4.43 $MPa \cdot m^{1/2}$.

The T55 composition showed the highest mechanical properties in this study, with a hardness of 20.85 GPa and a fracture toughness of 5.11 $MPa \cdot m^{1/2}$. In the study by Xing et al. (2014), a composition containing 55% TiC produced by the hot-pressing method reached a hardness of 23.5 GPa and a fracture toughness of 5.04 $MPa \cdot m^{1/2}$. These values were quite close to the results of this study, although slightly higher hardness was reported in their findings.

The differences observed between studies may result from variations in sintering methods and the types of starting powders used. The density values obtained in this study were very close to the theoretical densities. The T20 and T30 compositions showed the best results in terms of relative density, indicating that porosity can be better controlled when the TiC content is low.

Fig. 3.7 shows the backscattered SEM images of the compositions at 5000x magnification. Microstructural analysis revealed that the TiC and Al_2O_3 phases were homogeneously distributed in all samples. In the SEM images, dark areas represent Al_2O_3, while light areas represent TiC. Both transgranular and intergranular crack mechanisms were observed in all samples. However, as the TiC content increased, intergranular cracks became more dominant. This suggests that a high amount of TiC weakens the grain boundaries, which may negatively affect the mechanical properties.

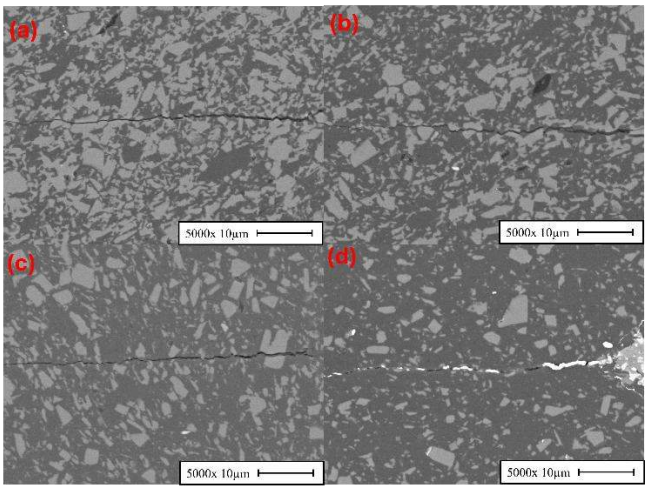

Figure 3.7. *Representative backscattered SEM images taken from polished surface of compositions (a) T55, (b) T40, (c) T30 and (d) T20*

As a result, the data obtained in this study demonstrate the characterization of Al_2O_3-TiC composites and the effect of TiC content on their microstructure and mechanical properties. The methodology used was consistent with the results of similar studies in the literature. In addition, the analysis of crack mechanisms and microstructure was successfully linked to the mechanical properties.

3.3. Effects of Sintering Parameters

The previous study obtained the best results from the sample sintered at 1900 °C for 60 minutes under 90 bar of argon atmosphere. The current study examined closed porosity points to determine the optimal sintering parameters. Samples were sintered at 1875 °C for 90 minutes and at 1900 °C for 30, 60 and 90 minutes in an argon atmosphere. Studies by Wang et al. (Wang, et al., 2023) and others suggest that adding ZrO_2 to Al_2O_3-TiC composites improves their mechanical properties. In this study, we aimed to determine the optimum weight percentage of ZrO_2. Sintering experiments were repeated by adding 3.5 wt.% and 5 wt.% ZrO_2 to the composition to evaluate its effect.

3.3.1. 1875 °C for 90 minutes under 5 bar Ar with GPS

Table 3.4 presents the dimensional changes and relative densities of composites containing 0, 3.5 and 5 wt.% ZrO_2, sintered at 1875 °C for 90 minutes under 5 bar argon atmospheres. It was observed that increasing the ZrO_2 content under the same positively

affected the sintering process. The correlation between the dimensional changes and the relative densities of the samples supports this finding.

Table 3.4. *Dimensional changes and relative densities of compositions sintered at 1875 °C for 90 minutes under 5 bar Ar*

Composites	Height (%)	Diameter (%)	Relative Density (%)
Al_2O_3-30wt.%TiC-0wt.%ZrO_2	15.34	14.73	93.91
66.5wt.%Al_2O_3-30wt.%TiC-3.5wt.%ZrO_2	17.12	15.67	94.67
65wt.%Al_2O_3-30wt.%TiC-5wt.%ZrO_2	17.46	15.88	95.25

Fig. 3.8 shows backscattered SEM images at different magnifications of the sample produced by GPS at 1875 °C under 5 bar of argon, with a 90-minute soak at peak temperature. TiC particles were seen to be uniformly distributed within the Al_2O_3 matrix. However, some coarse TiC and Al_2O_3 grains were present in the microstructure. Fig. 3.8.c and fig. 3.8.d reveals structural defects, including unclosed pores. These defects were likely due to the low-pressure sintering conditions.

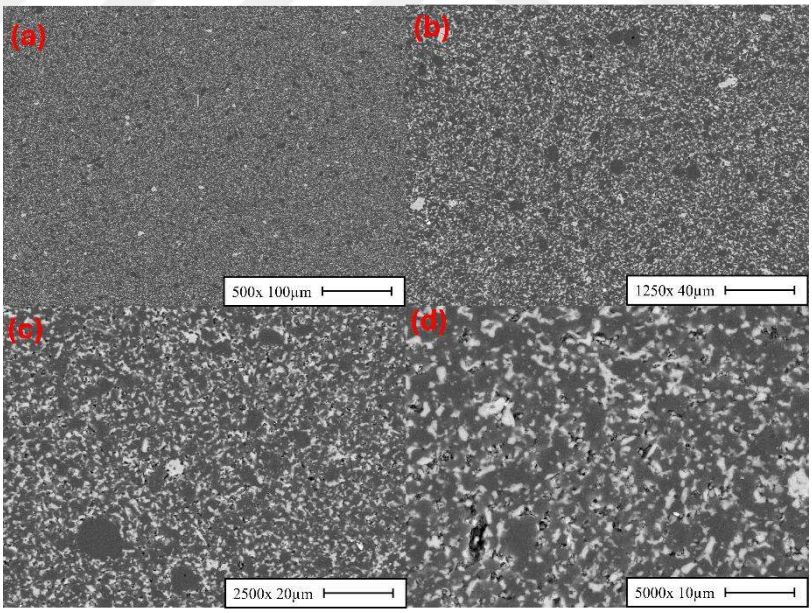

Figure 3.8. *Representative backscattered SEM images taken from polished surface of the composite contain 0wt.%ZrO_2. (a) 500x, (b) 1250x, (c) 2500x and (d) 5000x magnification.*

Fig. 3.9 shows backscattered SEM images taken from different magnifications of a composite containing 3.5 wt.% ZrO_2, produced by GPS at 1875 °C under 5 bar of argon, with a 90-minute soak at peak temperature. TiC particles (gray areas) and ZrO_2 particles

(bright areas) were uniformly distributed within the Al_2O_3 matrix (dark areas). Compared to the previous study, grain growth was significantly reduced.

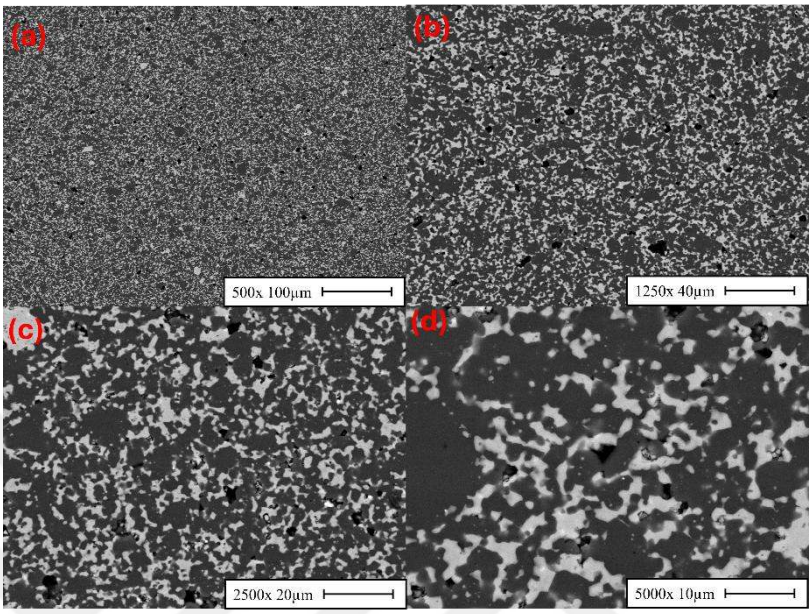

Figure 3.9. *Representative backscattered SEM images taken from polished surface of the composite contain 3.5wt.%ZrO_2. (a) 500x, (b) 1250x, (c) 2500x and (d) 5000x magnification.*

Fig. 3.10 shows the EDS analysis image and data table of the composite containing 3.5 wt.% ZrO_2. In the area scan at 1250x magnification, 2.93 wt.% Zr and 18.35 wt.% Ti were detected. This result indicates that the added ZrO_2 was homogeneously distributed throughout the structure.

Element	Weight%	Atomic%
C	6.18	10.84
O	44.28	58.34
Al	28.24	22.06
Ti	18.37	8.08
Zr	2.93	0.68

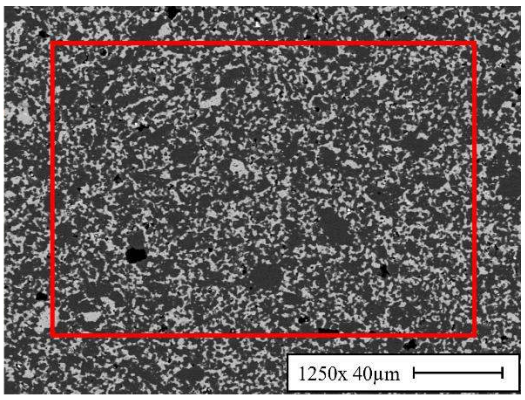

Figure 3.10. *Representative backscattered SEM image and EDS analysis taken from the polished surface of 3.5wt.%ZrO_2 composition*

Fig. 3.11 shows backscattered SEM images taken from different magnifications of a composite containing 5 wt.% ZrO_2, produced by GPS at 1875 °C under 5 bar of argon, with a 90-minute soak at the peak sintering temperature. TiC particles (gray areas) and ZrO_2 particles (bright areas) were uniformly distributed within the Al_2O_3 matrix (dark areas). Compared to previous studies, grain growth was noticeably reduced in this sample.

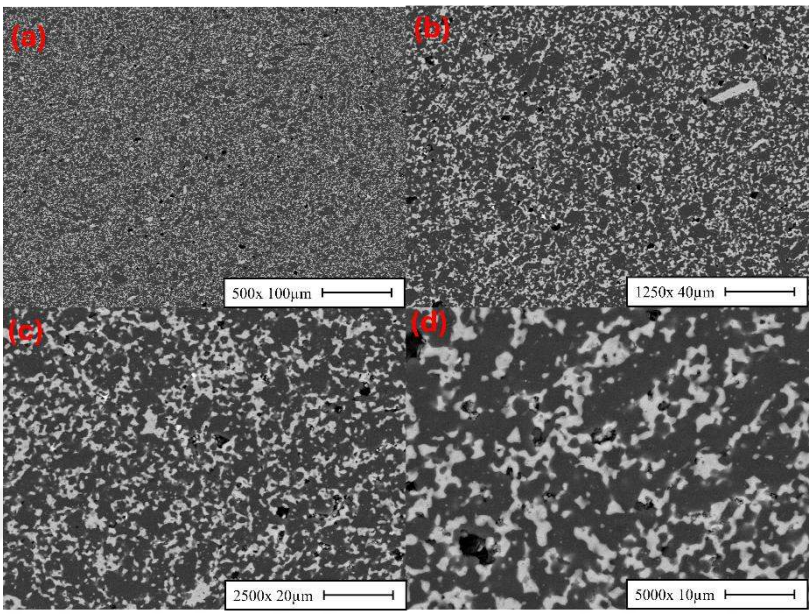

Figure 3.11. *Representative backscattered SEM images taken from polished surface of the composite contain 5wt.%ZrO_2. (a) 500x, (b) 1250x, (c) 2500x and (d) 5000x magnification.*

Fig. 3.12 shows the EDS analysis image and data table of the composite containing 5 wt.% ZrO_2. In the area scan at 1250x magnification, 1.88 wt.% Zr and 19.07 wt.% Ti were detected. This indicates that the added ZrO_2 was homogeneously distributed in the structure. However, despite the increase in ZrO_2 content in the composition, its detected amount in the EDS analysis appears lower. This suggests that ZrO_2 may have diffused or been transported within the structure during sintering.

Element	Weight%	Atomic%
C	6.85	11.92
O	44.10	57.58
Al	28.10	21.75
Ti	19.07	8.32
Zr	1.88	0.43

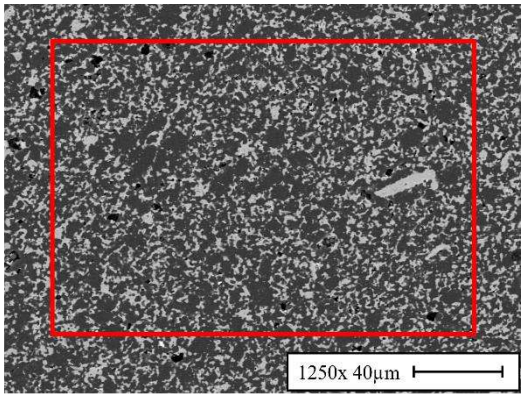

Figure 3.12. *Representative backscattered SEM image and EDS analysis taken from the polished surface of 5wt.%ZrO_2 composition*

3.3.2. 1900 °C for 90 minutes under 5 bar Ar with GPS

Table 3.5 presents the dimensional changes and relative densities of composites containing 0, 3.5 and 5 wt.% ZrO_2, sintered at 1900 °C for 90 minutes under 5 bar of argon atmosphere. Under these conditions, the addition of ZrO_2 appears to negatively affect the sintering compared to the sample without ZrO_2. Only a slight difference was observed between the samples with 3.5 wt.% and 5 wt.% ZrO_2.

Table 3.5. *Dimensional changes and relative densities of compositions sintered at 1900 °C for 90 minutes under 5 bar Ar*

Composites	Height (%)	Diameter (%)	Relative Density (%)
Al_2O_3-30wt.%TiC-0wt.%ZrO_2	16.67	12.61	96.68
66.5wt.%Al_2O_3-30wt.%TiC-3.5wt.%ZrO_2	11.41	15.14	94.63
65wt.%Al_2O_3-30wt.%TiC-5wt.%ZrO_2	11.17	15.53	94.78

Fig. 3.13 shows backscattered SEM images at different magnifications of the sample produced by GPS at 1900 °C under 5 bar of argon, with a 90-minute soak at the peak sintering temperature. TiC particles were uniformly distributed within the Al_2O_3 matrix. However, some coarse TiC and Al_2O_3 grains were still present in the microstructure. Compared to the sample sintered at 1875 °C, the microstructure appears denser, indicating that the sintering process was more effective at the higher temperature.

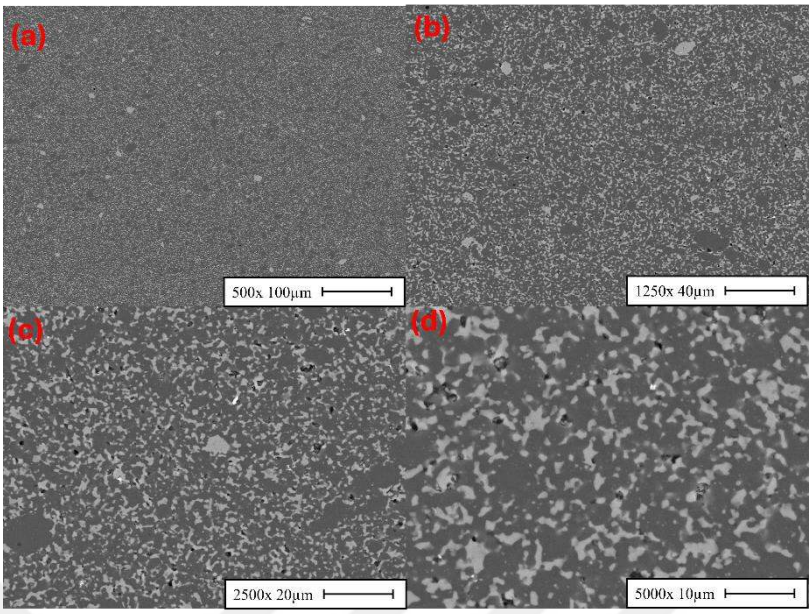

Figure 3.13. *Representative backscattered SEM images taken from polished surface of the composite contain 0wt.%ZrO_2. (a) 500x, (b) 1250x, (c) 2500x and (d) 5000x magnification.*

Fig. 3.14 shows backscattered SEM images taken from different magnifications of a composite containing 3.5 wt.% ZrO_2, produced by GPS at 1900 °C under 5 bar of argon, with a 90-minute soak at peak temperature. Compared to the previous study, grain growth and porosity increase was observed.

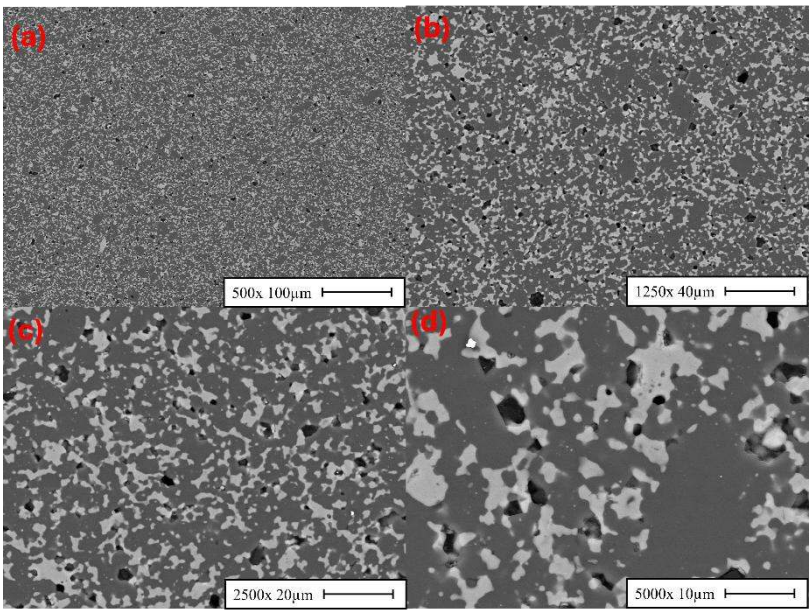

Figure 3.14. *Representative backscattered SEM images taken from polished surface of the composite contain 3.5wt.%ZrO_2. (a) 500x, (b) 1250x, (c) 2500x and (d) 5000x magnification.*

Fig. 3.15 shows the EDS analysis image and data table of the composite containing 3.5 wt.% ZrO_2. In the area scan at 1250x magnification, 2.12 wt.% Zr and 17.77 wt.% Ti were detected. This indicates that the added ZrO_2 was homogeneously distributed throughout the structure.

Element	Weight%	Atomic%
C	6.47	11.22
O	44.95	58.46
Al	28.69	22.12
Ti	17.77	7.72
Zr	2.12	0.48

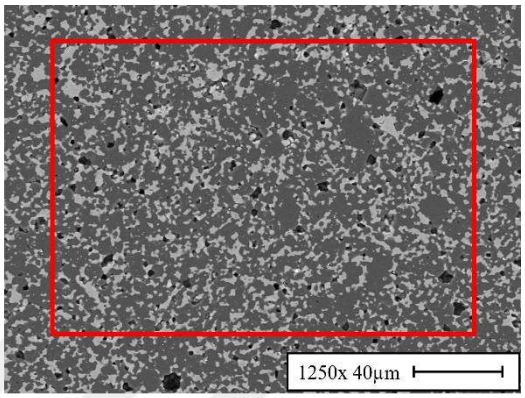

Figure 3.15. *Representative backscattered SEM image and EDS analysis taken from the polished surface of 3.5wt.%ZrO_2 composition*

Fig. 3.16 shows backscattered SEM images taken from different magnifications of a composite containing 5 wt.% ZrO_2, produced by GPS at 1900 °C under 5 bar of argon, with a 90-minute soak at peak temperature. The grain growth and porosity levels were similar to those observed in the previous study. The dimensional change and relative density results support this observation.

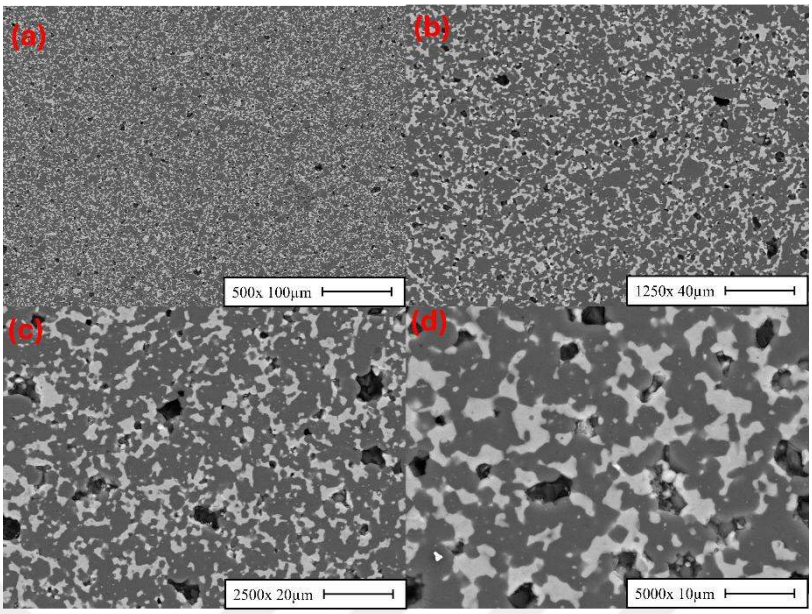

Figure 3.16. *Representative backscattered SEM images taken from polished surface of the composite contain 5wt.%ZrO_2. (a) 500x, (b) 1250x, (c) 2500x and (d) 5000x magnification.*

Fig. 3.17 shows the EDS analysis image and data table of the composite containing 5 wt.% ZrO_2. In the area scan at 1250x magnification, 3.23 wt.% Zr and 18.13 wt.% Ti were detected.

Element	Weight%	Atomic%
C	6.19	10.95
O	42.82	56.9
Al	29.64	23.35
Ti	18.13	8.05
Zr	3.23	0.75

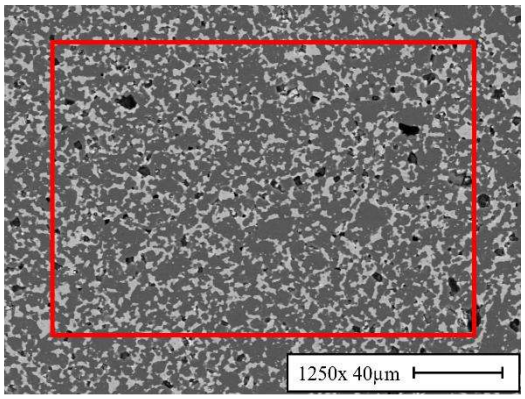

Figure 3.17. *Representative backscattered SEM image and EDS analysis taken from the polished surface of 5wt.%ZrO_2 composition*

3.3.3. 1900 °C for 60 minutes under 5 bar Ar with GPS

Table 3.6 presents the dimensional changes and relative densities of composites containing 0, 3.5 and 5 wt.% ZrO_2, sintered at 1900 °C for 60 minutes under 5 bar argon atmospheres. Under these conditions, the addition of ZrO_2 appears to have a negative

effect on the sintering process compared to the sample without ZrO_2. However, only a slight difference was observed between the 3.5 wt.% and 5 wt.% ZrO_2 additions.

Table 3.6. *Dimensional changes and relative densities of compositions sintered at 1900 °C for 60 minutes under 5 bar Ar*

Composites	Height (%)	Diameter (%)	Relative Density (%)
Al_2O_3-30wt.%TiC-0wt.%ZrO_2	14.26	14.63	94.75
66.5wt.%Al_2O_3-30wt.%TiC-3.5wt.%ZrO_2	14.44	15.52	95.09
65wt.%Al_2O_3-30wt.%TiC-5wt.%ZrO_2	15.04	14.33	94.37

Fig. 3.18 shows backscattered SEM images at different magnifications of the sample produced by GPS at 1900 °C under 5 bar of argon, with a soak time of 60 minutes at the peak sintering temperature. Compared to the previous study with a 90-minute soak, an increase in porosity was observed.

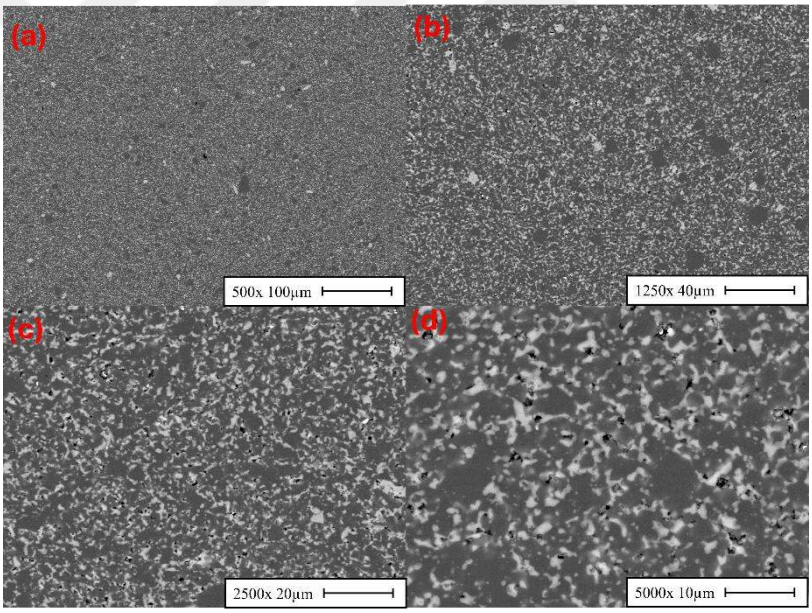

Figure 3.18. *Representative backscattered SEM images taken from polished surface of the composite contain 0wt.%ZrO_2. (a) 500x, (b) 1250x, (c) 2500x and (d) 5000x magnification.*

Fig. 3.19 shows backscattered SEM images taken from different magnifications of a composite containing 3.5 wt.% ZrO_2, produced by GPS at 1900 °C under 5 bar of argon, with a 60-minute soak at peak temperature. The addition of ZrO_2 at this temperature and duration affects the microstructure positively.

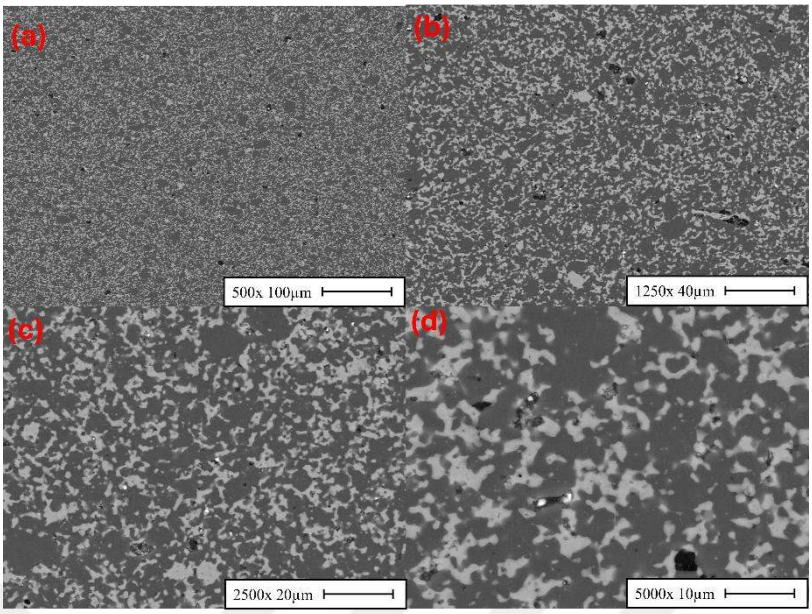

Figure 3.19. *Representative backscattered SEM images taken from polished surface of the composite contain 3.5wt.%ZrO_2. (a) 500x, (b) 1250x, (c) 2500x and (d) 5000x magnification.*

Fig. 3.20 shows the EDS analysis image and data table of the composite containing 3.5 wt.% ZrO_2. In the area scan at 1250x magnification, 1.72 wt.% Zr and 18.57 wt.% Ti were detected.

Element	Weight%	Atomic%
C	7.84	13.53
O	43.27	56.07
Al	28.60	21.98
Ti	18.57	8.04
Zr	1.72	0.39

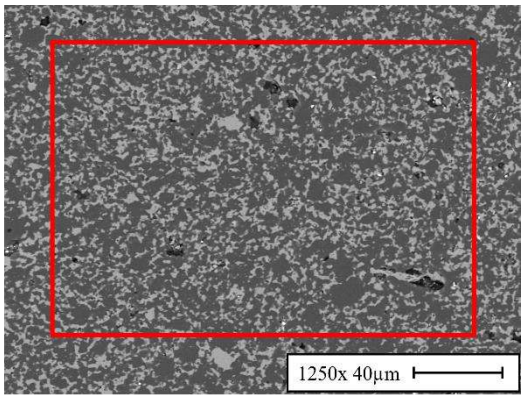

Figure 3.20. *Representative backscattered SEM image and EDS analysis taken from the polished surface of 3.5wt.%ZrO_2 composition*

Fig. 3.21 shows backscattered SEM images at different magnifications of a composite containing 5 wt.% ZrO_2, produced by GPS at 1900 °C under 5 bar of argon, with a 60-minute soak at peak temperature. The change in ZrO_2 content appears to have a minimal effect on the microstructure, as supported by the dimensional change and relative density results.

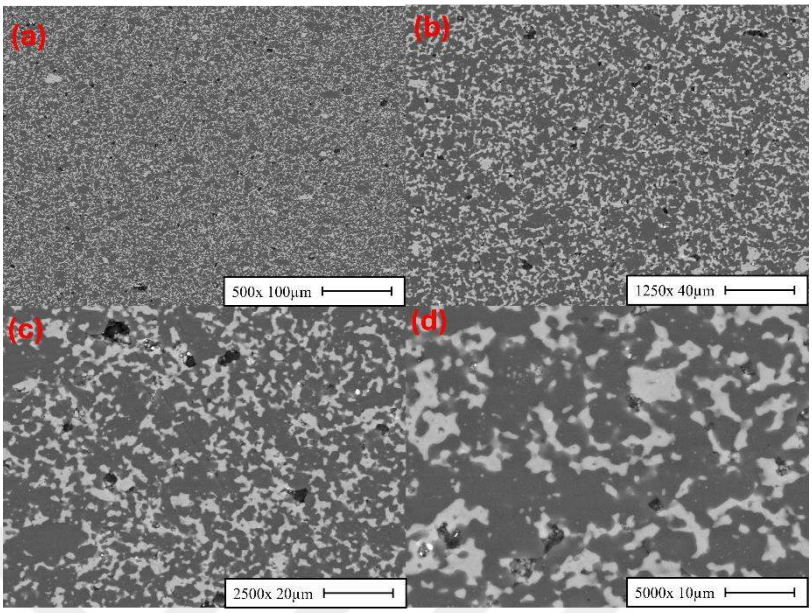

Figure 3.21. *Representative backscattered SEM images taken from polished surface of the composite contain 5wt.%ZrO_2. (a) 500x, (b) 1250x, (c) 2500x and (d) 5000x magnification.*

Fig. 3.22 shows the EDS analysis image and data table of the composite containing 5 wt.% ZrO_2. In the area scan at 1250x magnification, 2.93 wt.% Zr and 19.74 wt.% Ti were detected.

Element	Weight%	Atomic%
C	7.44	13.02
O	43.29	56.9
Al	26.61	20.74
Ti	19.74	8.67
Zr	2.93	0.67

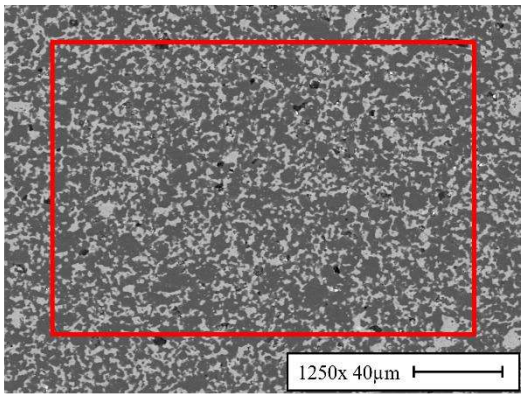

Figure 3.22. *Representative backscattered SEM image and EDS analysis taken from the polished surface of 5wt.%ZrO_2 composition*

3.3.4. 1900 °C for 30 minutes under 5 bar Ar with GPS

Table 3.7 presents the dimensional changes and relative densities of composites containing 0, 3.5 and 5 wt.% ZrO_2, sintered at 1900 °C for 60 minutes under 5 bar argon atmospheres. Under these conditions, the addition of ZrO_2 appears to have a negative

effect on the sintering process compared to the sample without ZrO_2. However, only a slight difference was observed between the 3.5 wt.% and 5 wt.% ZrO_2 additions.

Table 3.7. *Dimensional changes and relative densities of compositions sintered at 1900 °C for 30 minutes under 5 bar Ar*

Composites	Height (%)	Diameter (%)	Relative Density (%)
Al_2O_3-30wt.%TiC-0wt.%ZrO_2	14.29	15.42	96.05
66.5wt.%Al_2O_3-30wt.%TiC-3.5wt.%ZrO_2	13.75	15.31	95.56
65wt.%Al_2O_3-30wt.%TiC-5wt.%ZrO_2	14.89	14.87	95.40

Fig. 3.23 shows backscattered SEM images at different magnifications of the sample produced by GPS at 1900 °C under 5 bar of argon, with a 60-minute soak at the peak sintering temperature. Compared to the previous study with a 90-minute soak, an increase in porosity was observed.

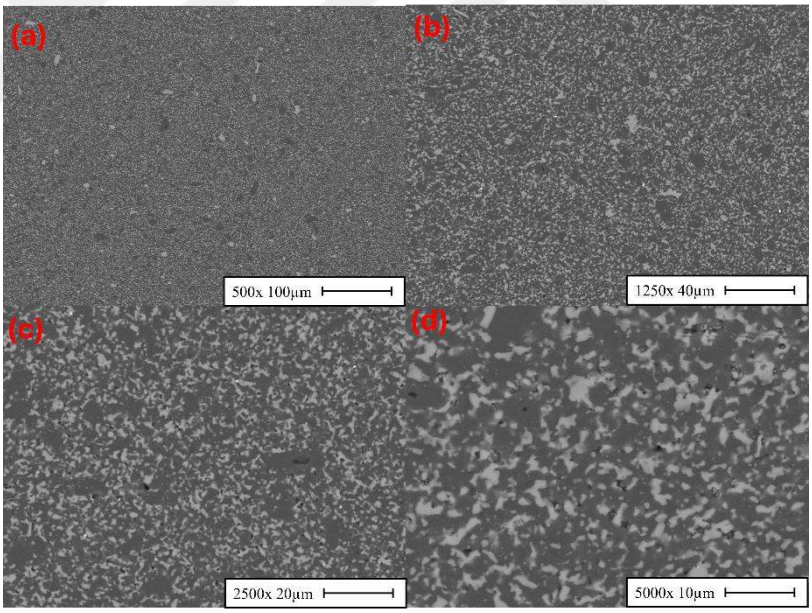

Figure 3.23. *Representative backscattered SEM images taken from polished surface of the composite contain 0wt.%ZrO_2. (a) 500x, (b) 1250x, (c) 2500x and (d) 5000x magnification.*

Fig. 3.24 shows backscattered SEM images at different magnifications of a composite containing 3.5 wt.% ZrO_2, produced by GPS at 1900 °C under 5 bar of argon, with a 60-minute soak at peak temperature. At this temperature and duration, the addition of ZrO_2 appears to have a positive effect on the microstructure.

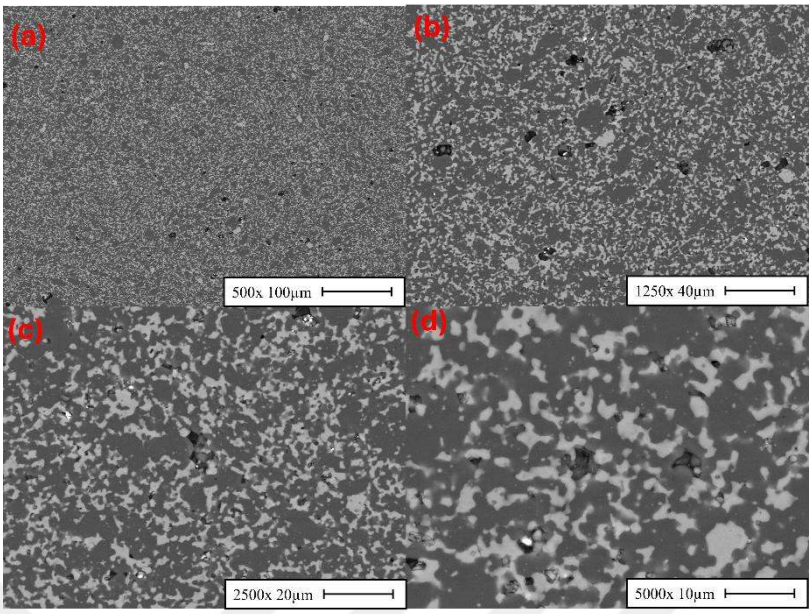

Figure 3.24. *Representative backscattered SEM images taken from polished surface of the composite contain 3.5wt.%ZrO_2. (a) 500x, (b) 1250x, (c) 2500x and (d) 5000x magnification.*

Fig. 3.25 shows the EDS analysis image and table of the composite contain 3.5wt.% ZrO_2. 1.72 wt.% Zr and 17.27 wt.% Ti was found in the area scan at 1250x magnification.

Element	Weight%	Atomic%
C	5.84	10.14
O	44.74	58.39
Al	30.42	23.54
Ti	17.27	7.53
Zr	1.72	0.39

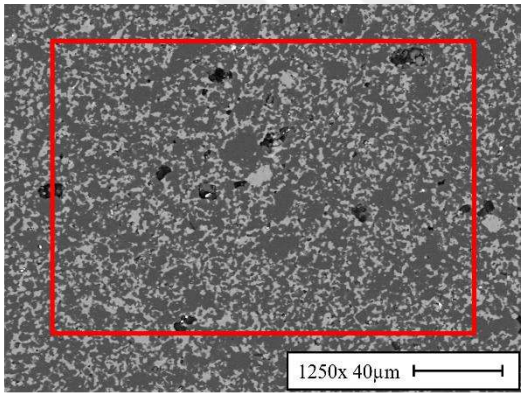

Figure 3.25. *Representative backscattered SEM image and EDS analysis taken from the polished surface of 3.5wt.%ZrO_2 composition*

Fig. 3.26 shows backscattered SEM images at different magnifications of a composite containing 5 wt.% ZrO_2, produced by GPS at 1900 °C under 5 bar of argon, with a 30-minute soak at peak temperature. The change in ZrO_2 content appears to have a minimal effect on the microstructure, as supported by the dimensional change and relative density results.

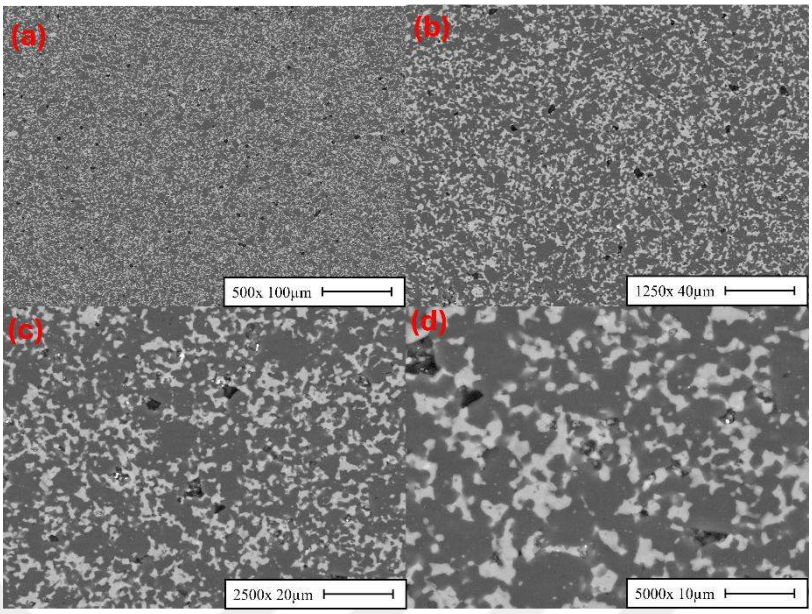

Figure 3.26. *Representative backscattered SEM images taken from polished surface of the composite contain 5wt.%ZrO_2. (a) 500x, (b) 1250x, (c) 2500x and (d) 5000x magnification.*

Fig. 3.27 shows the EDS analysis image and table of the composite contain 5wt.% ZrO_2. 2.38 wt.% Zr and 17.04 wt.% Ti was found in the area scan at 1250x magnification.

Element	Weight%	Atomic%
C	8.35	14.36
O	43.14	55.70
Al	28.74	22.01
Ti	17.04	7.35
Zr	2.38	0.54

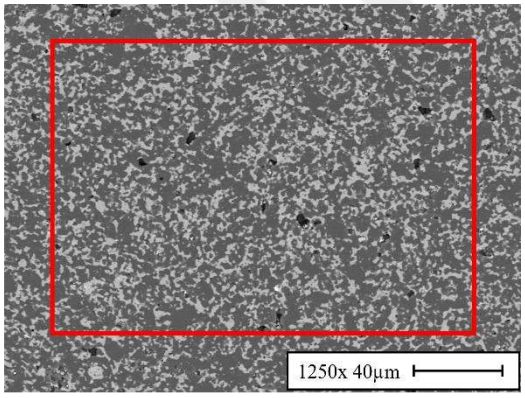

Figure 3.27. *Representative backscattered SEM image and EDS analysis taken from the polished surface of 5wt.%ZrO_2 composition*

3.3.5. Comparison of Sintering Parameters Results

Fig. 3.28 shows the relative densities, sintering temperatures and peak temperature durations of the compositions containing 0, 3.5 and 5 wt.% ZrO_2, sintered at 1875 °C for 90 minutes and 1900 °C for 30, 60 and 90 minutes.

The best relative density (95.4%) was obtained from the composition with 3.5 wt.% ZrO_2 sintered at 1900 °C for 30 minutes. The lowest relative density (93.91%) was

observed in the sample without ZrO_2, sintered at 1875 °C for 90 minutes. This indicates that lower sintering temperatures did not provide sufficient densification.

Similarly, the highest relative density (96.68%) among the compositions without ZrO_2 was achieved at 1900 °C for 90 minutes. These results show that higher temperatures and longer durations lead to better densification.

When evaluated by composition:

- Al_2O_3–TiC–0 wt.% ZrO_2: Highest density of 96.68% at 1900 °C for 90 minutes.
- Al_2O_3–TiC–3.5 wt.% ZrO_2: Reached 95.56% at 1900 °C for 30 minutes.
- Al_2O_3–TiC–5 wt.% ZrO_2: Reached 95.4% at 1900 °C for 30 minutes.

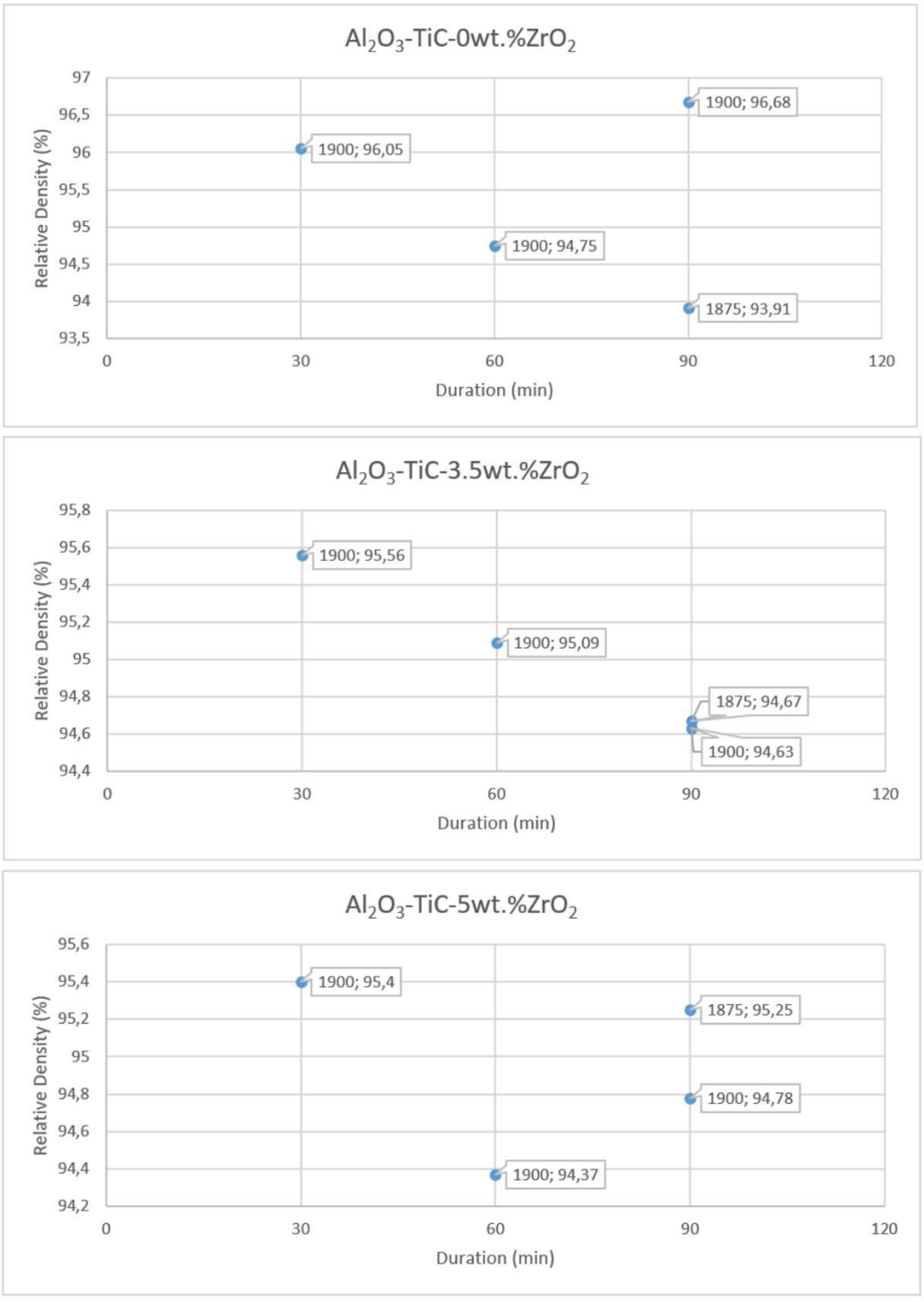

Figure 3.28. *Representative relative density vs duration graphics of 0-3.5-5 wt.% ZrO_2 contain Al_2O_3-TiC compositions sintered at 1875 °C and 1900 °C for 30-60-90 minutes under 5 bar Ar atmosphere*

3.4. Effect of Pressing Pressure and Interaction with Crucible on Sintering Behavior

The best result was obtained from the composition containing 3.5 wt.% ZrO_2, sintered at 1900 °C for 30 minutes in the previous study. Holding the temperature for 45 minutes was predicted to give better results. In this study, sintering was carried out at 1900 °C for 45 minutes under 90 bar of argon atmosphere, using different pressing pressures and various sintering crucibles.

The goal was to determine the minimum pressing pressure required to achieve a relative density above 99%. Ayas et al. (Ayas, 2003) reported that, during sintering in BN crucibles, TiC in the structure migrated to the surface and formed TiB_2. To avoid this unwanted reaction and observe the effect of crucible type, additional sintering experiments were conducted using BN and graphite crucibles under the same conditions.

Two different sample groups were created to observe the effects of pressing pressure and the sintering crucible. In the first group, the samples were pressed at 50 to 600 MPa pressures. Samples labeled with “P" were pressed using an automatic press (Komage, S-20XT, Germany), while those labeled with only numbers were first pressed with a hand press and then further compacted using Cold Isostatic Pressing (CIP) at 2000 bar.

Table 3.8 compares the green density (before sintering) and relative density (after sintering) of samples pressed under different pressures. An increase in green density was observed with higher pressing pressures. For example, the green density of the sample pressed at 50 MPa was 47.29% and gradually increased to 62.86% at 600 MPa.

Relative density values show that samples pressed at lower pressures, such as sample 1, had lower density (94.06%), while sample 7P, pressed at 200 MPa, reached around 99%. Sample 2P, pressed at 350 MPa, achieved a relative density of 99.13%. The highest value, 99.35%, was observed in sample 19P, which was pressed at 500 MPa. However, a slight decrease in relative density was seen in samples 20P (540 MPa) and 10P (600 MPa), with values of 99.14% and 98.54%, respectively. This trend suggests excessive pressure may cause mechanical deformation during sintering, slightly reducing densification.

When examining changes in the diameter and height of the samples, it was observed that higher pressing pressure caused more shrinkage in diameter. For example, sample 1 (pressed at 50 MPa) showed a diameter change of 20.11%, while sample 19P (pressed at 500 MPa) showed a smaller change of 16%. Similarly, the height changes in sample 1

were 19.35%, whereas in sample 20P it was 12.10%. These results suggest that higher pressing pressures lead to more uniform shrinkage during sintering and better pore closure. However, the slight decrease in relative density observed in highly pressed samples (20P and 10P) indicates that excessive pressure may cause internal stress or micro-cracks, negatively affecting densification.

Table 3.8. *Al_2O_3-TiC-3.5wt.%ZrO_2 composition pressed at different pressures and sintered with a BN crucible*

		Before GPS	After GPS		
Sample Name	**Applied Pressure (MPa)**	**Green Body Density (%)**	**Diameter (%)**	**Height (%)**	**Relative Density (%)**
1	50	47.29	20.11	19.35	94.06
2	100	50.96	19.15	17.40	98.27
3	130	52.50	17.56	19.12	98.65
4	175	53.98	17.57	17.98	98.73
5	220	55.28	16.97	15.76	98.80
6	260	55.51	16.26	17.79	99.01
7P	200	57.71	17.51	17.12	99.01
4P	320	59.81	15.03	14.75	99.07
2P	350	60.30	16.26	13.20	99.13
16P	410	60.71	15.89	14.24	99.19
14P	450	61.31	16.26	14.18	99.30
19P	500	61.70	16.00	14.12	99.35
20P	540	62.27	15.69	12.10	99.14
10P	600	62.86	15.70	12.59	98.54

Table 3.9 compares the density and dimensional changes of the Al_2O_3–TiC–3.5 wt.% ZrO_2 composite after sintering in a graphite crucible under different pressing pressures. As the pressing pressure increases, the green body density of the samples also increases. For example, sample 8P (pressed at 220 MPa) had a green density of 58.24%, while sample 17P (pressed at 480 MPa) reached 61.67%. This trend indicates that higher pressing pressure improves particle packing efficiency.

Increasing the pressing pressure leads to higher green density and an increase in relative density up to approximately 99.49%. However, beyond 320 MPa, the improvement in relative density becomes minimal. The optimal pressing pressure range was between 320 and 360 MPa.

Table 3.9. *Al_2O_3-TiC-3.5wt.%ZrO_2 composition pressed at different pressures and sintered with a graphite crucible*

		Before GPS	After GPS		
Sample Name	**Applied Pressure (MPa)**	**Green Body Density (%)**	**Diameter (%)**	**Height (%)**	**Relative Density (%)**
8P	220	58.24	17.43	11.97	99.41
11P	320	59.75	17.24	15.77	99.43
1P	335	60.10	15.93	14.99	99.37
3P	357	60.15	16.50	14.14	99.36
12P	360	60.39	17.32	15.51	99.47
15P	435	61.08	18.73	15.65	99.41
17P	480	61.67	17.24	16.06	99.49

Fig. 3.29 shows backscattered SEM images of Sample 2, sintered in a BN crucible, taken at different magnifications. Pores indicate incomplete densification during sintering, likely due to insufficient pressing pressure.

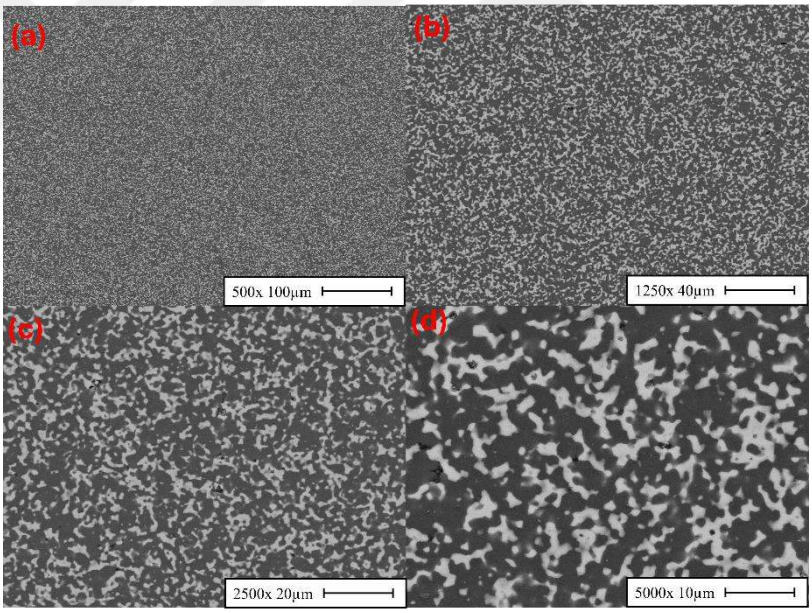

Figure 3.29. *Representative backscattered SEM images taken from polished surface of Sample 2 (pressed at 100 MPa) sintered in a BN crucible at different magnifications.*

Fig. 3.30 shows backscattered SEM images of Sample 7P, sintered in a BN crucible, taken at different magnifications. As seen in Fig. 3.30, applying a moderate pressing pressure of 200 MPa significantly improves densification during sintering and reduces porosity. A homogeneous distribution of TiC particles within the Al_2O_3 matrix was also observed.

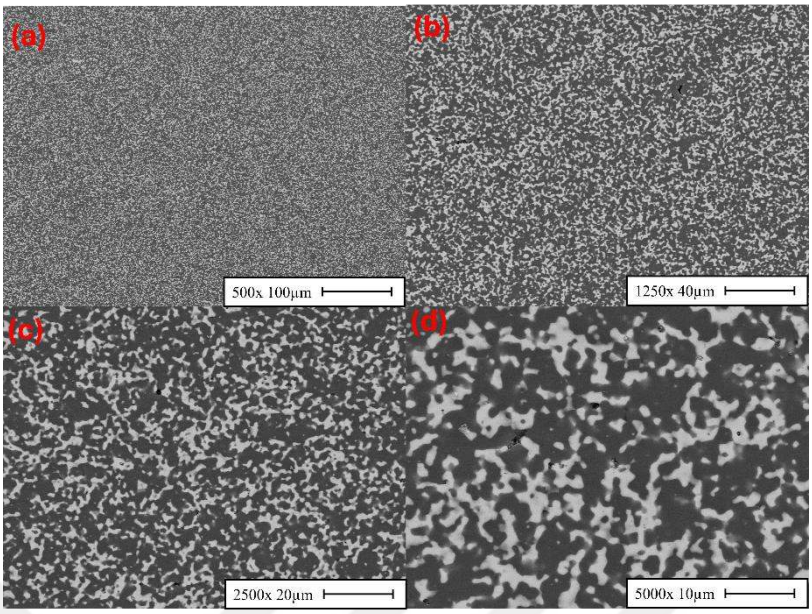

Figure 3.30. *Representative backscattered SEM images taken from polished surface of Sample 7P (pressed at 200 MPa) sintered in a BN crucible at different magnifications.*

Fig. 3.31 shows backscattered SEM images of Sample 2P, sintered in a BN crucible, taken at different magnifications. It is clearly seen that a high pressure of 350 MPa significantly improves both the density and microstructural homogeneity after sintering. TiC particles were more uniformly distributed within the Al_2O_3 matrix and the number of pores was greatly reduced.

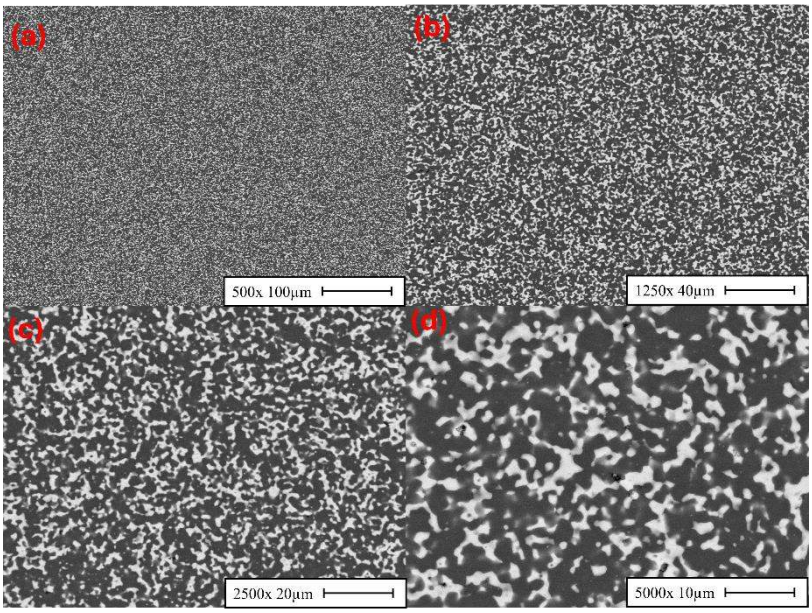

Figure 3.31. *Representative backscattered SEM images taken from polished surface of Sample 2P (pressed at 350 MPa) sintered in a BN crucible at different magnifications.*

Fig. 3.32 shows backscattered SEM images of Sample 3P, sintered in a graphite crucible, taken at different magnifications. The results indicate that a high pressure of 350 MPa significantly improves density and microstructural homogeneity after sintering. The graphite crucible exhibits lower chemical interaction with the material, helping preserve the microstructure's purity. The reduced pore size suggests that the sintering process was completed and the use of a graphite crucible contributed to this outcome. The combination of 350 MPa pressing pressure and a graphite crucible can be considered an ideal process for achieving both high density and a homogeneous microstructure.

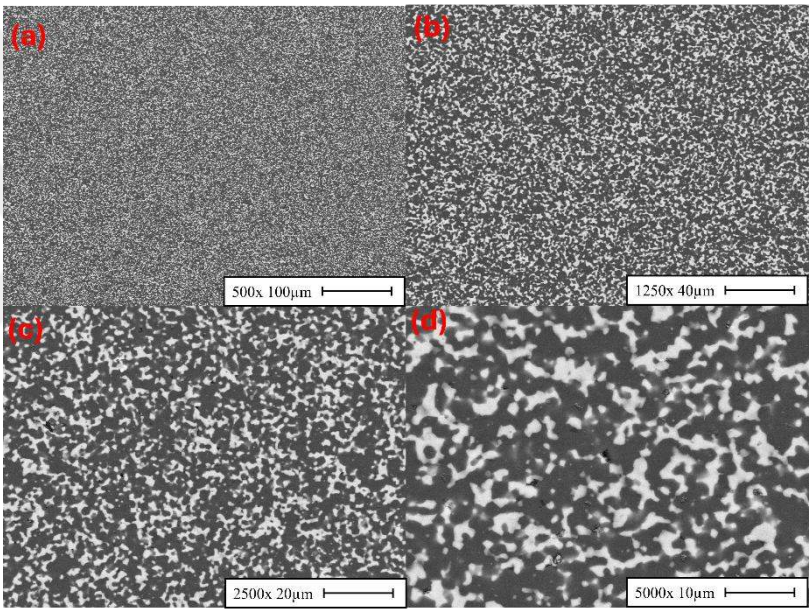

Figure 3.32. *Representative backscattered SEM images taken from polished surface of Sample 3P (pressed at ~350 MPa) sintered in a graphite crucible at different magnifications.*

Fig. 3.33 shows edge SEM images taken at 250x magnification of samples pressed at 100, 200 and 350 MPa and sintered in a BN crucible, along with a sample pressed at 350 MPa and sintered in a graphite crucible. The sample pressed at 100 MPa exhibited lower relative density than the others and its SEM image clearly shows a significant amount of porosity. The samples pressed at 200 MPa and 350 MPa achieved a relative density of 99% or higher, which was supported by the edge SEM images. However, both samples display a thin surface layer, likely formed due to the interaction with the BN crucible during sintering. A similar layer was observed in the sample sintered in the

graphite crucible, although the thickness and composition of the layer appear to be different.

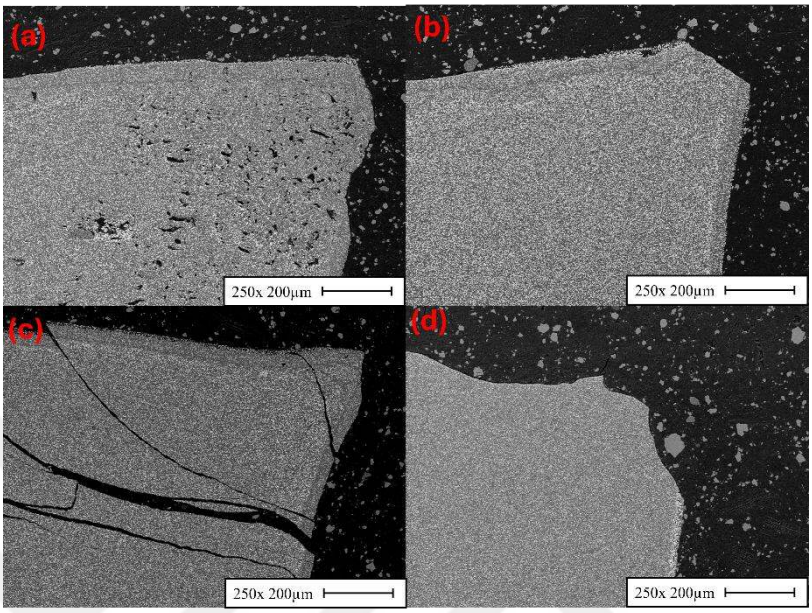

Figure 3.33. *Representative backscattered SEM images taken from polished surface of Sample 2, 7P, 2P and 3P*

Fig. 3.34 shows SEM images taken at 1250x magnification of the same samples. A closer examination of the thin surface layer reveals that the samples sintered in the BN crucible have an approximate layer thickness of 30 µm. The sample sintered in the graphite crucible has a thinner layer of around 16 µm. Unexpectedly, the sample pressed at 200 MPa shows signs of distortion. As seen in the SEM image in Fig. 3.34, the thin layer at the edge extends toward the corner, reaching a thickness of approximately 60 µm. This phenomenon was observed only in samples pressed with the automatic press and sintered in the BN crucible.

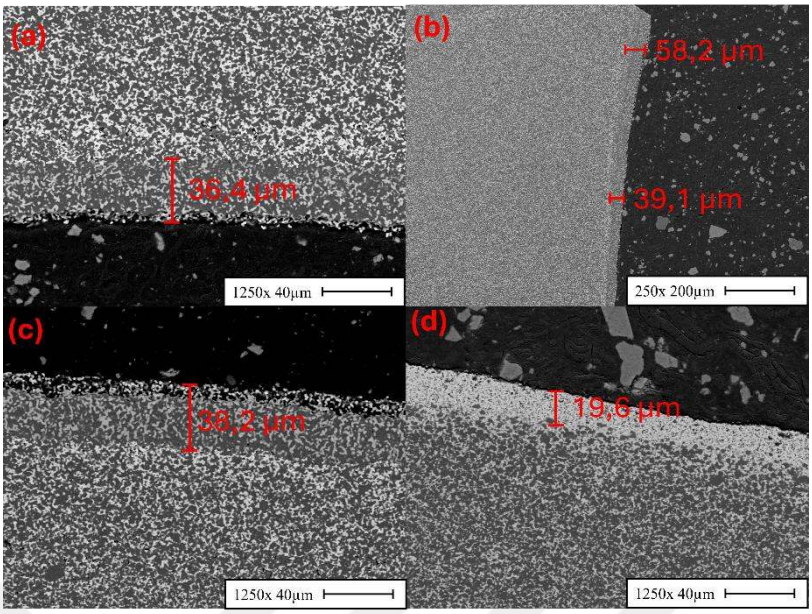

Figure 3.34. *Representative backscattered SEM images taken from polished surface of the edge layer of Sample 2, 7P, 2P and 3P*

Fig. 3.35 shows the results of EDS analyses conducted on the edge of Sample 2P (pressed at 350 MPa and sintered in the BN crucible). The EDS results confirm the presence of boron (B), originating from the BN crucible, in the outer region of the thin surface layer. Additionally, the accumulation of titanium at the boundary (highlighted in green) was confirmed through EDS analysis. As the analysis moves from this boundary toward the center of the sample, the EDS results begin to show similar compositions, indicating a gradual transition in material distribution.

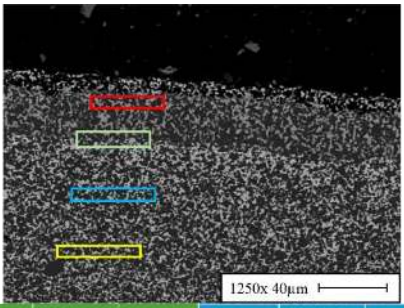

Elements	Weight %	Atomic %
C	3.29	4.62
O	30.48	32.15
Al	20.35	12.73
Ti	15.35	5.41
Zr	1.87	0.35
B	28.66	44.74

Elements	Weight %	Atomic %
C	5.15	9.44
O	40.59	55.88
Al	28.15	22.98
Ti	24.67	11.34
Zr	1.45	0.35

Elements	Weight %	Atomic %
C	5.49	9.60
O	44.57	58.53
Al	30.40	23.67
Ti	17.73	7.78
Zr	1.82	0.42

Elements	Weight %	Atomic %
C	6.00	10.61
O	43.57	57.81
Al	28.00	22.03
Ti	20.57	9.12
Zr	1.86	0.43
B	0	0

Figure 3.35. *Representative backscattered SEM image and EDS analysis taken from the polished surface of Sample 2P*

XRD analysis of Sample 2P sintered in BN crucible showed that TiB_2 peaks were evident and γ-Al_2O_3 and a small amount of C were present as accompanying phases in Fig. 3.36. This finding was consistent with literature studies showing TiC migrates to the surface and forms TiB_2 during sintering in a BN crucible. Therefore, this study also used graphite crucibles with BN crucibles to investigate the crucible effect comparatively. In the fig. 3.34 and fig. 3.35, it was observed that a reaction layer approximately 30 µm thick was formed in the BN crucible and this layer thickened towards the corners in the sample prepared with an automatic press at 200 MPa. This layer thickness and compositional differentiation clearly reveal the chemical interaction with BN.

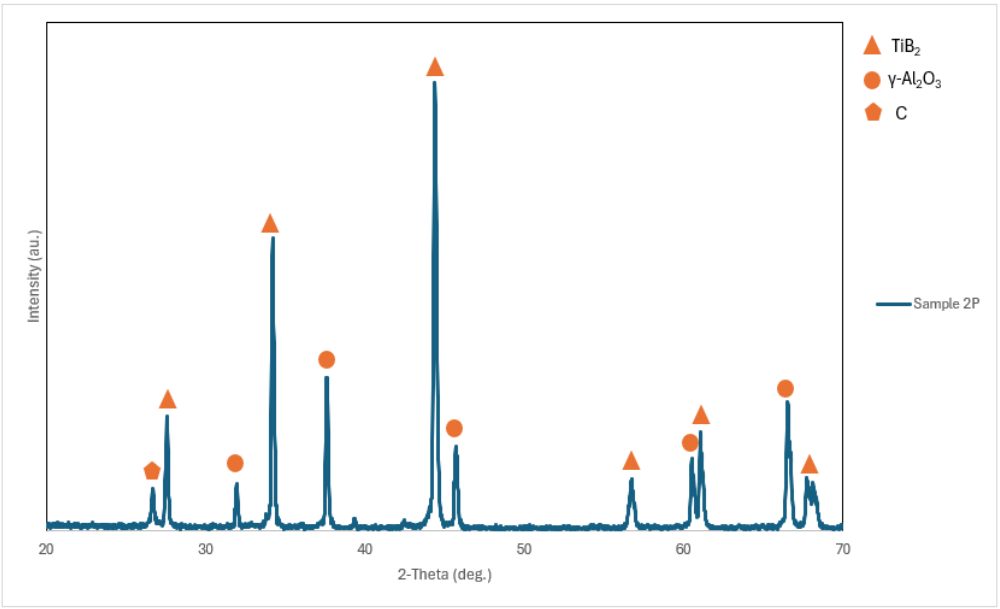

Figure 3.36. *Representative XRD analysis of Sample 2P*

Fig. 3.37 shows the results of EDS analyses conducted on the edge of Sample 3P (pressed at 350 MPa and sintered in a graphite crucible). Unlike the sample sintered in the BN crucible, this sample displays a thinner surface layer. The layer contains a high concentration of titanium. It was believed that an interaction occurred between the carbon from the graphite crucible and the titanium within the sample's microstructure.

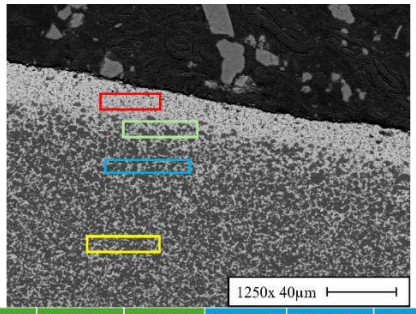

Elements	Weight %	Atomic %	Elements	Weight %	Atomic %	Elements	Weight %	Atomic %	Elements	Weight %	Atomic %
C	18.55	47.40	C	7.86	14.65	C	7.03	12.73	C	6.16	11.15
O	1.76	3.38	O	36.58	51.17	O	38.27	52.04	O	38.43	52.23
Al	0.37	0.42	Al	24.02	19.92	Al	30.61	24.69	Al	33.13	26.70
Ti	72.17	46.24	Ti	29.39	13.73	Ti	22.23	10.10	Ti	21.37	9.70
Zr	6.79	2.28	Zr	2.15	0.53	Zr	1.86	0.44	Zr	0.91	0.22

Figure 3.37. *Representative backscattered SEM image and EDS analysis taken from the polished surface of Sample 3P*

In Fig. 3.38, XRD analysis of Sample 3P revealed that the main phases were preserved as Al_2O_3, TiC and ZrO_2 and boride formation was not observed. This result was consistent with the microstructural observations that the graphite crucible gives lower chemical interaction with the material. The layer formed in the graphite crucible at the edge region was thinner than BN (16 µm). This indicates that the crucible induced reactions were limited.

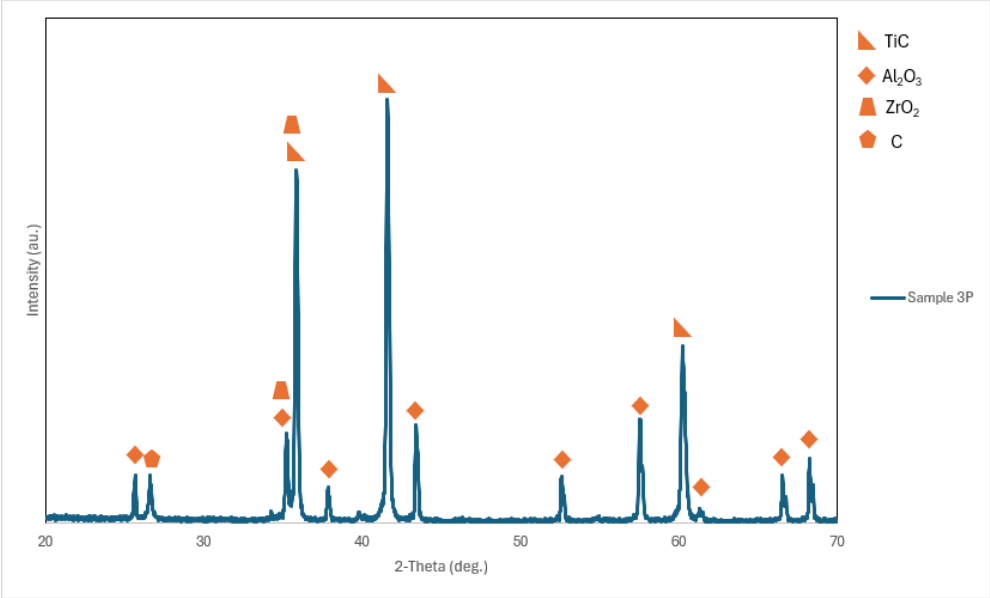

Figure 3.38. *Representative XRD analysis of Sample 3P*

3.4.1. Comparison of Pressing Parameters Results

Fig. 3.39 shows the relationship between pressing pressure and both green density and relative density. In the first graph, it was clearly observed that green density continuously increases with rising pressing pressure. While green density remains low at lower pressures (below 50%), it rises rapidly as the pressure increases and tends to level off around 600 MPa. This indicates that higher pressing pressures enable tighter particle packing within the sample and help reduce initial porosity.

The second graph shows the effect of pressure on relative density. A sharp increase in relative density was observed with pressure increases up to 100 MPa, rising from 94% to 98%. After this point, the density values begin to stabilize. Around 350 MPa, relative density reaches approximately 99% and this level was maintained with only slight increases at higher pressures. However, a slight decrease in relative density was seen to be beyond 500 MPa. This suggests that very high pressing pressures may cause mechanical deformation in the microstructure or trigger local reactions during sintering.

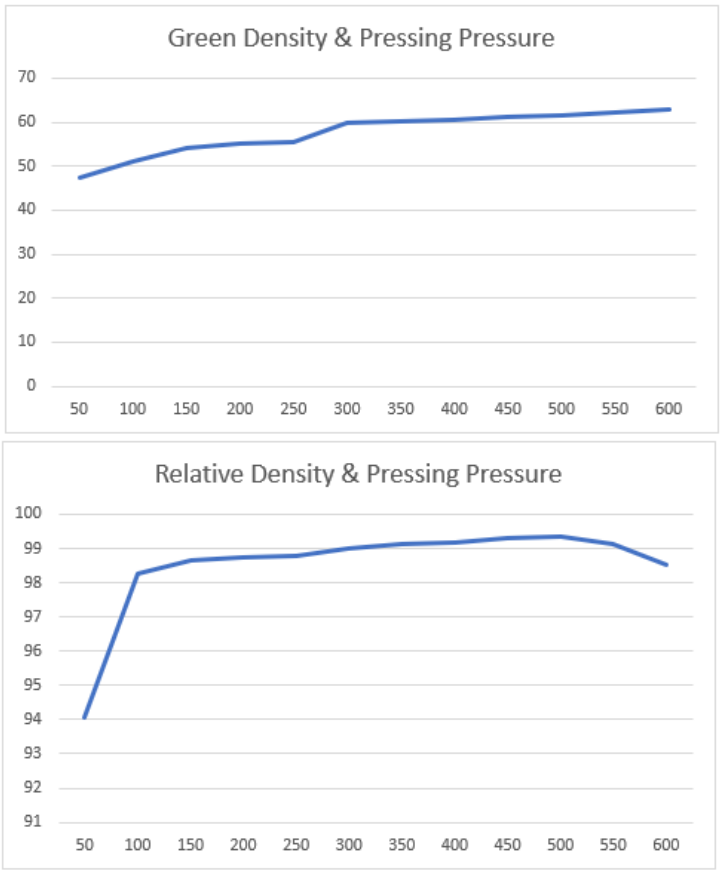

Figure 3.39. *Representative green density vs. pressing pressure and relative density vs. pressing pressure graphic of samples*

As a result, high pressures clearly improve green density. However, for relative density, the optimal pressing pressure was in the range of 200–350 MPa. Pressures of 500 MPa and above do not increase density further and may cause a slight decrease. These graphs indicate that the ideal pressing pressure range for an efficient sintering process was between 200 and 350 MPa, providing the best green and relative density results.

3.5. Prototype production with GPS and resintering studies

This study investigates different sintering setups to improve the density and microstructural properties of the Al_2O_3 (66.5 wt.%) – TiC (30 wt.%) – ZrO_2 (3.5 wt.%) composition, referred to as ATZ. Initially, high density was achieved in individual samples through the controlled use of carbon sheets. Based on these results, mass production trials were conducted. However, increasing the amount of carbon sheets had negative effects. In the final approach, the carbon sheet was completely removed and dummy samples were used instead leading to more positive results in density. This study shows that optimizing sample arrangement and layout during the sintering process plays a critical role in improving the performance of the ATZ composite.

Table 3.10 compares parameters such as relative density and shrinkage rates after sintering under different pressing pressures. It was observed that green density generally increases with higher pressing pressure, which in turn improves relative density after sintering. Diameter and length shrinkage occurred at similar rates, ranging between approximately 16–18%. Relative density values were between 99.45% and 99.68%. These results show that pressing pressure and sintering conditions directly affect density and that a nearly fully dense structure can be achieved under optimal parameters.

Table 3.10. *ATZ composition RPGX 3V geometry pressed at different pressures and sintered with a graphite crucible*

		Before GPS	After GPS		
Sample Name	**Applied Pressure (MPa)**	**Green Body Density (%)**	**Diameter (%)**	**Height (%)**	**Relative Density (%)**
7 - RPGX 3V	352	55.10	16.86	16.95	99.49
9 - RPGX 3V	338	54.99	16.69	16.98	99.59
10 - RPGX 3V	307	54.60	17.70	18.43	99.68
16 - RPGX 3V	320	54.58	17.36	17.17	99.57
17 - RPGX 3V	311	54.46	17.69	18.00	99.45
20 - RPGX 3V	323	54.71	17.75	18.14	99.50

Table 3.11 presents the results for properties such as relative density and shrinkage after sintering samples produced in two different geometries (RPGX 3V and SNMN) under varying pressures in an environment with excess carbon sheet. From the table, it was observed that green density generally increases with pressing pressure. However, the presence of excess carbon sheet leads to a decrease in relative density. Due to this negative effect, relative density values mostly remained between 90% and 92% and did not reach the desired 99% level.

Table 3.11. *ATZ composition RPGX 3V and SNMN geometry pressed at different pressures and sintered with a graphite crucible*

		Before GPS	After GPS		
Sample Name	**Applied Pressure (MPa)**	**Green Body Density (%)**	**Diameter (%)**	**Height (%)**	**Relative Density (%)**
35 - RPGX 3V	299	54.35	15.65	15.87	94.05
36 - RPGX 3V	368	55.36	15.53	14.36	93.81
37 - RPGX 3V	406	55.73	15.09	14.31	93.72
40 - RPGX 3V	278	53.99	15.89	14.49	93.12
41 - RPGX 3V	205	52.63	16.16	14.91	91.17
42 - RPGX 3V	275	53.86	15.88	14.27	92:65
9 - SNMN	265	59.45	15.62	13.52	91.60
10 – SNMN	219	58.46	15.94	13.95	91.00
12 – SNMN	267	59.51	15.86	13.59	92.56
14 – SNMN	285	60.11	15.57	14.14	93.05
19 – SNMN	199	57.86	16.58	14.65	92.49
25 – SNMN	166	56.78	16.91	15.06	92.28
30 – SNMN	224	58.67	15.88	13.71	91.48

Compared with Table 3.10, Table 3.11 shows that excessive use of carbon sheets negatively affects the samples' relative density. While the relative density reached 99% in Table 3.10, it was limited to a maximum of 94.05% in Table 3.11 due to the presence of carbon sheets. This difference indicates that carbon sheets disrupt the sample's internal structure during sintering and negatively impact the microstructure and mechanical properties. Therefore, the use of carbon sheets should be carefully optimized, or alternative methods should be considered.

Table 3.12 shows the relative density values obtained after resintering samples that did not reach the desired density in previous studies. As seen in the table, resintering significantly improved in relative density. For example, the values of some samples

increased to the 95–98% range, indicating clear progress compared to earlier sintering attempts. The most important outcome of this study was that low-density samples can approach the targeted density through resintering. However, some samples remained around 92%, showing that the desired level was not fully achieved. This suggests that resintering parameters—such as temperature, pressure and time—should be further optimized and the influence of carbon sheets should be minimized. The study demonstrates that resintering can improve underperforming samples and help reduce material waste.

Table 3.12. *Relative densities of resintered samples*

Sample Name	Relative Density (%)		
	1. GPS Run	2. GPS Run	3. GPS Run
9 - SNMN	91.60	95.63	98.90
10 - SNMN	91.00	95.52	98.90
12 – SNMN	92.56	96.31	98.63
30 – SNMN	91.48	95.08	-
31 – SNMN	91.46	95.12	-
32 – SNMN	91.55	95.06	-
35 – RPGX 3V	94.05	99.00	-
36 – RPGX 3V	93.81	98.88	-
38 – RPGX 3V	93.94	98.01	-

Fig. 3.40 illustrates the placement of the samples and carbon sheet inside the graphite crucible during the experiments. The first configuration, shown in Fig. 3.40.a, represents the setup used in an individual sintering experiment, where carbon sheets were placed below and above the samples. Since using carbon paper was limited in this study, the density results were positive and the samples reached nearly full density (~ 99%).

Fig. 3.40.b shows the configuration used for mass production, where multiple samples were placed in the same sintering system following the positive results from earlier experiments. In this setup, the excessive use of carbon sheets had a negative impact on the material structure during sintering. The increased amount of carbon sheet reduced the relative density of the samples and negatively affected their overall density.

Fig. 3.40.c illustrates a configuration where previously low-density samples were used as dummy samples and the carbon sheet was completely removed. The absence of the carbon sheet contributed to an improvement in the density of the new samples. The

dummy samples helped balance the system, enhancing thermal conductivity and supporting increased density during the sintering process.

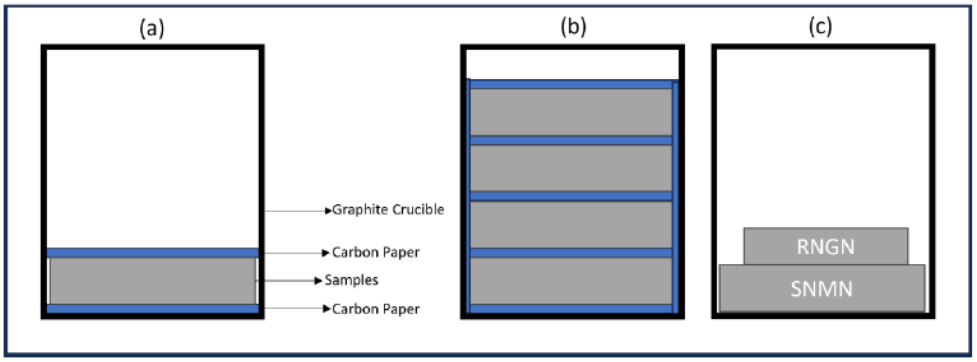

Figure 3.40. *Representative sintering configurations used in this study*

These three configurations clearly demonstrate the critical importance of the amount and placement of carbon sheets in the sintering process. While carbon sheets do not negatively affect density when used in controlled amounts, excessive use leads to decreased density. Alternatively, sintering setups without carbon sheets have shown more positive results and have the potential to improve material properties. These findings highlight the importance of optimizing carbon sheet usage to make sintering processes more efficient.

Table 3.13 shows the relative density, hardness and fracture toughness of the resintered samples. Fracture toughness measurements could not be performed for Samples 8 and 34, as their relative densities were 90% and 93%, respectively. A clear increase in hardness was observed as density increased. For example, Sample 13, with a relative density of 96%, showed a hardness of 16.74 GPa and a fracture toughness of 4.85 $MPa \cdot m^{1/2}$. Sample 26, with 99% relative density, achieved the highest values 20.18 GPa for hardness and 4.97 $MPa \cdot m^{1/2}$ for fracture toughness. These results clearly demonstrate that increased density after resintering has a direct and positive effect on mechanical properties. In particular, Sample 26 showed superior performance in both hardness and fracture toughness due to reaching 99% density.

Table 3.13. *Mechanical properties of resintered samples*

Sample Name	Relative Density (%)	Hardness (GPa)	Fracture Toughness (MPa $m^{1/2}$)
8	90	9.86	-
34	93	11.47	-
13	96	16.74	4.85
26	99	20.18	4.97

Fig. 3.41 presents backscattered SEM images of the resintered samples at 2500× magnification. Fig. 3.41.a shows Sample 8 with 90% density, fig. 3.41.b shows Sample 34 with 93% density, fig. 3.41.c shows Sample 13 with 96% density and fig. 3.41.d shows Sample 26 with 99% density. These images clearly demonstrate the resintering process's effect on density and microstructure.

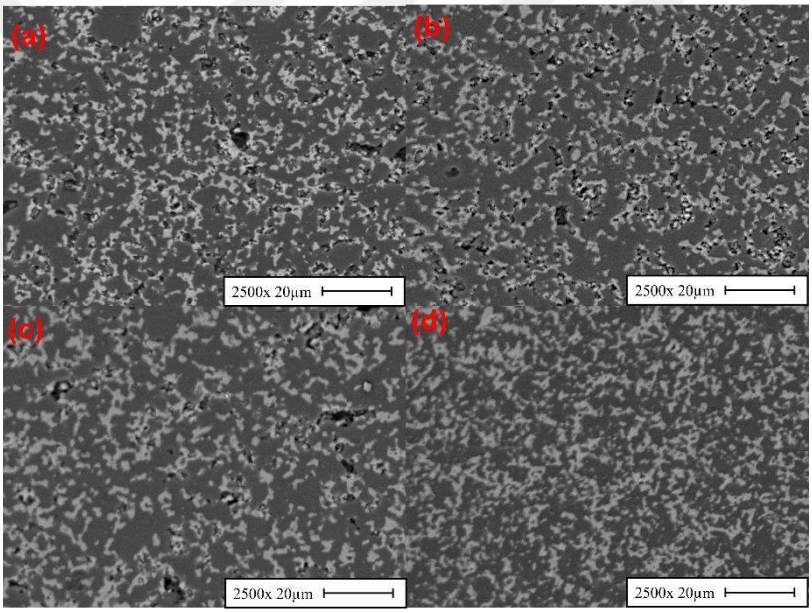

Figure 3.41. *Representative backscattered SEM images taken from polished surface of resintered samples. (a) sample 8, (b) sample 34, (c) sample 13 and (d) sample 26*

As expected, increasing the density led to a significant decrease in pores within the microstructure. More pores were observed in Samples 8 and 34 (with 90% and 93% relative density, respectively). The bonding between particles was incomplete and the structure appears more porous. This explains the weaker mechanical properties and why fracture toughness could not be measured for these samples. In Sample 13, porosity was reduced and particles were more tightly packed. Finally, Sample 26 shows the most homogeneous structure with the least amount of pores. This demonstrates the

effectiveness of the resintering process and that the material has reached an optimal level in terms of mechanical properties.

Table 3.14 presents the density and geometric properties of samples pressed within a very narrow pressure range, between 373 and 381 MPa. It was observed that the relative densities of the samples produced under these conditions were all above 99%. This indicates that the selected pressure range was optimal for sintering and has yielded successful results.

Table 3.14. *ATZ composition pressed in a narrow range of pressing pressure and sintered with a graphite crucible*

		Before GPS	After GPS		
Sample Name	**Applied Pressure (MPa)**	**Green Body Density (%)**	**Diameter (%)**	**Height (%)**	**Relative Density (%)**
12	379	54.87	16.71	15.79	99.84
16	373	54.95	15.99	16.32	99.72
20	375	55.13	16.07	16.32	99.82
25	381	55.08	16.63	15.70	99.86
35	367	54.80	16.56	16.40	99.75

When the data in Table 3.14 was examined, it was observed that the green density ranges between 54.80% and 55.13% and the diameter and length shrinkage rates were quite consistent. The similarity in density values indicates that the selected pressing pressure provides consistent and repeatable results. This also shows that the process parameters have been successfully optimized.

Fig. 3.42 presents backscattered SEM images of Sample 35 at different magnifications. This sample represents the Al_2O_3–TiC–ZrO_2 (ATZ) composition produced under optimal pressing and sintering conditions. In fig. 3.42.a, the overall structure of the sample can be seen; the particles were uniformly distributed and no visible pores were present. In fig. 3.42.b, the phase distribution becomes clearer, showing that TiC particles were homogeneously embedded in the Al_2O_3 matrix. Fig. 3.42.c reveals that the particle interfaces were rounded and the microstructure was tightly sintered. In fig. 3.42.d, grain boundaries were more distinct and the TiC, ZrO_2 and Al_2O_3 phases were clearly visible, along with localized densification. These results demonstrate that when proper pressing and sintering parameters were applied, the ATZ composition achieves excellent density and microstructural quality.

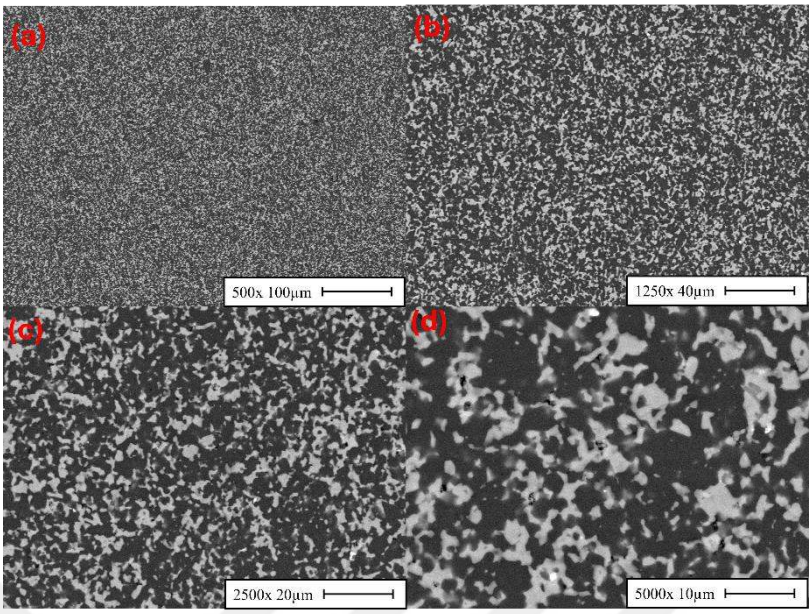

Figure 3.42. *Representative backscattered SEM images taken from polished surface of Sample 35*

Fig. 3.43 shows the EDS analysis of Sample 35 in backscattered SEM mode at 1250× magnification. According to the results, oxygen (O) and aluminum (Al) were the main components, with weight percentages of 44.81% and 28.14%, respectively. This confirms that the sample was based on an Al_2O_3 matrix. Titanium (Ti) was measured at 18.19%, supporting the presence of TiC. Carbon (C) was detected at 6.95%, while zirconium (Zr) was found at a relatively low 1.90%, indicating that ZrO_2 was added in a small amount (3.5 wt.%) as an additive. Despite the low amount, ZrO_2 contributed effectively to the overall structure. In conclusion, the EDS analysis confirms that the chemical composition of Sample 35 matches the expected ATZ (Al_2O_3–TiC–ZrO_2) composition and that the sintering process was completed.

Element	Weight%	Atomic%
C	6,95	12,00
O	44,81	58,07
Al	28,14	21,62
Ti	18,19	7,87
Zr	1,90	0,43

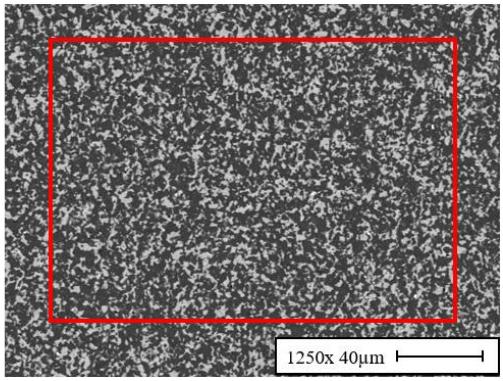

Figure 3.43. *Representative backscattered SEM image and EDS analysis taken from the polished surface of sample 35*

Fig. 3.44 shows the crack propagation mechanism in Sample 35. Transgranular and intergranular crack propagation were observed in the backscattered SEM images taken at 5000× magnification. Transgranular crack propagation means that the crack moves directly through the grains, indicating a brittle structure with high hardness. Intergranular crack propagation, on the other hand, shows that the crack follows the grain boundaries.

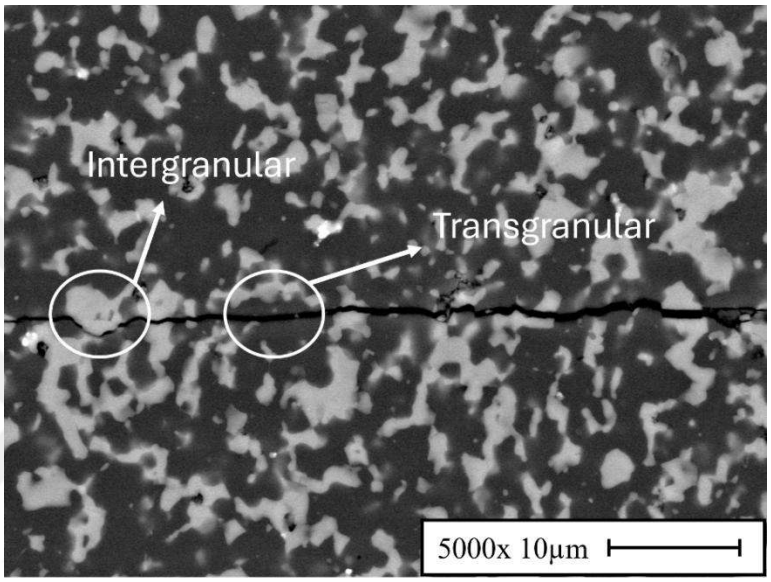

Figure 3.44. *Representative backscattered SEM images taken from polished surface of crack propagation of sample 35*

When the sample's mechanical properties were examined, the hardness was measured as 20.90 GPa. This high value confirms that the sample has a compact and dense structure. However, the fracture toughness was determined as 4.49 $MPa \cdot m^{1/2}$, indicating that the material offers some resistance to crack propagation but does not behave fully ductile. Although the hardness was high, the relatively limited fracture toughness suggests that transgranular crack propagation was dominant and the brittle nature of the ceramic was maintained.

In conclusion, fig. 3.44 and the mechanical test results show that Sample 35 has good toughness and offers a certain level of resistance to fracture. However, intergranular and transgranular crack propagations occur together, indicating a mixed fracture mechanism.

3.6. Effect of Rare Earth Oxide Additives

In this study, after optimizing the pressing and sintering parameters of the ATZ composition, an additive study using rare earth oxides (REOs) (Er_2O_3, Yb_2O_3, Y_2O_3, Sm_2O_3 and CeO_2) was conducted to improve the sintering behavior and mechanical properties of the material. These oxides were added at 3.5% and 5% by weight and their effects on the mechanical and microstructural properties of the ATZ composition were investigated.

There were no studies in the literature specifically focused on the ATZ composition with REOs. Existing research on Al_2O_3–TiC systems has generally examined only a limited number of oxides, without providing detailed comparisons. In this study, the effects of REO additives on the ATZ composition were evaluated by using previous research on Al_2O_3-based systems as a reference. The main reason for selecting these oxides was that Y_2O_3 lies in the middle of the ionic radius range among the chosen REOs. Since there was an existing study on Al_2O_3–TiC–Y_2O_3, it was taken as a reference point and comparing it with other REOs helped to broaden the scope of this research.

Adding these additives to the ATZ composition aimed to improve sintering kinetics, control grain growth and enhance mechanical properties. In particular, the effects of second phases that may form during sintering on the material's density and fracture toughness were examined in detail. Efforts were made to determine the optimum type and amount of additive. In this context, mechanical and microstructural properties were evaluated comparatively and the impact of modifying the ATZ composition with REOs on overall performance was clearly revealed.

3.6.1. Er_2O_3 additives

Samples were produced using different sintering methods by adding 3.5 wt.% and 5 wt.% REOs to the ATZ composition and the effects of these methods on material properties were compared. Sintering was performed using SPS, GPS with a carbon sheet and GPS without a carbon sheet. The densities of the resulting samples were analyzed in detail, their mechanical properties were evaluated and microstructural studies were conducted.

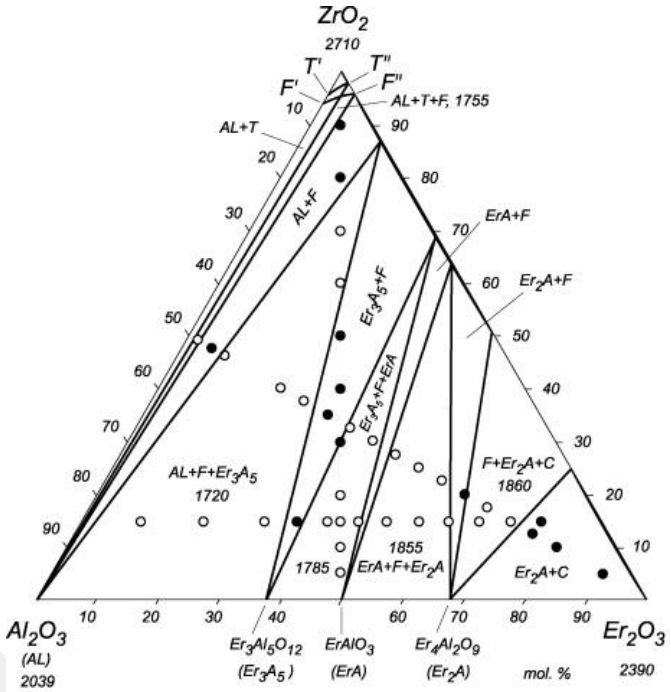

Figure 3.45. *Representative ternary phase diagram of Al_2O_3-Er_2O_3-ZrO_2 (Lakiza and Lopato, 2008)*

The effect of Er_2O_3 on sintering behavior and phase formation was investigated by adding it to the ATZ composition. According to Özerdem et al. (Özerdem and Ayas, 2015), the $Er_3Al_5O_{12}$ phase (Erbium Aluminum Garnet – EAG) forms when Er_2O_3 was added to an Al_2O_3 matrix. This phase can precipitate during sintering, helping to control grain growth and influencing mechanical properties. This study examined the formation of this phase and its effects on the material structure. The optimum additive ratio and sintering conditions were determined by adding Er_2O_3 to the ATZ composition.

The SPS method was used to investigate the sintering behavior of the ATZ–3.5Er composition. SPS was useful for understanding sintering behavior because it enables densification at high temperatures in a short time. The shrinkage behavior of the sample was monitored using the displacement curve and the critical temperatures for the sintering process were identified during the SPS procedure.

According to Fig. 3.46, the temperature at which the displacement curve begins to rise (T_{shr}) was determined as 1320 °C for the ATZ–3.5Er composition. This temperature marks the point where the sample's pores begin to close and densification starts. The temperature at which the displacement curve levels off (T_{sin}) was measured as 1610 °C, indicating the stage where the sample approaches full density and the sintering process

was nearly complete. The same predetermined parameters were used in the GPS sintering studies, which were carried out with and without using a carbon sheet.

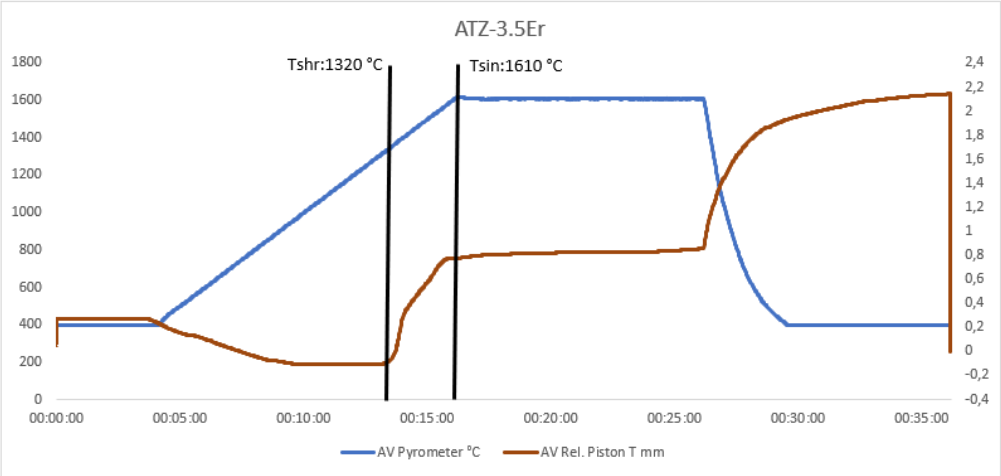

Figure 3.46. *Representative SPS graphic of ATZ-3.5Er composition*

Table 3.15 shows the relative density (%) values of ATZ–3.5Er samples produced using three different sintering methods. The sample sintered by the SPS method achieved the highest relative density at 99.95%. This indicates that SPS minimizes porosity by quickly and effectively sintering the material using high temperature and electrical current. The sample sintered using the GPS method with a carbon sheet had a relative density of 95.64%. This result shows that the carbon sheet negatively affected the sintering process. The presence of the carbon sheet limited oxygen and increased porosity, preventing full densification.

On the other hand, the GPS sample without a carbon sheet reached a relative density of 97.69%, showing better performance than the one with the carbon sheet. The sintering atmosphere was more stable and the material densified more evenly. However, since GPS uses lower pressure and requires longer processing time than SPS, it cannot achieve as high a density as SPS.

Table 3.15. *Sintering methods and relative densities of ATZ-3.5Er composition*

Sintering Method	Relative Density (%)
SPS	99.95
GPS – Carbon Sheet	95.64
GPS	97.69

Fig. 3.47 compares the backscattered SEM images of the ATZ-3.5Er composition obtained using different sintering methods at 5000x magnification. Fig. 3.47.a shows the image of the sample sintered by the SPS method, which has the lowest porosity. The additive could not be well distributed in the structure and formed clusters due to the fast process of SPS. Fig. 3.47.b shows the sample sintered by the GPS method with a carbon sheet, which has high porosity and visible phase separation. Pores appeared at the grain boundaries and a homogeneous structure could not be achieved because the carbon sheet limited full densification. Fig. 3.47.c shows the sample sintered by the GPS method without a carbon sheet, which has a better microstructure than the one in fig. 3.47.b. Less porosity formed at the grain boundaries, but some irregularities in the phase distribution were still observed.

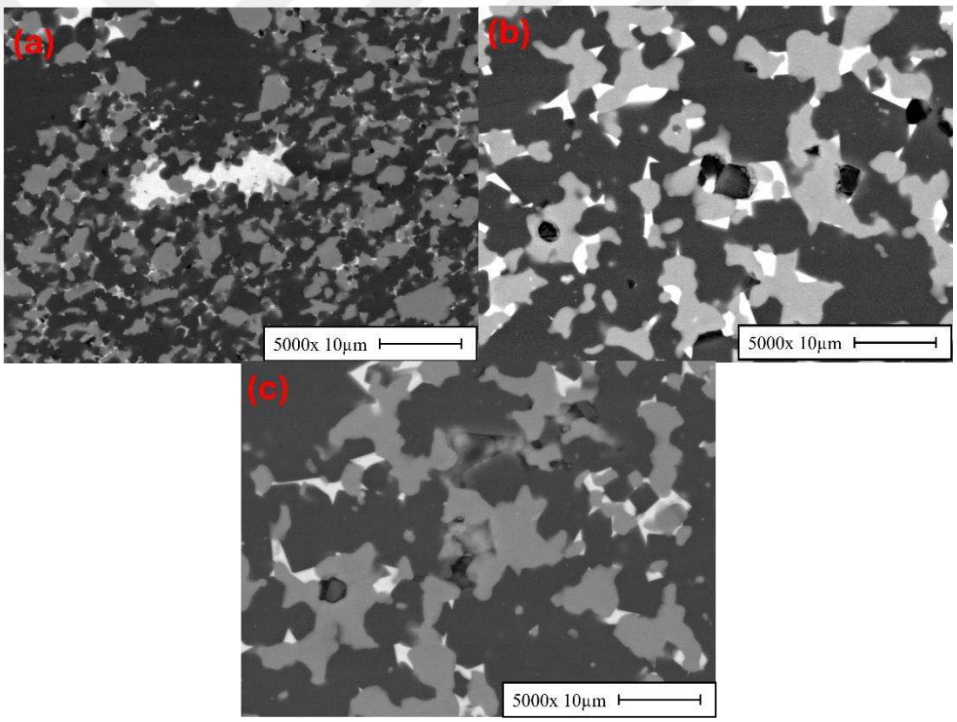

Figure 3.47. *Representative backscattered SEM images taken from polished surface of ATZ-3.5Er sintered using different methods. (a) SPS, (b) GPS with carbon sheet and (c) GPS without carbon sheet*

Fig. 3.48 shows the XRD analysis that compares the composition of ATZ-3.5Er with the original ATZ composition. The ATZ composition (orange curve) mainly contains Al_2O_3, TiC and ZrO_2 phases. In addition, some peaks related to carbon (C) phases were also seen. These carbon peaks were likely caused by the carbon sheet or the TiC used during the sintering process.

The ATZ-3.5Er composition (gray curve) shows how adding Er_2O_3 changes the material's structure. The XRD analysis reveals that Er_2O_3 doping reacts with Al_2O_3, forming the $Er_3Al_5O_{12}$ phase. This phase could help stabilize the microstructure and improve mechanical properties by adding a new oxide to the ATZ composition. The new peak corresponding to the $Er_3Al_5O_{12}$ phase was clearly visible in the ATZ-3.5Er composition. Additionally, the main phases (Al_2O_3, TiC and ZrO_2) in the ATZ composition remained unchanged, indicating that the overall structure of the material did not change significantly. However, the additive modified the matrix by creating a new phase.

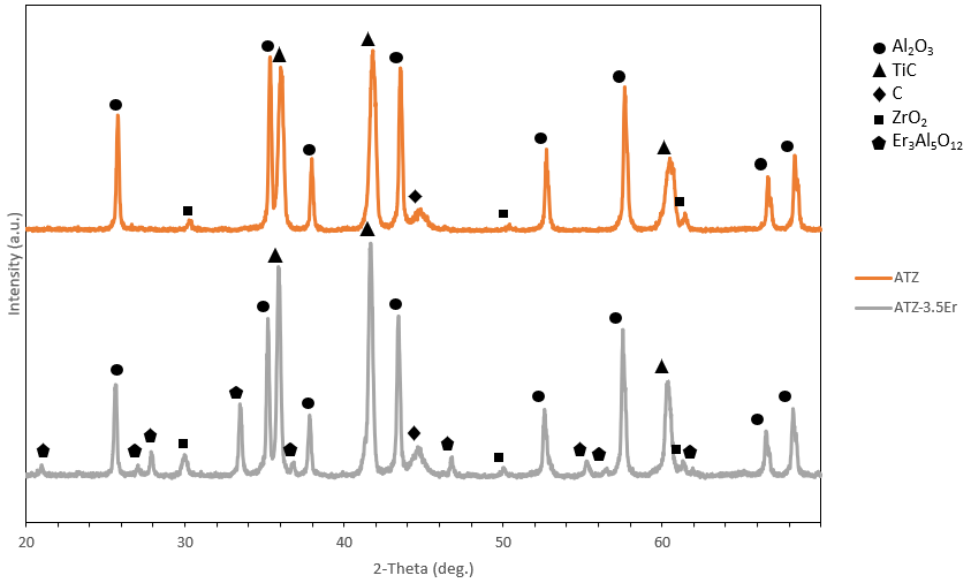

Figure 3.48. *Representative comparison of the XRD spectra of ATZ and ATZ-3.5Er*

Fig. 3.49 shows the EDS analysis of the ATZ-3.5Er composition in backscattered mode at 1250x magnification. According to the analysis, the main components of the composition were Al_2O_3, TiC and ZrO_2, with oxygen (O) being the highest at 43.62 wt.%. This confirms that the ATZ matrix was primarily based on Al_2O_3. Aluminum (Al) was detected at 27.39 wt.% and titanium (Ti) was detected at 18.25 wt.%, which supports the presence of Al_2O_3 and TiC phases in the ATZ structure. Zirconium (Zr) was detected at 1.83 wt.%, indicating the presence of ZrO_2 added to the ATZ composition.

Erbium (Er) element was detected with 2.63 wt.% in this analysis. This ratio shows that the Er_2O_3 contribution in the material after the sintering process was successfully incorporated into the composition and supported the formation of the $Er_3Al_5O_{12}$ phase

observed in the XRD analysis. The carbon (C) content was determined to be 6.29 wt. % due to the TiC content and possible carbon residues used in the sintering process.

Element	Weight%	Atomic%
C	6,29	11,18
O	43,62	58,24
Al	27,39	21,68
Ti	18,25	8,14
Zr	1,83	0,43
Er	2,63	0,34

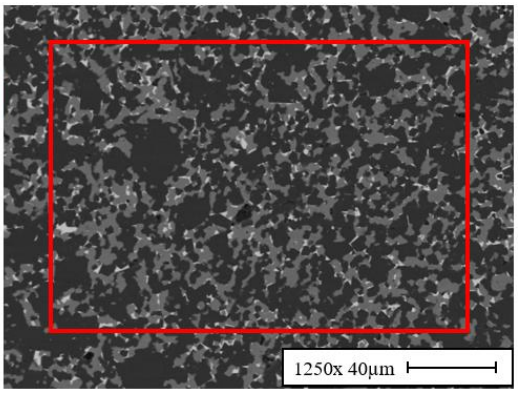

Figure 3.49. *Representative backscattered SEM image and EDS analysis taken from the polished surface of ATZ-3.5Er*

Table 3.16 compares the mechanical properties (hardness and fracture toughness) of samples of ATZ-3.5Er composition produced with different sintering methods. Mechanical tests were not performed since the relative density of the sample sintered with a carbon sheet GPS was low.

Table 3.16. *Mechanical properties of ATZ-3.5Er compositions*

Sintering Method	Hardness (GPa)	Fracture Toughness (MPa $m^{1/2}$)
SPS	17.32	4.46
GPS	20.62	6.29

The hardness of the sample sintered with SPS was measured as 17.32 GPa. However, the fracture toughness of the sample sintered with SPS was measured as 3.46 MPa $m^{1/2}$, lower than that of the sample sintered with the GPS method. The sample sintered with the GPS method reached 20.62 GPa hardness and 6.29 MPa $m^{1/2}$ fracture toughness values. The higher hardness of the sample sintered with GPS can be explained by the longer sintering process and more stable phase formations. The higher fracture toughness indicates that better grain bonding may have been achieved during the GPS sintering. The $Er_3Al_5O_{12}$ phase formed by Er_2O_3 doping may have contributed to improving these mechanical properties.

Fig. 3.50 shows the backscattered SEM images comparing the crack propagation mechanism in SPS and GPS sintered samples of ATZ-3.5Er composition. Fig. 3.50.a

represents the sample sintered with the SPS method and fig. 3.50.b represents the sample sintered with the GPS method. Transgranular and intergranular crack propagation mechanisms were observed in both samples. However, it was determined that the crack bridging mechanism occurred in the sample using the SPS method.

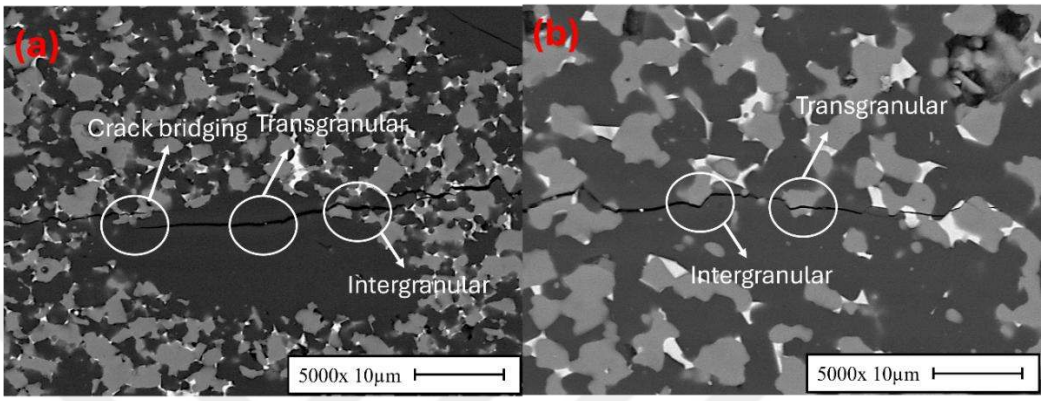

Figure 3.50. *Representative backscattered SEM images taken from polished surface of crack propagation of ATZ-3.5Er sample, (a) SPS sintered sample, (b) GPS sintered sample*

According to fig. 3.51, the temperature at which the displacement curve starts to increase (Tshr) was determined as 1330 °C for ATZ-5Er. This temperature represents the threshold at which the sample's pores begin to close and the material enters the densification process. The temperature at which the displacement curve remains constant (Tsin) was measured as 1630 °C. This temperature represents the point at which the sample reaches the closest level to full density and the material completes the sintering process.

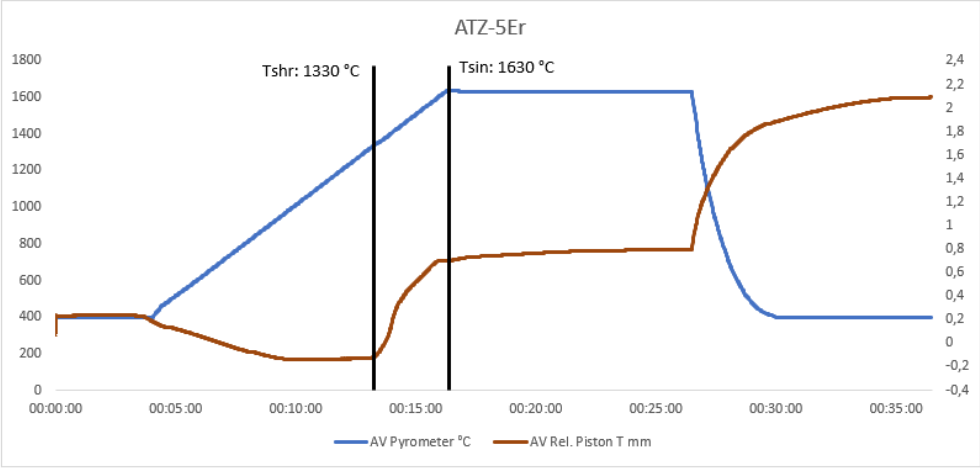

Figure 3.51. *Representative SPS graphic of ATZ-5Er composition*

Table 3.17 shows the relative density (%) values of samples of ATZ-5Er composition produced by three different sintering methods. The sample sintered with the SPS method achieved the highest density by reaching 99.97% relative density. The relative density of the sample sintered with the GPS – carbon sheet was 94.06%. The sample sintered with the GPS method without a carbon sheet reached a relative density of 96.95% and a more successful sintering process compared to the GPS method with a carbon sheet.

Table 3.17. *Sintering methods and relative densities of ATZ-5Er composition*

Sintering Method	Relative Density (%)
SPS	99.97
GPS – Carbon Sheet	94.06
GPS	96.95

Fig. 3.52 compares the backscattered SEM images of ATZ-5Er composition obtained with different sintering methods at 5000x magnification. Fig. 3.52.a shows the image of the SPS sintered sample with the lowest porosity. The additive could not be sufficiently distributed within the structure and formed clusters due to the speed of the SPS method. Fig. 3.52.b shows the image of the sample sintered with the GPS with a carbon sheet showing phase separation. Fig. 3.52.c shows the image of the sample sintered with the GPS method without a carbon sheet.

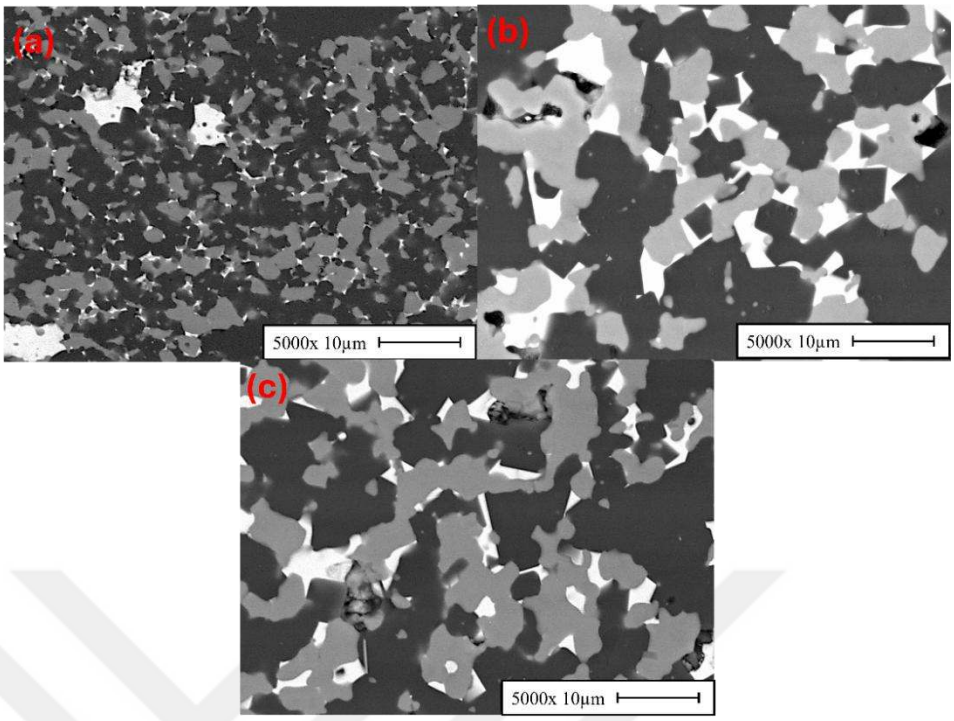

Figure 3.52. *Representative backscattered SEM images taken from polished surface of ATZ-5Er sintered using different methods. (a) SPS, (b) GPS with carbon sheet and (c) GPS without carbon sheet*

Fig. 3.53 shows the EDS analysis of the ATZ-5Er composition in backscattered mode at 1250x magnification. According to the results of the analysis, the composition's main components were Al_2O_3, TiC and ZrO_2 with oxygen (O), which was the highest with a 42.53 wt.%. This confirms that the ATZ matrix was largely Al_2O_3-based. Aluminum (Al) was detected with 26.19 wt.% and titanium (Ti) was detected with 18.72 wt.%. It supports the existence of Al_2O_3 and TiC phases in the ATZ structure. Zirconium (Zr) was detected with 2.08 wt. % indicating the presence of ZrO_2 added to the ATZ composition.

This analysis detected erbium (Er) element with 2.89 wt.% in this analysis. This ratio shows that the Er_2O_3 contribution in the material after the sintering process was successfully incorporated into the composition and supported the formation of the $Er_3Al_5O_{12}$ phase observed in the XRD analysis. The carbon (C) content was determined 7.59 wt.% due to the TiC content and possible carbon residues used in the sintering process.

Element	Weight%	Atomic%
C	7,59	13,47
O	42,53	56,66
Al	26,19	20,69
Ti	18,72	8,33
Zr	2,08	0,49
Er	2,89	0,37

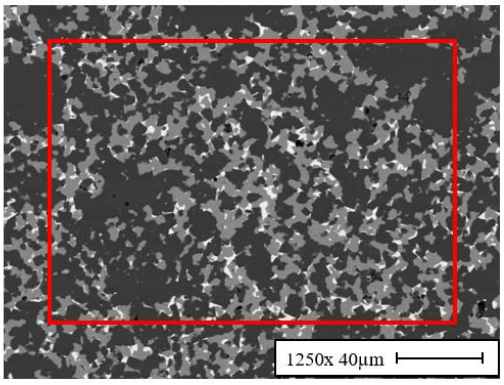

Figure 3.53. *Representative backscattered SEM image and EDS analysis taken from the polished surface of ATZ-5Er*

Table 3.18 compares the mechanical properties (hardness and fracture toughness) of samples of ATZ-5Er composition produced with different sintering methods. Mechanical tests were not performed since the relative density of the sample sintered with the carbon sheet GPS was low.

Table 3.18. *Mechanical properties of ATZ-5Er compositions*

Sintering Method	Hardness (GPa)	Fracture Toughness (MPa $m^{1/2}$)
SPS	17.11	4.61
GPS	20.95	5.41

The hardness of the sample sintered with SPS was measured as 17.11 GPa. However, the fracture toughness of the sample sintered with SPS was measured as 4.61 MPa $m^{1/2}$, lower than that of the sample sintered with the GPS method. The sample sintered with the GPS method reached 20.95 GPa hardness and 5.41 MPa $m^{1/2}$ fracture toughness values. The higher hardness of the sample sintered with GPS can be explained by the longer sintering process and more stable phase formations. The higher fracture toughness indicates that better grain bonding may have been achieved during the GPS sintering. The $Er_3Al_5O_{12}$ phase formed by Er_2O_3 doping may have contributed to improving these mechanical properties.

Fig. 3.54 shows the backscattered SEM images comparing the crack propagation mechanism in SPS and GPS sintered samples of ATZ-5Er composition. Fig. 3.54.a represents the sample sintered with the SPS method and fig. 3.54.b represents the sample sintered with the GPS method. Transgranular and intergranular crack propagation

mechanisms were observed in both samples. However, it was determined that the crack bridging mechanism occurred in the sample using the GPS method.

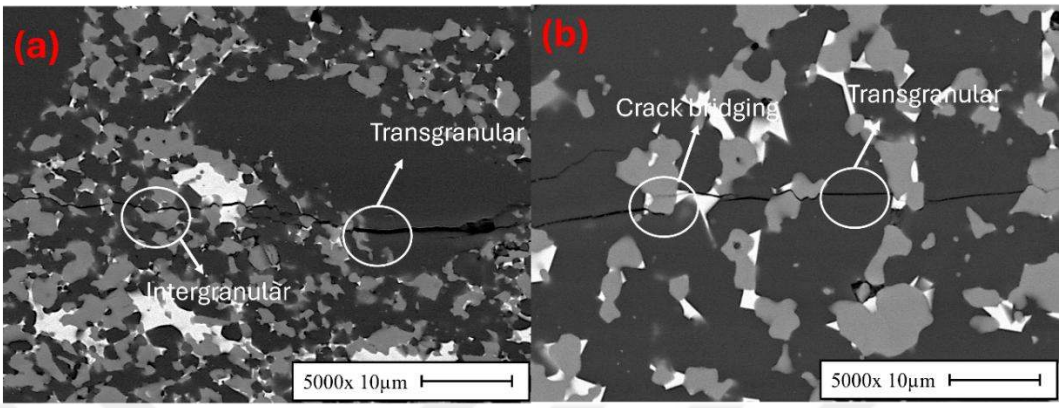

Figure 3.54. *Representative backscattered SEM images taken from polished surface of crack propagation of ATZ-5Er sample*

In fig. 3.55, the darkest areas were Al_2O_3, medium bright areas were TiC and the brightest grains were $Er_3Al_5O_{12}$. The detection of $Er_3Al_5O_{12}$ in XRD analysis indicates that Er_2O_3 reacts with Al_2O_3 and forms garnet type $Er_3Al_5O_{12}$.

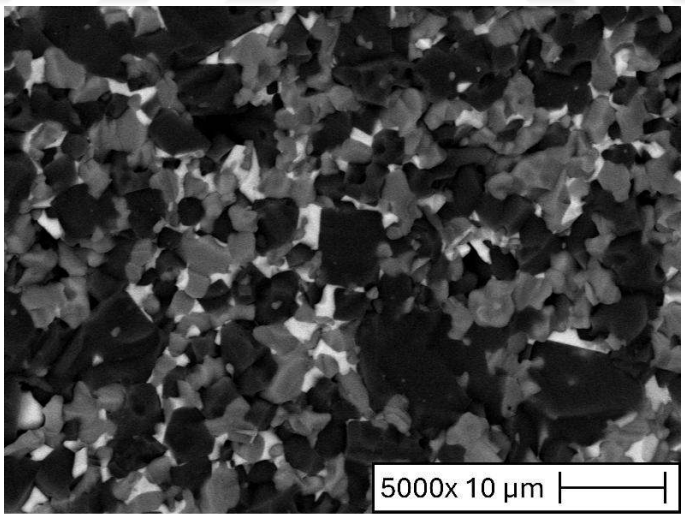

Figure 3.55. *Representative backscattered SEM image taken from the fractured surface of ATZ-3.5Er*

3.6.2. Yb_2O_3 additives

Samples were produced using different sintering methods such as adding 3.5 wt.% and 5 wt.% Yb_2O_3 to the ATZ composition and the effects of these methods on the material properties were compared. Sintering processes were carried out using three

different methods: SPS, GPS with a carbon sheet and GPS without a carbon sheet. The densities of the obtained samples were analyzed in detail, their mechanical properties were evaluated and microstructural studies were carried out.

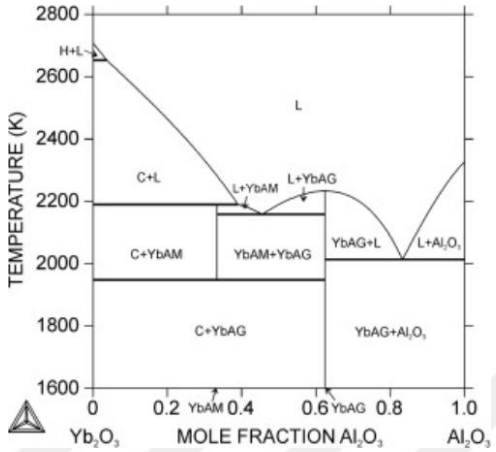

Figure 3.56. *Representative phase diagram of Al_2O_3-Yb_2O_3. (Fabrichnaya and Seifert, 2010)*

The effects of sintering methods on the material properties were investigated by adding 3.5 wt.% and 5 wt.% Yb_2O_3 to the ATZ composition. Sintering process was carried out using SPS, GPS with carbon sheet and GPS methods and the obtained sample's densities, mechanical properties and microstructures were compared. Studies by Sun et al. (Sun, et al., 2021) reported that the $Yb_3Al_5O_{12}$ (Ytterbium Aluminum Garnet – YbAG) phase was formed when Yb_2O_3 was added to the Al_2O_3 matrix. It has been stated that this phase has a limiting effect on grain growth during sintering and can increase the material's fracture toughness. In this study, the addition of Yb_2O_3 causes a phase transformation in the ATZ composition.

The SPS method was used to understand the sintering behavior of ATZ-3.5Yb composition. SPS provides important information about the sintering behavior of the material, as it provides densification at high temperature and in a short time. The shrinkage behavior of the sample was followed by the displacement curve and the critical temperatures for the sintering process were determined during the SPS sintering process.

According to fig. 3.57, the temperature at which the displacement curve starts to increase (Tshr) was determined as 1350 °C for ATZ-3.5Yb. This temperature represents the threshold at which the pores of the sample begin to close and the material enters the densification process. The temperature at which the displacement curve remains constant (Tsin) was measured as 1650 °C. This temperature represents the point at which the

sample reaches the closest level to full density and the material completes the sintering process. Predetermined parameters were used for the GPS sintering study. Sintering was performed with the same parameters with and without a carbon sheet.

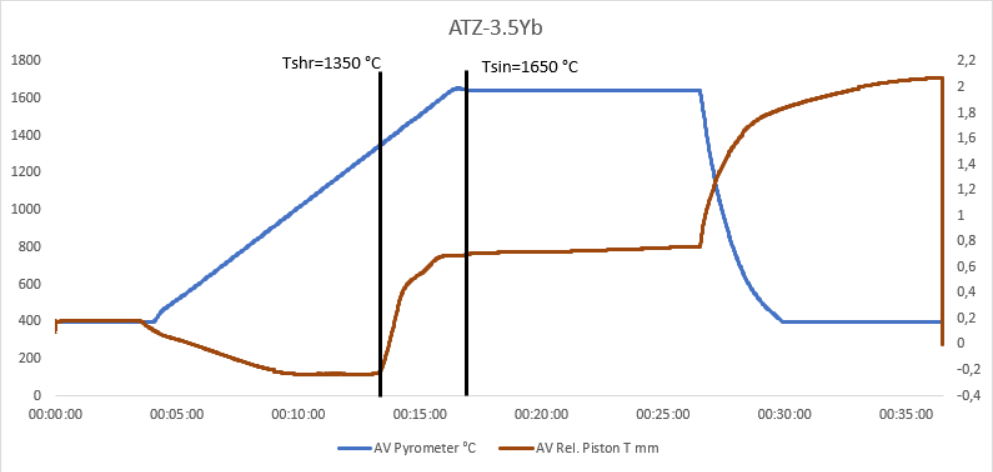

Figure 3.57. *Representative SPS graphic of ATZ-3.5Yb composition*

Table 3.19 shows the relative density (%) values of samples of ATZ-3.5Yb composition produced by three different sintering methods. The sample sintered with the SPS method achieved the highest density by reaching 99.99% of the relative density. This shows that SPS minimizes porosity by sintering the material quickly and effectively under the influence of high temperature and electrical current. The relative density of the sample sintered with the GPS – carbon sheet was 95.91%. This shows that carbon sheets have a negative effect on the sintering process. The carbon sheet prevented full densification during sintering due to oxygen limitation and increased the porosity level of the sample. The sample sintered with the GPS method without a carbon sheet reached a relative density of 98,32% and a more successful sintering process than the GPS method with a carbon sheet. The sintering atmosphere was more stable and the material was densified more homogeneously when a carbon sheet was not used. However, since the GPS method took longer and was under lower pressure than SPS, it could not achieve a density as high as SPS.

Table 3.19. *Sintering methods and relative densities of ATZ-3.5Yb composition*

Sintering Method	Relative Density (%)
SPS	99.99
GPS – Carbon Sheet	95.91
GPS	98.32

Fig. 3.58 compares the backscattered SEM images of ATZ-3.5Yb composition obtained with different sintering methods at 5000x magnification. Fig. 3.58.a shows the image of the SPS sintered sample with has the lowest porosity. The additive could not be sufficiently distributed within the structure and formed clusters due to the speed of the SPS method. Fig. 3.58.b shows the image of the sample sintered with the GPS with a carbon sheet, showing high porosity and phase separation. Pores formed at the grain boundaries and a homogeneous structure could not be obtained since the carbon sheet could not fully densify during the sintering. Fig. 3.58.c shows that the image of the sample sintered with the GPS method without carbon sheet has a better microstructure than fig. 3.58.b. Less porosity was formed at grain boundaries, but certain irregularities in the phase distribution were observed.

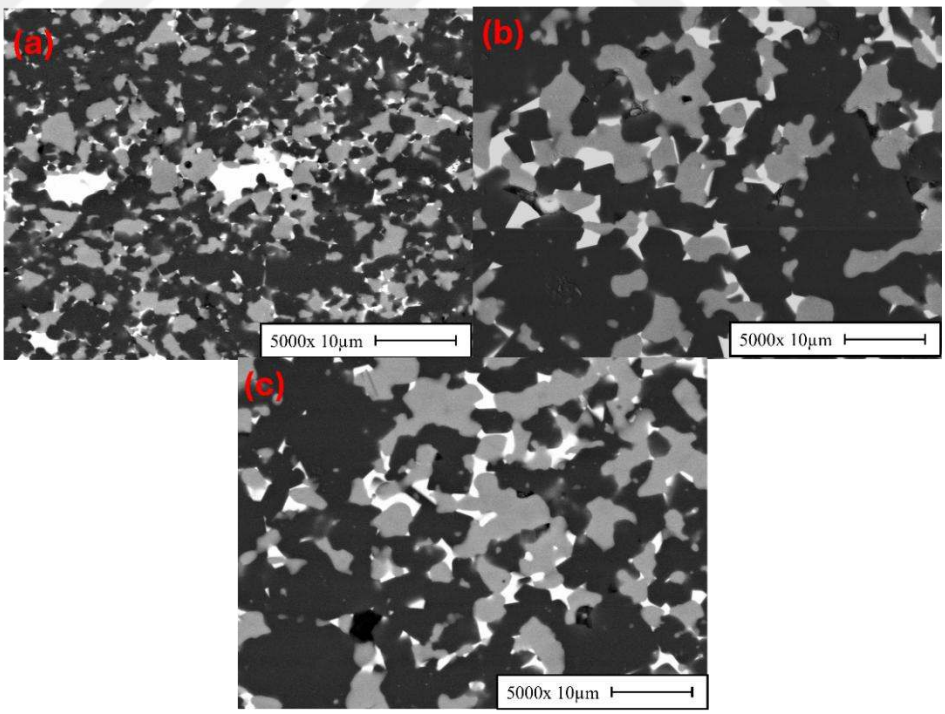

Figure 3.58. *Representative backscattered SEM images taken from polished surface of ATZ-3.5 Yb sintered using different methods. (a) SPS, (b) GPS with carbon sheet and (c) GPS without carbon sheet*

Fig. 3.59 shows the XRD analysis, comparing the composition of ATZ-3.5Yb with the composition of ATZ. The ATZ composition (orange curve) consists of the main phases Al2O3, TiC and ZrO2. some peaks belonging to the carbon (C) phases were also observed, which were related to the carbon sheet or TiC content used in the sintering process.

The ATZ-3.5Yb composition (gray curve) reveals how the Yb_2O_3 addition changes the material's structure. XRD shows that Yb_2O_3 doping reacts with Al_2O_3 forming the $Yb_3Al_5O_{12}$ phase. This phase may contribute to stabilizing the microstructure and potentially improving mechanical properties by providing a new oxide contribution to the ATZ composition. It was seen that the new peak belonging to the $Yb_3Al_5O_{12}$ phase appears clearly in the ATZ-3.5Yb composition. Besides, other main phases (Al_2O_3, TiC and ZrO_2) in the ATZ composition remained intact, indicating that the overall structure of the material did not change significantly. However, the additive modified the matrix by forming a new phase.

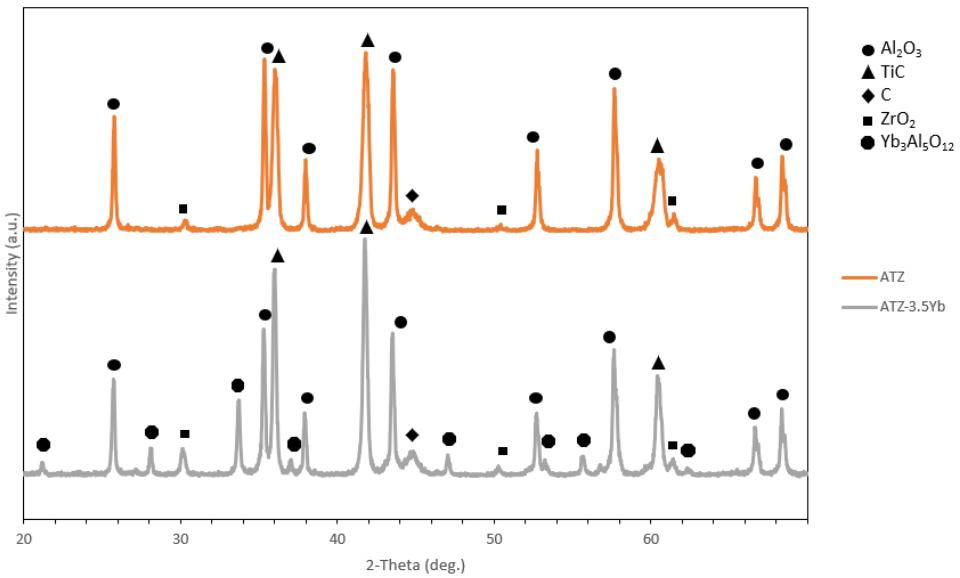

Figure 3.59. *Representative comparison of the XRD spectra of ATZ and ATZ-3.5Yb*

Fig. 3.60 shows the EDS analysis of the ATZ-3.5Yb composition in backscattered mode at 1250x magnification. According to the results of the analysis, the main components of the composition were Al_2O_3, TiC and ZrO_2 with oxygen (O), which was the highest with a 42.99 wt.%. This confirms that the ATZ matrix was largely Al_2O_3 based. Aluminum (Al) was detected with 24.43 wt.% and titanium (Ti) was detected with

19.20 wt.%. It supports the existence of Al_2O_3 and TiC phases in the ATZ structure. Zirconium (Zr) was detected with 2.45 wt.% indicating the presence of ZrO_2 added to the ATZ composition.

This analysis detected ytterbium (Yb) element with 3.19 wt.%. This ratio shows that the Yb_2O_3 contribution in the material after the sintering process was successfully incorporated into the composition and supported the formation of the $Yb_3Al_5O_{12}$ phase observed in the XRD analysis. The carbon (C) content was determined to be 7.74 wt.% due to the TiC content and possible carbon residues used in the sintering process.

Element	Weight%	Atomic%
C	7,74	13,76
O	42,99	57,38
Al	24,43	19,33
Ti	19,20	8,56
Zr	2,45	0,57
Yb	3,19	0,39

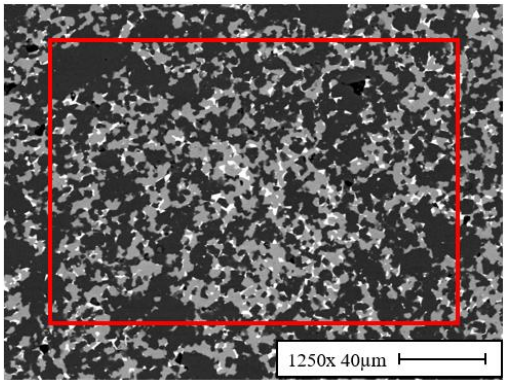

Figure 3.60. *Representative backscattered SEM image and EDS analysis taken from the polished surface of ATZ-3.5Yb*

Table 3.20 compares the mechanical properties (hardness and fracture toughness) of samples of ATZ-3.5Yb composition produced with different sintering methods. Mechanical tests were not performed since the relative density of the sample sintered with the carbon sheet GPS was low.

Table 3.20. *Mechanical properties of ATZ-3.5Yb compositions*

Sintering Method	Hardness (GPa)	Fracture Toughness (MPa $m^{1/2}$)
SPS	17.93	4.10
GPS	17.54	5.01

The hardness of the sample sintered with SPS was measured as 17.93 GPa. However, the fracture toughness of the sample sintered with SPS was measured as 4.10 MPa $m^{1/2}$, lower than that of the sample sintered with the GPS method. The sample sintered with the GPS method reached 17.54 GPa hardness and 5.01 MPa $m^{1/2}$ fracture toughness values. The higher hardness of the sample sintered with GPS can be explained by the longer sintering process and more stable phase formations. The higher fracture

toughness indicates that better grain bonding may have been achieved during the GPS sintering. The $Yb_3Al_5O_{12}$ phase formed by Yb_2O_3 doping may have improved these mechanical properties.

Fig. 3.61 shows the backscattered SEM images comparing the crack propagation mechanism in SPS and GPS sintered samples of ATZ-3.5Yb composition. Fig. 3.61.a represents the sample sintered with the SPS method and fig. 3.61.b represents the sample sintered with the GPS method. Transgranular and intergranular crack propagation mechanisms were observed in both samples. However, it was determined that the crack bridging mechanism occurred in the sample using the SPS method.

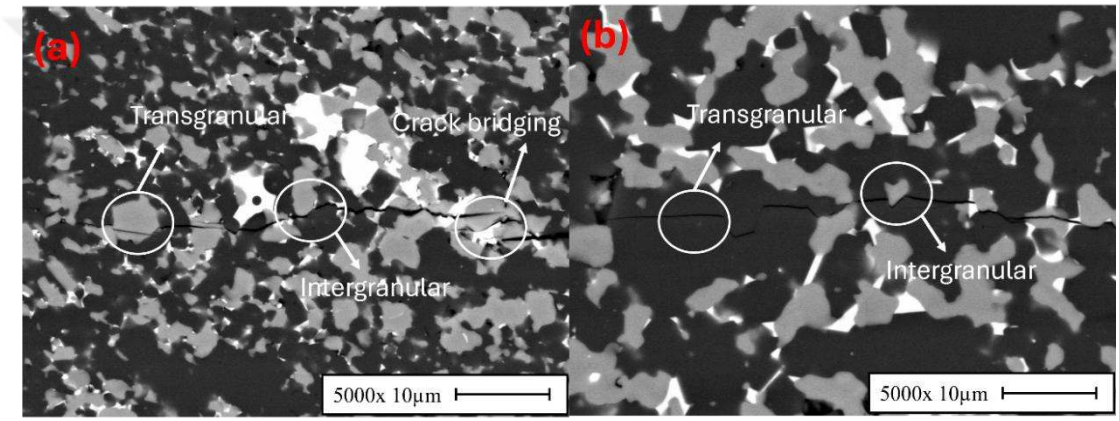

Figure 3.61. *Representative backscattered SEM images taken from polished surface of crack propagation of ATZ-3.5Yb sample, (a) SPS sintered sample, (b) GPS sintered sample*

According to fig. 3.62, the temperature at which the displacement curve starts to increase (Tshr) was determined as 1330 °C for ATZ-5Yb. This temperature represents the threshold at which the pores of the sample begin to close and the material enters the densification process. The temperature at which the displacement curve remains constant (Tsin) was measured as 1640 °C. This temperature represents the point at which the sample reaches the closest level to full density and the material completes the sintering process.

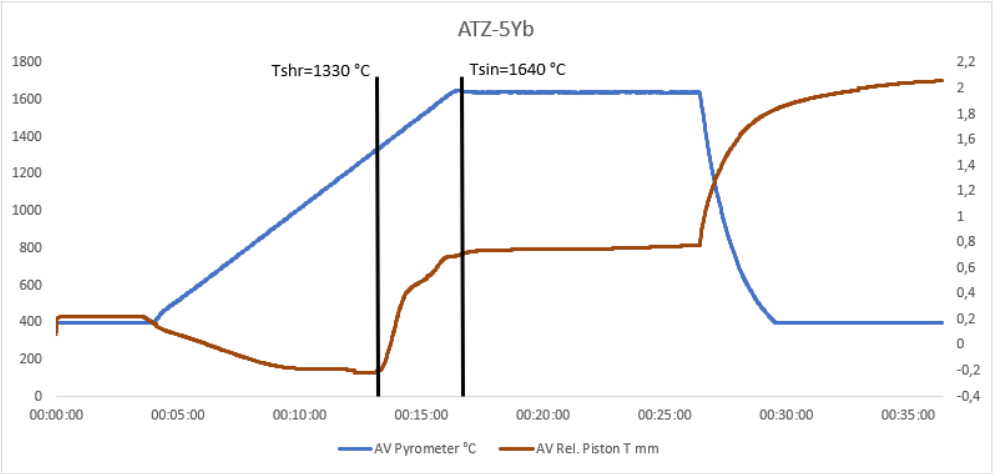

Figure 3.62. *Representative SPS graphic of ATZ-5Yb composition*

Table 3.21 shows the relative density (%) values of samples of ATZ-5Yb composition produced by three different sintering methods. The sample sintered with the SPS method achieved the highest density by reaching 99.99% of the relative density. The relative density of the sample sintered with the GPS – carbon sheet was 94.86%. The sample sintered with the GPS method without a carbon sheet reached a relative density of 97.90% and a more successful sintering process compared to the GPS method with a carbon sheet.

Table 3.21. *Sintering methods and relative densities of ATZ-5Yb composition*

Sintering Method	Relative Density (%)
SPS	99.99
GPS – Carbon Sheet	94.86
GPS	97.90

Fig. 3.63 compares the backscattered SEM images of ATZ-5Yb composition obtained with different sintering methods at 5000x magnification. Fig. 3.63.a shows the image of the SPS sintered sample with the lowest porosity. The additive could not be sufficiently distributed within the structure and formed clusters due to the speed of the SPS method. Fig. 3.63.b shows the image of the sample sintered with the GPS with carbon sheets showing phase separation. Fig. 3.63.c shows the image of the sample sintered with the GPS method without a carbon sheet.

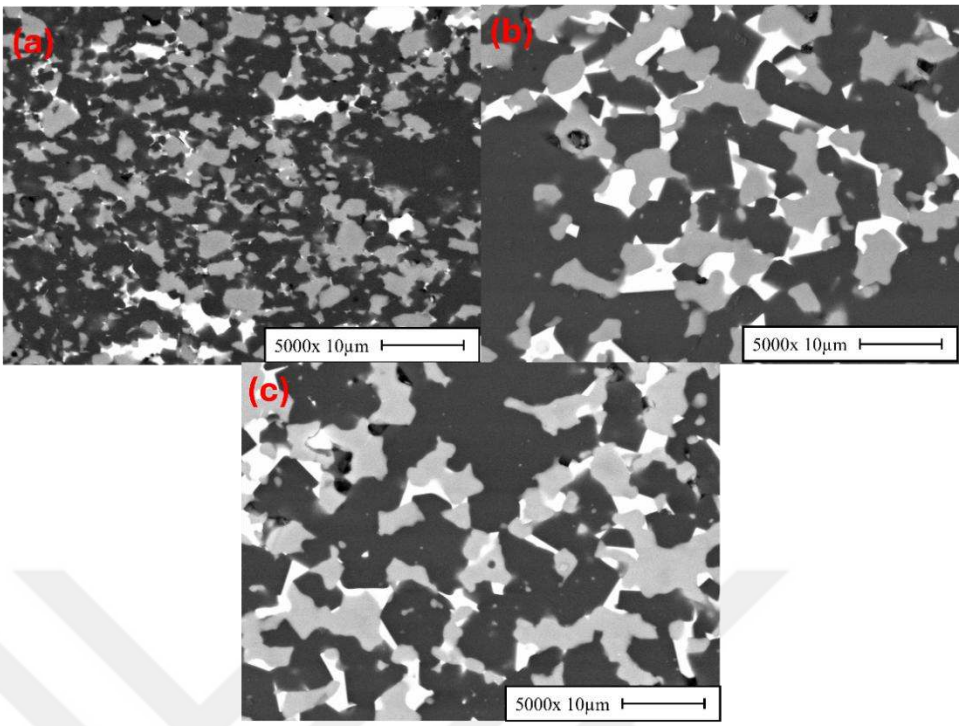

Figure 3.63. *Representative backscattered SEM images taken from polished surface of ATZ-5Yb sintered using different methods. (a) SPS, (b) GPS with carbon sheet and (c) GPS without carbon sheet*

Fig. 3.64 shows the EDS analysis of the ATZ-5Yb composition in backscattered mode at 1250x magnification. According to the results of the analysis, the main components of the composition were Al_2O_3, TiC and ZrO_2 with oxygen (O), which was the highest with a 44.03 wt.%. This confirms that the ATZ matrix was largely Al_2O_3 based. Aluminum (Al) was detected at 28.09 wt.% and titanium (Ti) was detected with 17.12 wt.%. It supports the existence of Al_2O_3 and TiC phases in the ATZ structure. Zirconium (Zr) was detected with 1.61 wt.% indicating the presence of ZrO_2 added to the ATZ composition.

This analysis detected ytterbium (Yb) element with 2.74 wt.% in this analysis. This ratio shows that the Yb_2O_3 contribution in the material after the sintering process was successfully incorporated into the composition and supported the formation of the $Yb_3Al_5O_{12}$ phase observed in the XRD analysis. The carbon (C) content was determined to be 6.41 wt.% due to the TiC content and possible carbon residues used in the sintering process.

Element	Weight%	Atomic%
C	6,41	11,32
O	44,03	58,33
Al	28,09	22,06
Ti	17,12	7,58
Zr	1,61	0,37
Yb	2,74	0,34

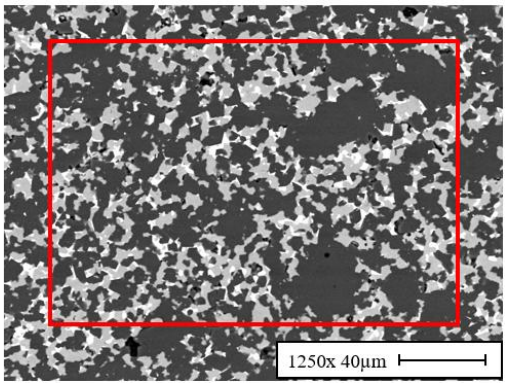

Figure 3.64. *Representative backscattered SEM image and EDS analysis taken from the polished surface of ATZ-5Yb*

Table 3.22 compares the mechanical properties (hardness and fracture toughness) of samples of ATZ-5Yb composition produced with different sintering methods. Mechanical tests were not performed since the relative density of the sample sintered with the carbon sheet GPS was low.

Table 3.22. *Mechanical properties of ATZ-5Yb compositions*

Sintering Method	Hardness (GPa)	Fracture Toughness (MPa $m^{1/2}$)
SPS	17.99	4.38
GPS	16.19	5.41

The hardness of the sample sintered with SPS was measured as 17.99 GPa. However, the fracture toughness of the sample sintered with SPS was measured as 4.38 MPa $m^{1/2}$, which was lower than the sample sintered with the GPS method. The sample sintered with the GPS method reached 16.19 GPa hardness and 5.41 MPa $m^{1/2}$ fracture toughness values. The higher hardness of the sample sintered with GPS can be explained by the longer sintering process and more stable phase formations. The higher fracture toughness indicates that better grain bonding may have been achieved during the GPS sintering. The $Yb_3Al_5O_{12}$ phase formed by Yb_2O_3 doping may have improved these mechanical properties.

Fig. 3.65 shows the backscattered SEM images comparing the crack propagation mechanism in SPS and GPS sintered samples of ATZ-5Yb composition. Fig. 3.65.a represents the sample sintered with the SPS method and fig. 3.65.b represents the sample sintered with the GPS method. Transgranular and intergranular crack propagation mechanisms were observed in both samples. However, it was determined that the crack bridging mechanism occurred in the sample using the GPS method.

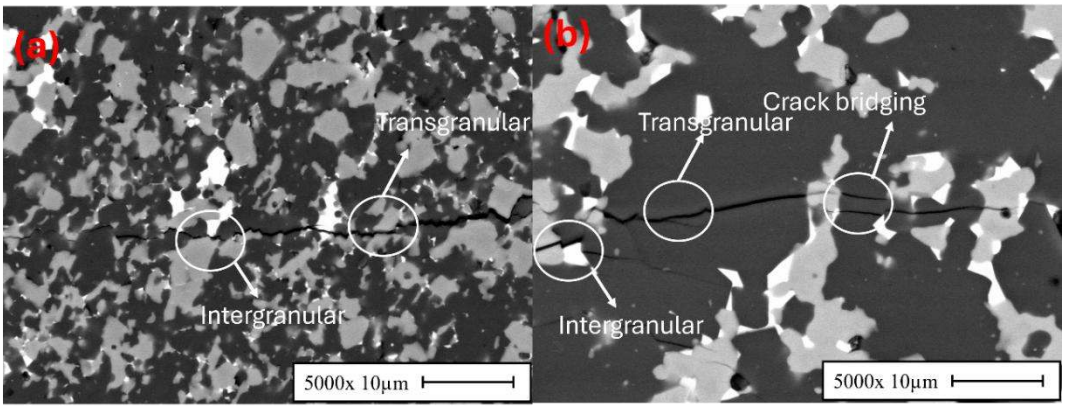

Figure 3.65. *Representative backscattered SEM images taken from polished surface of crack propagation of ATZ-5Yb (a) SPS sintered sample, (b) GPS sintered sample*

In fig. 3.66, the darkest areas were Al_2O_3, medium bright areas were TiC and the brightest grains were $Yb_3Al_5O_{12}$. The porosity remaining within the alumina grain during sintering was visible. The detection of $Yb_3Al_5O_{12}$ in XRD analysis indicates that Yb_2O_3 reacts with Al_2O_3 and forms garnet type $Yb_3Al_5O_{12}$.

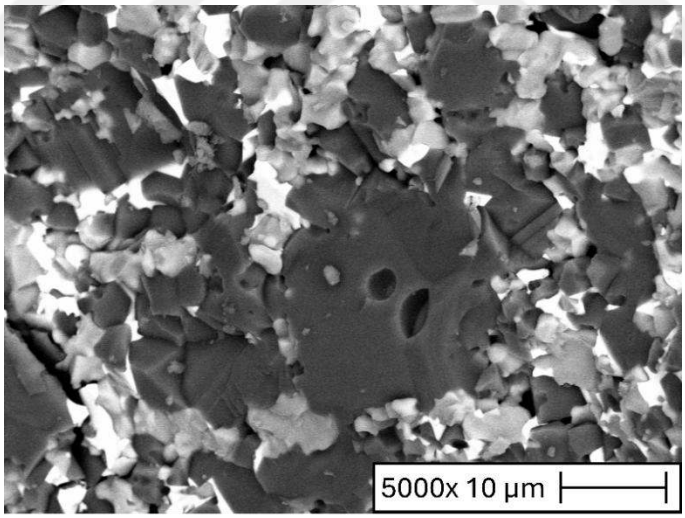

Figure 3.66. *Representative backscattered SEM image taken from the fractured surface of ATZ-3.5Yb*

3.6.3. Y_2O_3 additives

Samples were produced using different sintering methods by adding 3.5 wt.% and 5 wt.% Y_2O_3 to the ATZ composition and the effects of these methods on the material properties were compared. Sintering processes were carried out using three different methods: SPS, GPS with a carbon sheet and GPS without a carbon sheet. The densities

of the obtained samples were analyzed in detail, their mechanical properties were evaluated and microstructural studies were carried out.

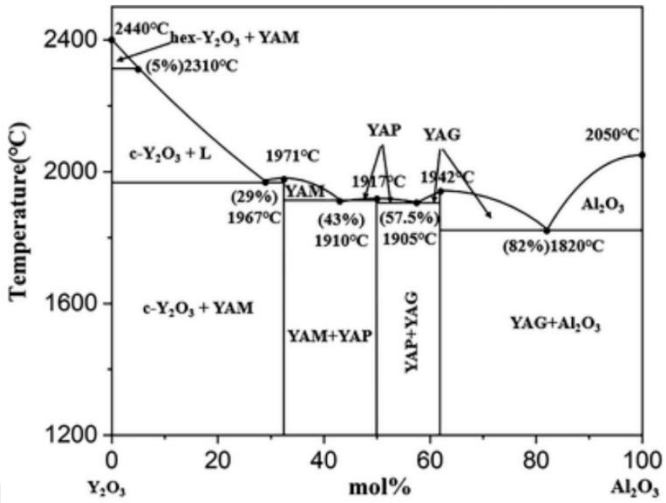

Figure 3.67. *Representative phase diagram of Al_2O_3-Y_2O_3. (Zhang, et al., 2022)*

Studies conducted by Chae et al. (Chae and Kim, 1993) reported that when Y_2O_3 was added to the Al_2O_3 matrix, the $Y_3Al_5O_{12}$ (Yttrium Aluminum Garnet – YAG) phase was formed and this phase left porosity in surface contact with Al_2O_3. This increases the risk of porosity formation during sintering, affecting the density and mechanical properties of the composite. In this study, the formation of $Y_3Al_5O_{12}$ phase in ATZ composition and the effect of this phase on mechanical properties were evaluated by XRD, SEM and mechanical tests.

The SPS method was used to understand the sintering behavior of ATZ-3.5Y composition. SPS provides important information about the sintering behavior of the material, as it provides densification at high temperature and in a short time. The shrinkage behavior of the sample was followed by the displacement curve and the critical temperatures for the sintering process were determined during the SPS sintering process.

According to fig. 3.68, the temperature at which the displacement curve starts to increase (Tshr) was determined as 1350 °C for ATZ-3.5Y. This temperature represents the threshold at which the pores of the sample begin to close and the material enters the densification process. The temperature at which the displacement curve remains constant (Tsin) was measured as 1640 °C. This temperature represents the point at which the sample reaches the closest level to full density and the material completes the sintering

process. Predetermined parameters were used for the GPS sintering study. Sintering was performed with the same parameters with and without a carbon sheet.

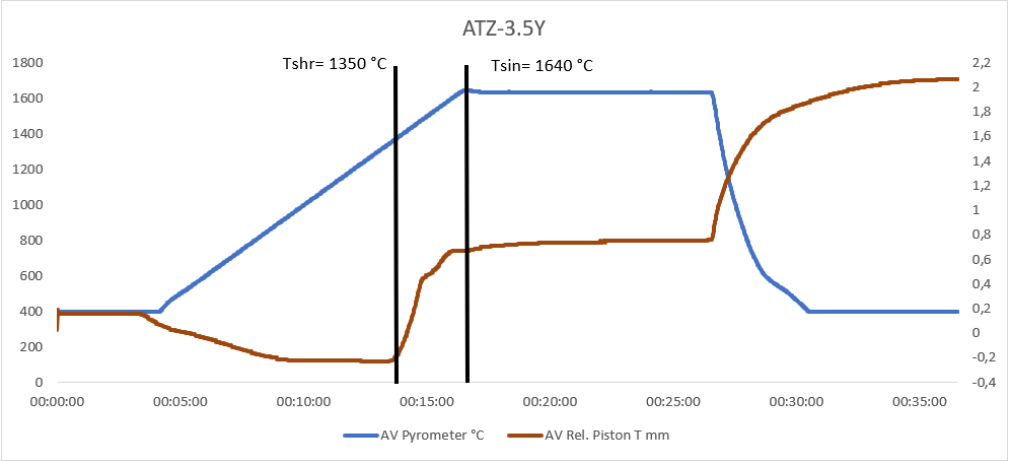

Figure 3.68. *Representative SPS graphic of ATZ-3.5Y composition*

Table 3.23 shows the relative density (%) values of samples of ATZ-3.5Y composition produced by three different sintering methods. The sample sintered with the SPS method achieved the highest density by reaching 98.90% relative density. This shows that SPS minimizes porosity by sintering the material quickly and effectively under the influence of high temperature and electrical current. The relative density of the sample sintered with the GPS – carbon sheet was 94.57%. This shows that carbon sheets have a negative effect on the sintering process. The carbon sheet prevented full densification during sintering due to oxygen limitation and increased the porosity level of the sample. The sample sintered with the GPS method without a carbon sheet reached a relative density of 97.09% and a more successful sintering process than the GPS method with a carbon sheet. The sintering atmosphere was more stable and the material was densified more homogeneously when a carbon sheet was not used. However, since the GPS method took longer and was under lower pressure than SPS, it could not achieve a density as high as SPS.

Table 3.23. *Sintering methods and relative densities of ATZ-3.5Y composition*

Sintering Method	Relative Density (%)
SPS	98.90
GPS – Carbon Sheet	94.57
GPS	97.09

Fig. 3.69 compares the backscattered SEM images of ATZ-3.5Y composition obtained with different sintering methods at 5000x magnification. Fig. 3.69.a shows the image of the SPS sintered sample, with the lowest porosity. The additive could not be sufficiently distributed within the structure and formed clusters due to the speed of the SPS method. Fig. 3.69.b shows the image of the sample sintered with the GPS with a carbon sheet, showing high porosity and phase separation. Pores formed at the grain boundaries and a homogeneous structure could not be obtained since the carbon sheet could not fully densify during the sintering process. Fig. 3.69.c shows that the image of the sample sintered with the GPS method without carbon sheet has a better microstructure than fig. 3.69.b. Less porosity was formed at grain boundaries, but certain irregularities in the phase distribution were observed.

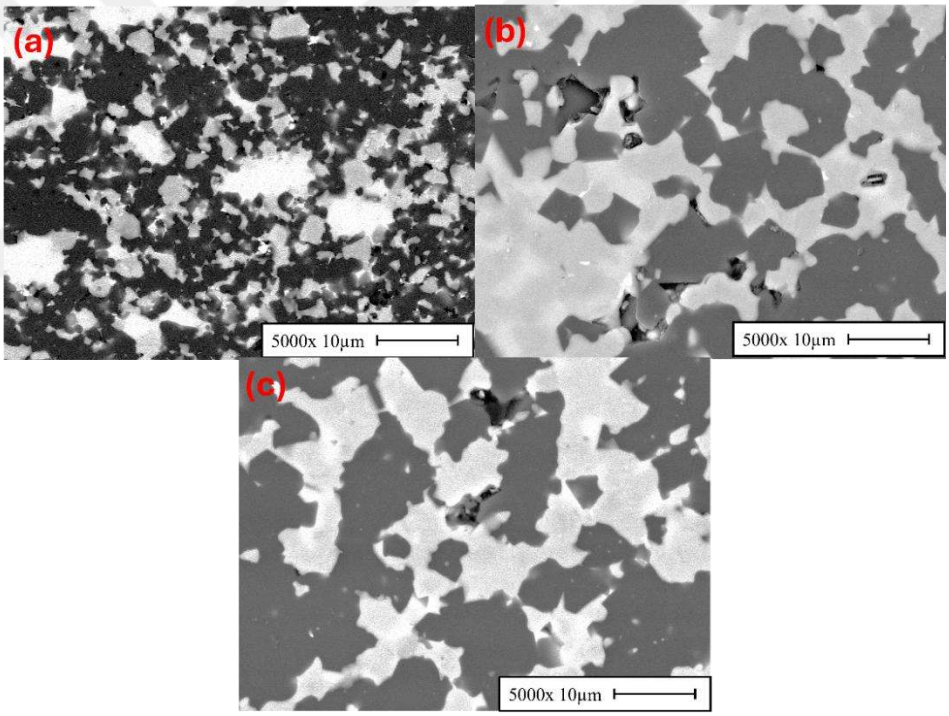

Figure 3.69. *Representative backscattered SEM images taken from polished surface of ATZ-3.5 Y sintered using different methods. (a) SPS, (b) GPS with carbon sheet and (c) GPS without carbon sheet*

Fig. 3.70 shows the XRD analysis, comparing the composition of ATZ-3.5Y with the composition of ATZ. The ATZ composition (orange curve) consists of the main phases Al_2O_3, TiC and ZrO_2. Some peaks belonging to the carbon (C) phases were also observed, which were related to the carbon sheet or TiC content used in the sintering process.

The ATZ-3.5Y composition (gray curve) reveals how the Y_2O_3 addition changes the material's structure. XRD shows that Y_2O_3 doping reacts with Al_2O_3 forming the $Y_3Al_5O_{12}$ phase. This phase may contribute to stabilizing the microstructure and potentially improving mechanical properties by providing a new oxide contribution to the ATZ composition. It was seen that the new peak belonging to the $Y_3Al_5O_{12}$ phase appears clearly in the ATZ-3.5Y composition. Besides, other main phases (Al_2O_3, TiC and ZrO_2) in the ATZ composition remained intact, indicating that the overall structure of the material did not change significantly. However, the additive modified the matrix by forming a new phase.

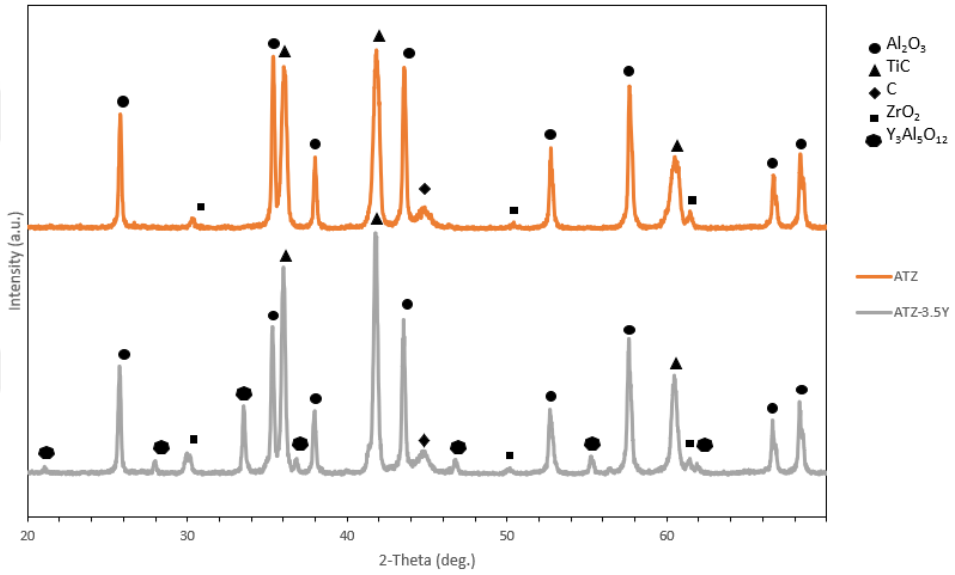

Figure 3.70. *Representative comparison of the XRD spectra of ATZ and ATZ-3.5Y*

Fig. 3.71 shows the EDS analysis of the ATZ-3.5Y composition in backscattered mode at 1250x magnification. According to the results of the analysis, the main components of the composition were Al_2O_3, TiC and ZrO_2 with oxygen (O), which was the highest with a 44.20 wt.%. This confirms that the ATZ matrix was largely Al_2O_3 based. Aluminum (Al) was detected with 26.32 wt.% and titanium (Ti) was detected with 17.32 wt.%. It supports the existence of Al_2O_3 and TiC phases in the ATZ structure. Zirconium (Zr) was detected with 1.45 wt.% indicating the presence of ZrO_2 added to the ATZ composition.

This analysis detected the yttrium (Y) element was detected with 0.72 wt.%. This ratio shows that the Y_2O_3 contribution in the material after the sintering process was

successfully incorporated into the composition and supported the formation of the $Y_3Al_5O_{12}$ phase observed in the XRD analysis. The carbon (C) content was determined to be 9.99 wt.% due to the TiC content and possible carbon residues used in the sintering process.

Element	Weight%	Atomic%
C	9,99	16,79
O	44,20	55,75
Al	26,32	19,68
Ti	17,32	7,30
Y	0,72	0,16
Zr	1,45	0,32

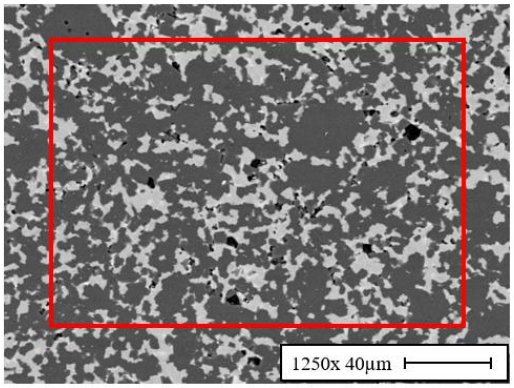

Figure 3.71. *Representative backscattered SEM image and EDS analysis taken from the polished surface of ATZ-3.5Y*

Table 3.24 compares the mechanical properties (hardness and fracture toughness) of samples of ATZ-3.5Y composition produced with different sintering methods. Mechanical tests were not performed since the relative density of the sample sintered with the carbon sheet GPS was low.

Table 3.24. *Mechanical properties of ATZ-3.5Y compositions*

Sintering Method	Hardness (GPa)	Fracture Toughness (MPa $m^{1/2}$)
SPS	18.17	4.26
GPS	17.37	4.01

The hardness of the sample sintered with SPS was measured as 18.17 GPa. However, the fracture toughness of the sample sintered with SPS was measured as 4.26 MPa $m^{1/2}$, which was lower than the sample sintered with the GPS method. The sample sintered with the GPS method reached 17.37 GPa hardness and 4.01 MPa $m^{1/2}$ fracture toughness values. The higher hardness of the sample sintered with GPS can be explained by the longer sintering process and more stable phase formations. The higher fracture toughness indicates that better grain bonding may have been achieved during the GPS sintering. The $Y_3Al_5O_{12}$ phase formed by Y_2O_3 doping may have improved these mechanical properties.

Fig. 3.72 shows the backscattered SEM images comparing the crack propagation mechanism in SPS and GPS sintered samples of ATZ-3.5Y composition. Fig. 3.72.a represents the sample sintered with the SPS method and fig. 3.72.b represents the sample sintered with the GPS method. Transgranular and intergranular crack propagation mechanisms were observed in both samples.

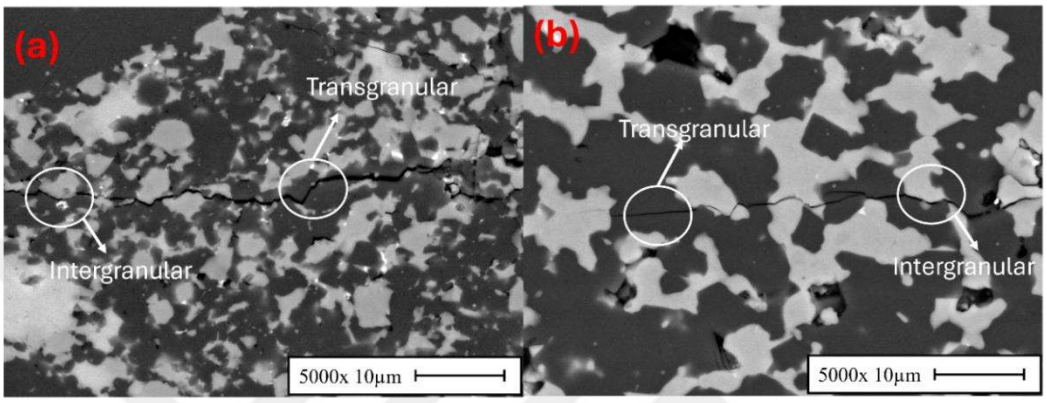

Figure 3.72. *Representative backscattered SEM images taken from polished surface of crack propagation of ATZ-3.5Y sample, (a) SPS sintered sample, (b) GPS sintered sample*

The SPS method was used to understand the sintering behavior of ATZ-5Y composition. SPS provides important information about the sintering behavior of the material as it provides densification at high temperature and in a short time. The shrinkage behavior of the sample was followed by the displacement curve and the critical temperatures for the sintering process were determined during the SPS sintering process.

According to fig. 3.73, the temperature at which the displacement curve starts to increase (Tshr) was determined as 1370 °C for ATZ-5Y. This temperature represents the threshold at which the pores of the sample begin to close and the material enters the densification process. The temperature at which the displacement curve remains constant (Tsin) was measured as 1640 °C. This temperature represents the point at which the sample reaches the closest level to full density and the material completes the sintering process. Predetermined parameters were used for the GPS sintering study. Sintering was performed with the same parameters with and without a carbon sheet.

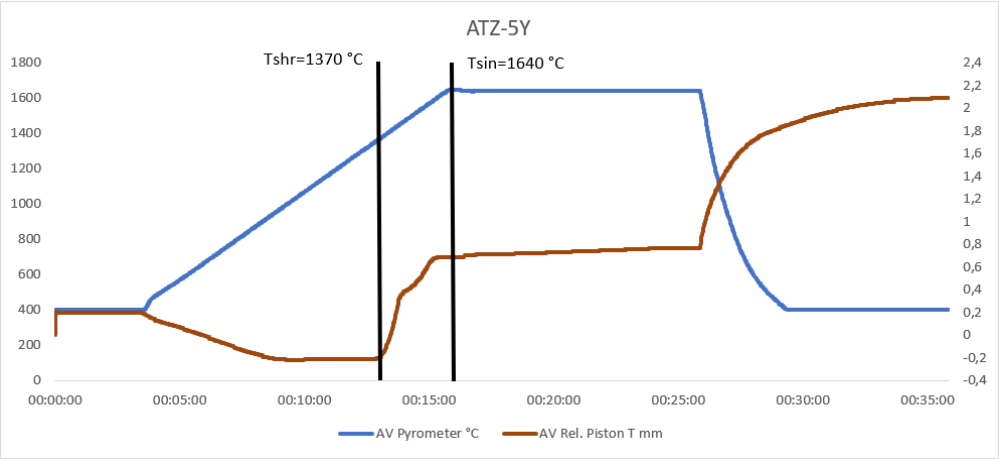

Figure 3.73. *Representative SPS graphic of ATZ-5Y composition*

Table 3.25 shows the relative density (%) values of samples of ATZ-5Y composition produced by three different sintering methods. The sample sintered with the SPS method achieved the highest density by reaching 98.14% relative density. This shows that SPS minimizes porosity by sintering the material quickly and effectively under the influence of high temperature and electrical current. The relative density of the sample sintered with the GPS – carbon sheet was measured as 90.24%. This shows that carbon sheets have a negative effect on the sintering process. The carbon sheet prevented full densification during sintering due to oxygen limitation and increased the porosity level of the sample. The sample sintered with the GPS method without a carbon sheet reached a relative density of 96.16% and a more successful sintering process compared to the GPS method with a carbon sheet. The sintering atmosphere was more stable and the material was densified more homogeneously when a carbon sheet was not used. However, since the GPS method took longer and under lower pressure than SPS, it could not achieve a density as high as SPS.

Table 3.25. *Sintering methods and relative densities of ATZ-5Y composition*

Sintering Method	Relative Density (%)
SPS	98.14
GPS – Carbon Sheet	90.24
GPS	96.16

Fig. 3.74 compares the backscattered SEM images of ATZ-5Y composition obtained with different sintering methods at 5000x magnification. Fig. 3.74.a shows the image of the SPS sintered sample with the lowest porosity. The additive could not be

sufficiently distributed within the structure and formed clusters due to the speed of the SPS method. Fig. 3.74.b shows the image of the sample sintered with the GPS with a carbon sheet, showing high porosity and phase separation. Pores formed at the grain boundaries and a homogeneous structure could not be obtained since the carbon sheet could not fully densify during the sintering process. Fig. 3.74.c shows that the image of the sample sintered with the GPS method without carbon sheet has a better microstructure than fig. 3.74.b. Less porosity was formed at grain boundaries but certain irregularities in the phase distribution were observed.

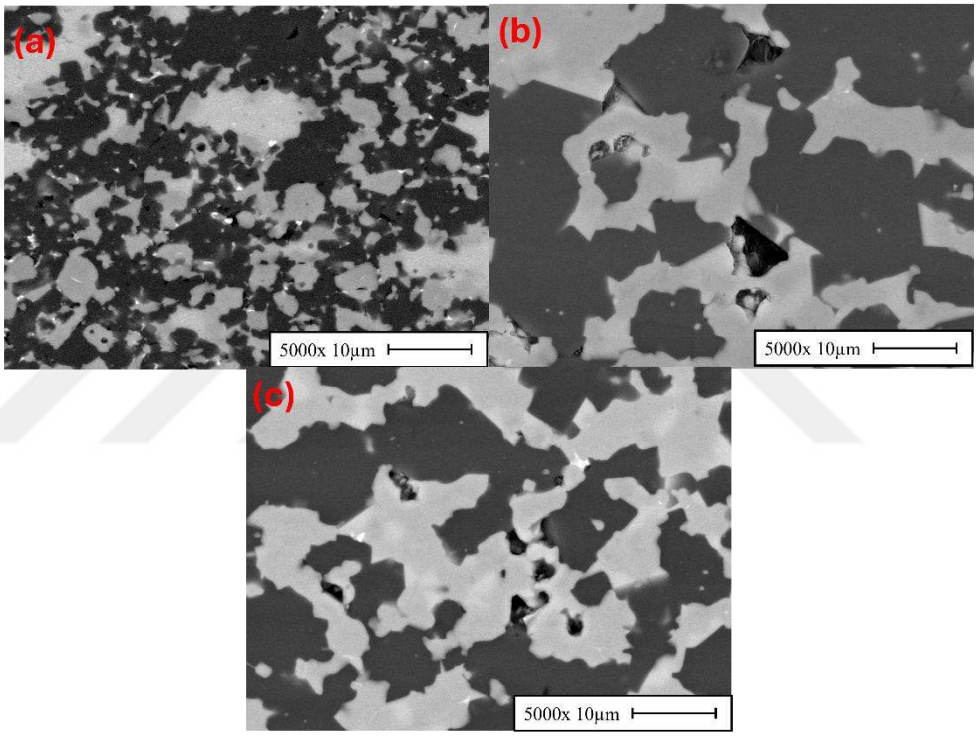

Figure 3.74. *Representative backscattered SEM images taken from polished surface of ATZ-Y5 sintered using different methods. (a) SPS, (b) GPS with carbon sheet and (c) GPS without carbon sheet*

Fig. 3.75 shows the EDS analysis of the ATZ-5Y composition in backscattered mode at 1250x magnification. According to the analysis results, the main components of the composition were Al_2O_3, TiC and ZrO_2 with oxygen (O), which was the highest with a 43.00 wt.%. This confirms that the ATZ matrix was largely Al_2O_3 based. Aluminum (Al) was detected with 25.17 wt.% and titanium (Ti) with 19.66 wt.%. It supports the existence of Al_2O_3 and TiC phases in the ATZ structure. Zirconium (Zr) was detected with 1.86 wt.%, indicating the presence of ZrO_2 added to the ATZ composition.

Yttrium (Y) element was detected with 1.67 wt.% in this analysis. This ratio shows that the Y_2O_3 contribution in the material after the sintering process was successfully incorporated into the composition and supported the formation of the $Y_3Al_5O_{12}$ phase observed in the XRD analysis. The carbon (C) content was determined to be 8.65 wt.% due to the TiC content and possible carbon residues used in the sintering process.

Element	Weight%	Atomic%
C	8,65	15,03
O	43,00	56,11
Al	25,17	19,47
Ti	19,66	8,57
Y	1,67	0,39
Zr	1,86	0,43

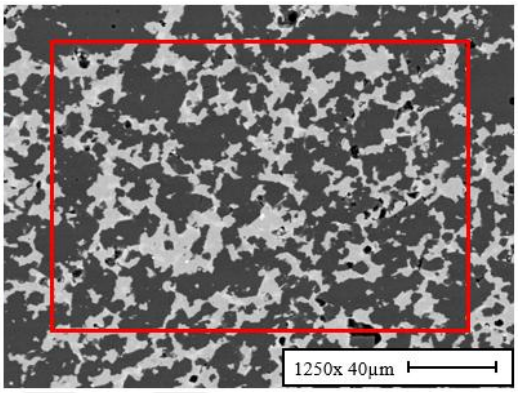

Figure 3.75. *Representative backscattered SEM image and EDS analysis taken from the polished surface of ATZ-5Y*

Table 3.26 compares the mechanical properties (hardness and fracture toughness) of samples of ATZ-5Y composition produced with different sintering methods. Mechanical tests were not performed since the relative density of the sample sintered with the carbon sheet GPS was low.

Table 3.26. *Mechanical properties of ATZ-5Y compositions*

Sintering Method	Hardness (GPa)	Fracture Toughness (MPa $m^{1/2}$)
SPS	17.63	4.36
GPS	17.24	4.32

The hardness of the sample sintered with SPS was measured as 17.63 GPa. However, the fracture toughness of the sample sintered with SPS was measured as 4.36 MPa $m^{1/2}$, which was lower than the sample sintered with the GPS method. The sample sintered with the GPS method reached 17.24 GPa hardness and 4.32 MPa $m^{1/2}$ fracture toughness values. The higher hardness of the sample sintered with GPS can be explained by the longer sintering process and more stable phase formations. The higher fracture toughness indicates that better grain bonding may have been achieved during the GPS

sintering. The $Y_3Al_5O_{12}$ phase formed by Y_2O_3 doping may have improved these mechanical properties.

Fig. 3.76 shows the backscattered SEM images comparing the crack propagation mechanism in SPS and GPS sintered samples of ATZ-5Y composition. Fig. 3.76.a represents the sample sintered with the SPS method and fig. 3.76.b represents the sample sintered with the GPS method. Transgranular and intergranular crack propagation mechanisms were observed in both samples.

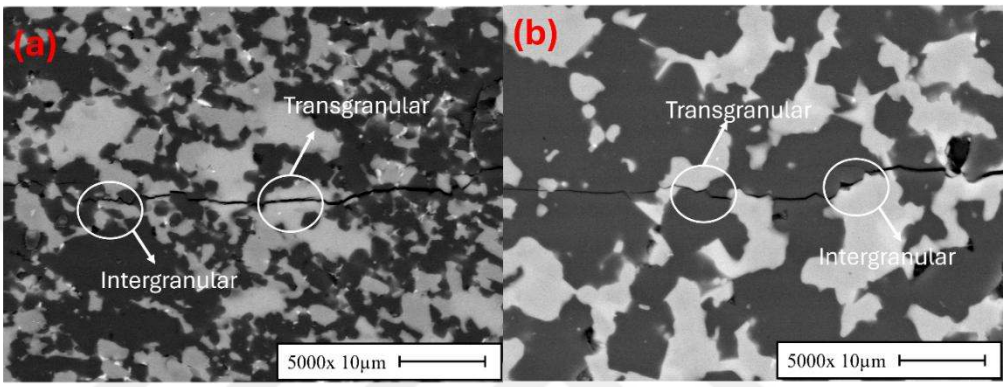

Figure 3.76. *Representative backscattered SEM images taken from polished surface of crack propagation of ATZ-5Y sample, (a) SPS sintered sample, (b) GPS sintered sample*

In fig. 3.77, medium bright TiC grains and brighter YAG phases were homogeneously distributed in the dark Al_2O_3 matrix.

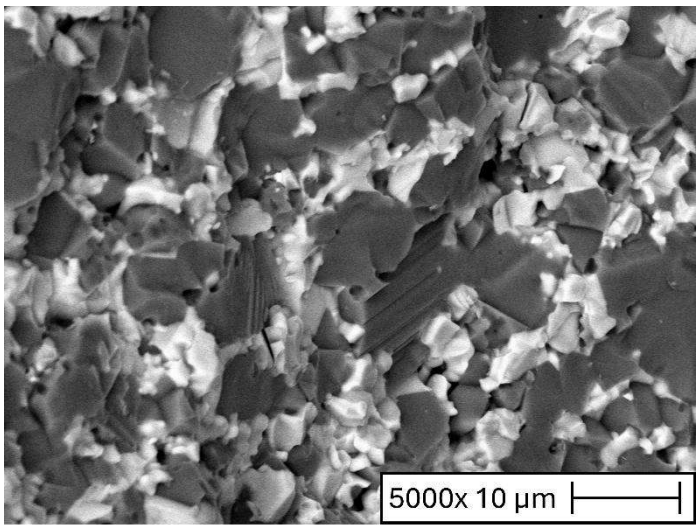

Figure 3.77. *Representative backscattered SEM image taken from the fractured surface of ATZ-3.5Y*

3.6.4. Sm_2O_3 additives

Samples were produced using different sintering methods by adding 3.5 wt.% and 5 wt.% Sm_2O_3 to the ATZ composition and the effects of these methods on the material properties were compared. Sintering processes were carried out using three different methods: SPS, GPS with a carbon sheet and GPS without a carbon sheet. The densities of the obtained samples were analyzed in detail, their mechanical properties were evaluated and microstructural studies were carried out.

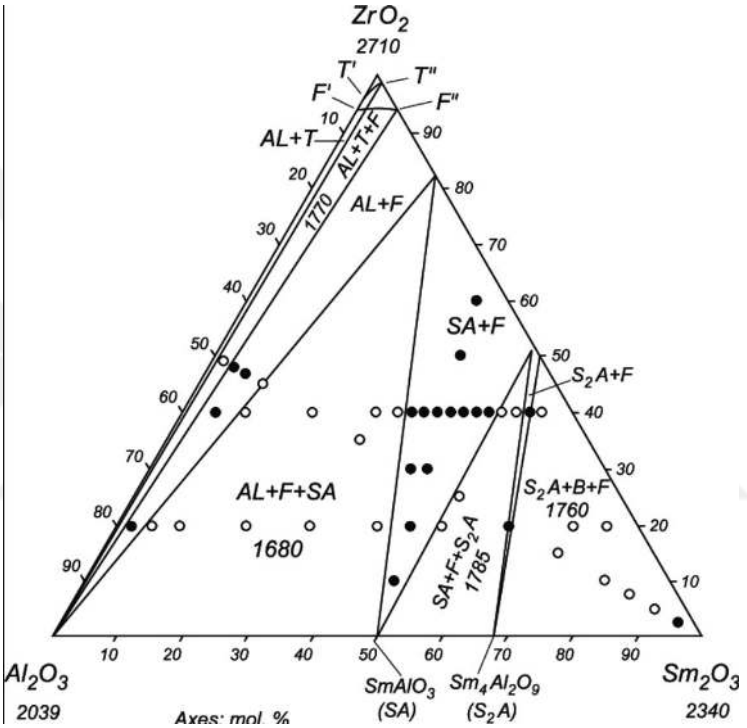

Figure 3.78. *Representative ternary phase diagram of Al_2O_3-Sm_2O_3-ZrO_2. (Lakiza and Lopato, 2006)*

Studies conducted by Taşdemir et al. (Taşdemir et al., 2023) reported that when Sm_2O_3 was added to the Al_2O_3 matrix, the $SmAlO_3$ (Samarium Aluminate) perovskite phase was formed, unlike other rare earth oxides. This phase can have a limiting effect on grain growth during sintering and increase the fracture toughness. In this study, the formation of $SmAlO_3$ phase in ATZ composition and the effect of this phase on mechanical properties were evaluated by XRD, SEM and mechanical tests.

The SPS method was used to understand the sintering behavior of ATZ-3.5Sm composition. SPS provides important information about the sintering behavior of the material, as it provides densification at high temperature and in a short time. The

shrinkage behavior of the sample was followed by the displacement curve and the critical temperatures for the sintering process were determined during the SPS sintering process.

According to fig. 3.79, the temperature at which the displacement curve starts to increase (Tshr) was determined as 1310 °C for ATZ-3.5Sm. This temperature represents the threshold at which the pores of the sample begin to close and the material enters the densification process. The temperature at which the displacement curve remains constant (Tsin) was measured as 1580 °C. This temperature represents the point at which the sample reaches the closest level to full density and the material completes the sintering process. Predetermined parameters were used for the GPS sintering study. Sintering was performed with the same parameters with and without a carbon sheet.

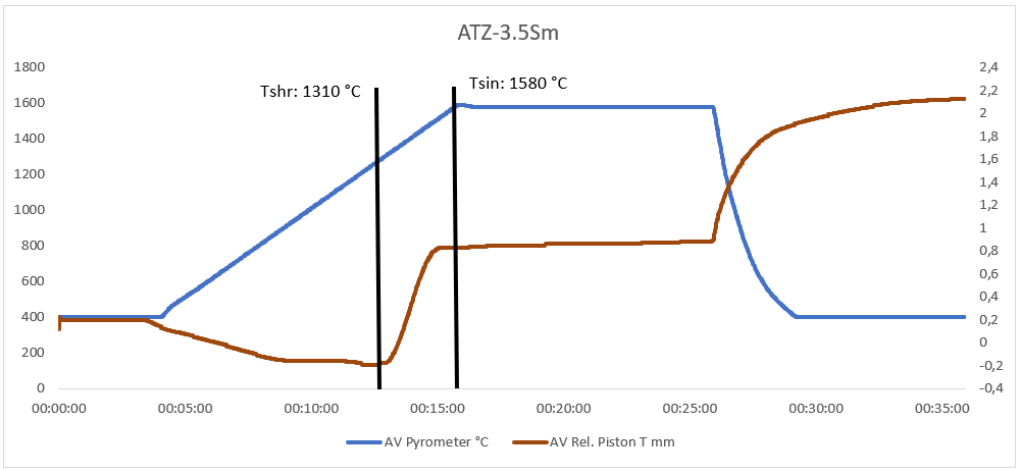

Figure 3.79. *Representative SPS graphic of ATZ-3.5Sm composition*

Table 3.27 shows the relative density (%) values of samples of ATZ-3.5Sm composition produced by three different sintering methods. The sample sintered with the SPS method achieved the highest density by reaching 99.56% relative density. This shows that SPS minimizes porosity by sintering the material quickly and effectively under the influence of high temperature and electrical current. The relative density of the sample sintered with the GPS – carbon sheet was 95.33%. This shows that carbon sheets have a negative effect on the sintering process. The carbon sheet prevented full densification during sintering due to oxygen limitation and increased the porosity level of the sample. The sample sintered with the GPS method without a carbon sheet reached a relative density of 96.68% and a more successful sintering process than the GPS method with a carbon sheet. The sintering atmosphere was more stable and the material was densified

more homogeneously when a carbon sheet was not used. However, since the GPS method took longer and under lower pressure than SPS, it could not achieve a density as high as SPS.

Table 3.27. *Sintering methods and relative densities of ATZ-3.5Sm composition*

Sintering Method	Relative Density (%)
SPS	99.56
GPS – Carbon Sheet	95.33
GPS	96.68

Fig. 3.80 compares the backscattered SEM images of ATZ-3.5Sm composition obtained with different sintering methods at 5000x magnification. Fig. 3.80.a shows the image of the SPS sintered sample with the lowest porosity. The additive could not be sufficiently distributed within the structure and formed clusters due to the speed of the SPS method. Fig. 3.80.b shows the image of the sample sintered with the GPS with a carbon sheet, showing high porosity and phase separation. Pores formed at the grain boundaries and a homogeneous structure could not be obtained since the carbon sheet could not fully densify during the sintering process. Fig. 3.80.c shows that the image of the sample sintered with the GPS method without carbon sheet has a better microstructure than fig. 3.80.b. Less porosity was formed at grain boundaries, but certain irregularities in the phase distribution were observed.

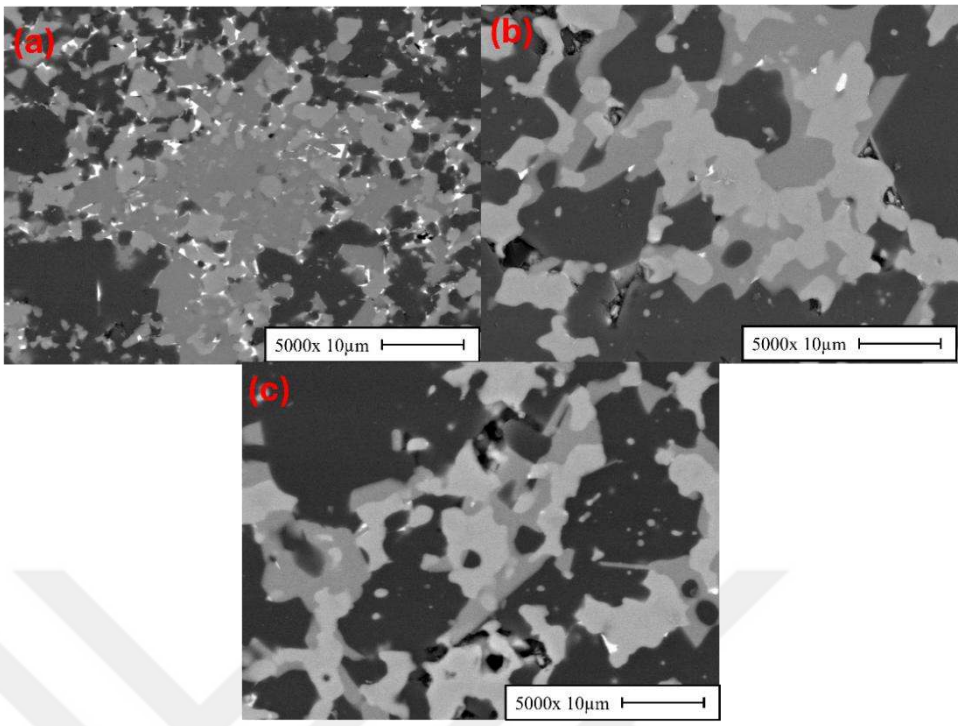

Figure 3.80. *Representative backscattered SEM images taken from polished surface of ATZ-3.5Sm sintered using different methods. (a) SPS, (b) GPS with carbon sheet and (c) GPS without carbon sheet*

Fig. 3.81 shows the XRD analysis, comparing the composition of ATZ-3.5Sm with the composition of ATZ. The ATZ composition (orange curve) consists of the main phases Al_2O_3, TiC and ZrO_2. Some peaks belonging to the carbon (C) phases were also observed, which were related to the carbon sheet or TiC content used in the sintering process.

The ATZ-3.5Sm composition (gray curve) reveals how the Sm_2O_3 addition changes the material's structure. XRD shows that Sm_2O_3 doping reacts with Al_2O_3 forming the $SmAlO_3$ phase. This phase may contribute to stabilizing the microstructure and potentially improving mechanical properties by providing a new oxide contribution to the ATZ composition. It was seen that the new peak belonging to the $SmAlO_3$ phase appears clearly in the ATZ-3.5Sm composition. Besides, other main phases (Al_2O_3, TiC and ZrO_2) in the ATZ composition remained intact, indicating that the overall structure of the material did not change significantly. However, the additive modified the matrix by forming a new phase.

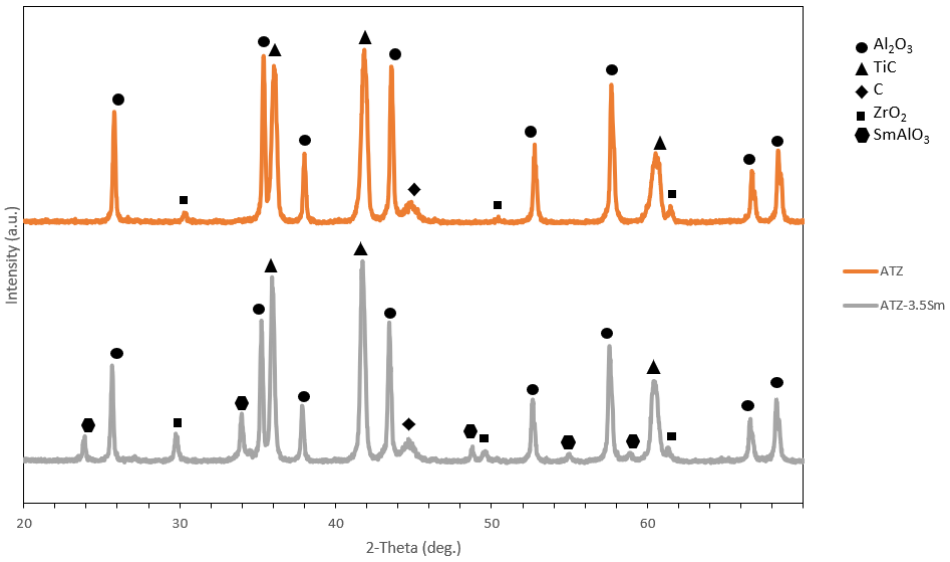

Figure 3.81. *Representative comparison of the XRD spectra of ATZ and ATZ-3.5Sm*

Fig. 3.82 shows the EDS analysis of the ATZ-3.5Sm composition in backscattered mode at 1250x magnification. According to the analysis results, the main components of the composition were Al_2O_3, TiC and ZrO_2 with oxygen (O), which was the highest with a 42.50 wt.%. This confirms that the ATZ matrix was largely Al_2O_3 based. Aluminum (Al) was detected with 27.69 wt.% and titanium (Ti) was detected with 18.22 wt.%. It supports the existence of Al_2O_3 and TiC phases in the ATZ structure. Zirconium (Zr) was detected with 2.13 wt.% indicating the presence of ZrO_2 added to the ATZ composition.

This analysis detected samarium (Sm) element with 1.62 wt.%. This ratio shows that the Sm_2O_3 contribution in the material after the sintering process was successfully incorporated into the composition and supported the formation of the $SmAlO_3$ phase observed in the XRD analysis. The carbon (C) content was determined to be 7.86 wt.% due to the TiC content and possible carbon residues used in the sintering process.

Element	Weight%	Atomic%
C	7,86	13,77
O	42,5	55,91
Al	27,69	21,60
Ti	18,22	8,00
Zr	2,13	0,49
Sm	1,62	0,23

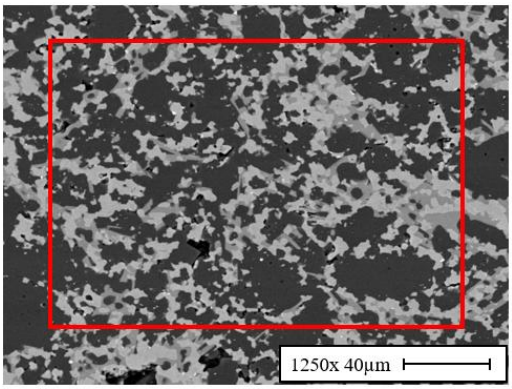

Figure 3.82. *Representative backscattered SEM image and EDS analysis taken from the polished surface of ATZ-3.5Sm*

Table 3.28 compares the mechanical properties (hardness and fracture toughness) of samples of ATZ-3.5Sm composition produced with different sintering methods. Mechanical tests were not performed since the relative density of the sample sintered with the carbon sheet GPS was low.

Table 3.28. *Mechanical properties of ATZ-3.5Sm compositions*

Sintering Method	Hardness (GPa)	Fracture Toughness (MPa $m^{1/2}$)
SPS	17.59	4.85
GPS	17.88	5.37

The hardness of the sample sintered with SPS was measured as 17.59 GPa. However, the fracture toughness of the sample sintered with SPS was measured as 4.85 MPa $m^{1/2}$, which was lower than the sample sintered with the GPS method. The sample sintered with the GPS method reached 17.88 GPa hardness and 5.37 MPa $m^{1/2}$ fracture toughness values. The higher hardness of the sample sintered with GPS can be explained by the longer sintering process and more stable phase formations. The higher fracture toughness indicates that better grain bonding may have been achieved during the GPS sintering. The $SmAlO_3$ phase formed by Sm_2O_3 doping may have improved these mechanical properties.

Fig. 3.83 shows the backscattered SEM images comparing the crack propagation mechanism in SPS and GPS sintered samples of ATZ-3.5Sm composition. Fig. 3.83.a represents the sample sintered with the SPS method and fig. 3.83.b represents the sample sintered with the GPS method. Transgranular and intergranular crack propagation mechanisms were observed in both samples.

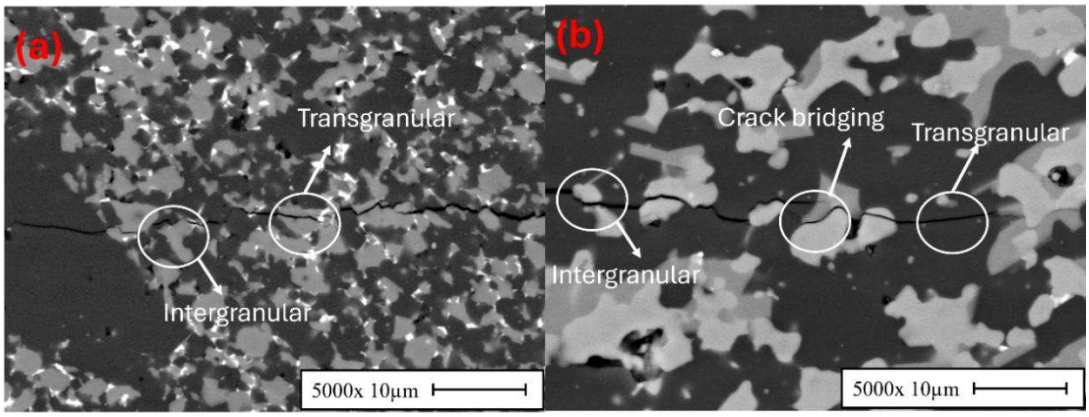

Figure 3.83. *Representative backscattered SEM images taken from polished surface of crack propagation of ATZ-3.5Sm sample, (a) SPS sintered sample, (b) GPS sintered sample*

The SPS method was used to understand the sintering behavior of ATZ-5Sm composition. SPS provides important information about the sintering behavior of the material, as it provides densification at high temperature and in a short time. The shrinkage behavior of the sample was followed by the displacement curve and the critical temperatures for the sintering process were determined during the SPS sintering process.

According to fig. 3.84, the temperature at which the displacement curve starts to increase (Tshr) was determined as 1315 °C for ATZ-5Sm. This temperature represents the threshold at which the pores of the sample begin to close and the material enters the densification process. The temperature at which the displacement curve remains constant (Tsin) was measured as 1570 °C. This temperature represents the point at which the sample reaches the closest level to full density and the material completes the sintering process. Predetermined parameters were used for the GPS sintering study. Sintering was performed with the same parameters with and without a carbon sheet.

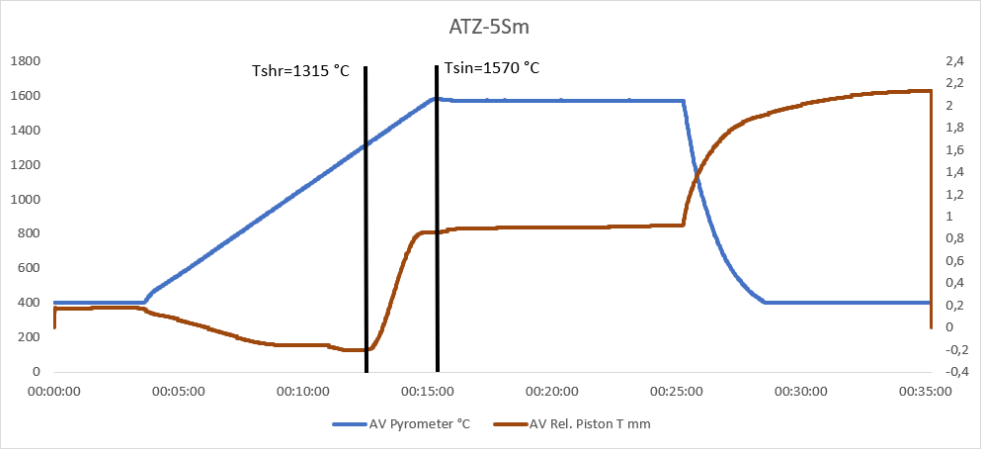

Figure 3.84. *Representative SPS graphic of ATZ-5Sm composition*

Table 3.29 shows the relative density (%) values of samples of ATZ-5Sm composition produced by three different sintering methods. The sample sintered with the SPS method achieved the highest density by reaching 99.21% relative density. This shows that SPS minimizes porosity by sintering the material quickly and effectively under the influence of high temperature and electrical current. The relative density of the sample sintered with the GPS – carbon sheet was 95.18%. This shows that carbon sheets have a negative effect on the sintering process. The carbon sheet prevented full densification during sintering due to oxygen limitation and increased the porosity level of the sample. The sample sintered with the GPS method without a carbon sheet reached a relative density of 95.92% and a more successful sintering process than the GPS method with a carbon sheet. The sintering atmosphere was more stable and the material was densified more homogeneously when a carbon sheet was not used. However, since the GPS method took longer and under lower pressure than SPS, it could not achieve a density as high as SPS.

Table 3.29. *Sintering methods and relative densities of ATZ-5Sm composition*

Sintering Method	Relative Density (%)
SPS	99.21
GPS – Carbon Sheet	95.18
GPS	95.92

Fig. 3.85 compares the backscattered SEM images of ATZ-5Sm composition obtained with different sintering methods at 5000x magnification. Fig. 3.85.a shows the image of the SPS sintered sample with the lowest porosity. The additive could not be

sufficiently distributed within the structure and formed clusters due to the speed of the SPS method. Fig. 3.85.b shows the image of the sample sintered with the GPS with a carbon sheet showing high porosity and phase separation. Pores formed at the grain boundaries and a homogeneous structure could not be obtained since the carbon sheet could not fully densify during the sintering process. Fig. 3.85.c shows that the image of the sample sintered with the GPS method without carbon sheet has a better microstructure than fig. 3.85.b. Less porosity was formed at grain boundaries, but certain irregularities in the phase distribution were observed.

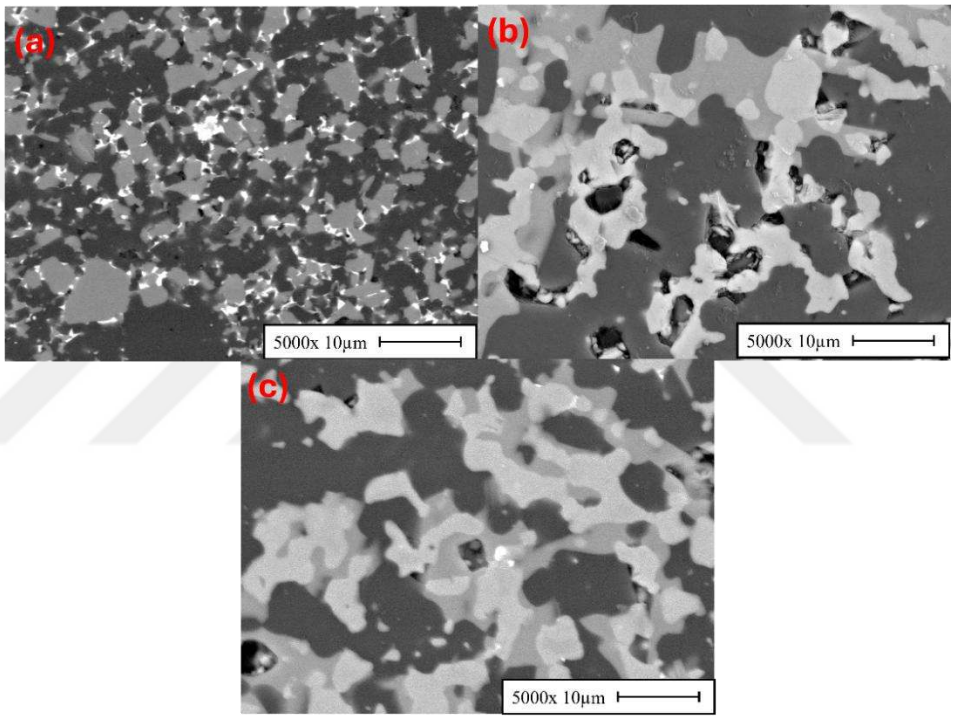

Figure 3.85. *Representative backscattered SEM images taken from polished surface of ATZ-5Sm sintered using different methods. (a) SPS, (b) GPS with carbon sheet and (c) GPS without carbon sheet*

Fig. 3.86 shows the EDS analysis of the ATZ-5Sm composition in backscattered mode at 1250x magnification. According to the analysis results, the main components of the composition were Al_2O_3, TiC and ZrO_2 with oxygen (O), which was the highest with a 44.27 wt.%. This confirms that the ATZ matrix was largely Al_2O_3 based. Aluminum (Al) was detected with 27.23 wt.% and titanium (Ti) was detected with 17.76 wt.%. It supports the existence of Al_2O_3 and TiC phases in the ATZ structure. Zirconium (Zr) was detected with 1.64 wt.% indicating the presence of ZrO_2 added to the ATZ composition.

This analysis detected samarium (Sm) element with 2.16 wt.%. This ratio shows that the Sm_2O_3 contribution in the material after the sintering process was successfully incorporated into the composition and supported the formation of the $SmAlO_3$ phase observed in the XRD analysis. The carbon (C) content was determined to be 6.93 wt.% due to the TiC content and possible carbon residues used in the sintering process.

Element	Weight%	Atomic%
C	6,93	12,13
O	44,27	58,17
Al	27,23	21,22
Ti	17,76	7,80
Zr	1,64	0,38
Sm	2,16	0,30

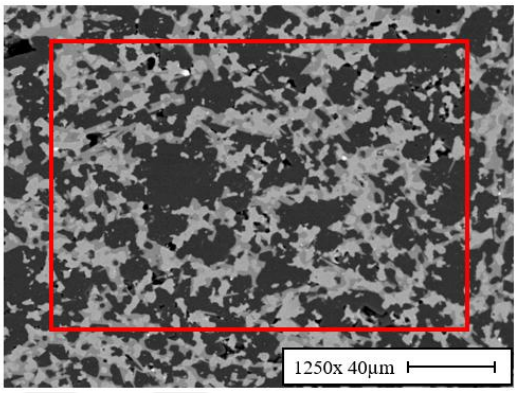

Figure 3.86. *Representative backscattered SEM image and EDS analysis taken from the polished surface of ATZ-5Sm*

Table 3.30 compares the mechanical properties (hardness and fracture toughness) of samples of ATZ-5Sm composition produced with different sintering methods. Mechanical tests were not performed since the relative density of the sample sintered with the carbon sheet GPS was low.

Table 3.30. *Mechanical properties of ATZ-5Sm compositions*

Sintering Method	Hardness (GPa)	Fracture Toughness (MPa $m^{1/2}$)
SPS	18.12	4.86
GPS	16.98	4.50

The hardness of the sample sintered with SPS was measured as 18.12 GPa. However, the fracture toughness of the sample sintered with SPS was measured as 4.86 MPa $m^{1/2}$, which was lower than the sample sintered with the GPS method. The sample sintered with the GPS method reached 16.98 GPa hardness and 4.5 MPa $m^{1/2}$ fracture toughness values. The higher hardness of the sample sintered with GPS can be explained by the longer sintering process and more stable phase formations. The higher fracture toughness indicates that better grain bonding may have been achieved during the GPS

sintering. The $SmAlO_3$ phase formed by Sm_2O_3 doping may have improved these mechanical properties.

Fig. 3.87 shows the backscattered SEM images comparing the crack propagation mechanism in SPS and GPS sintered samples of ATZ-5Sm composition. Fig. 3.87.a represents the sample sintered with the SPS method and fig. 3.87.b represents the sample sintered with the GPS method. Transgranular and intergranular crack propagation mechanisms were observed in both samples.

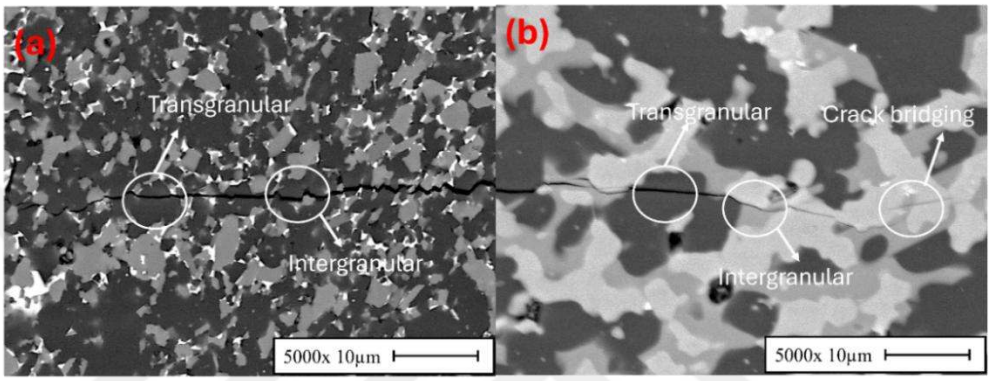

Figure 3.87. *Representative backscattered SEM images taken from polished surface of crack propagation of ATZ-5Sm sample, (a) SPS sintered sample, (b) GPS sintered sample*

In fig. 3.88, the darkest areas were Al_2O_3 matrix, medium-bright grains were TiC and the brightest phases were $SmAlO_3$. Excessive grain growth of Al_2O_3 grains was observed in the structure. Sm_2O_3 added to the composition reacted with Al_2O_3 to form the $SmAlO_3$ perovskite phase.

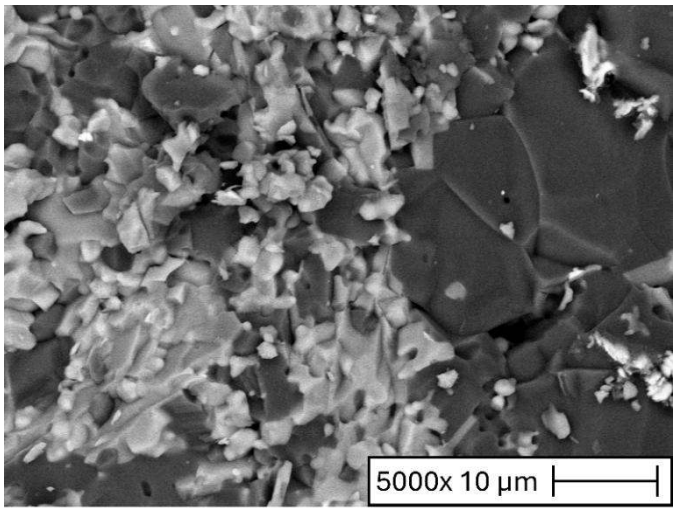

Figure 3.88. *Representative backscattered SEM image taken from the fractured surface of ATZ-3.5Sm*

3.6.5. CeO_2 additives

Samples were produced using different sintering methods by adding 3.5 wt.% and 5 wt.% CeO_2 to the ATZ composition and the effects of these methods on the material properties were compared. Sintering processes were carried out using three different methods: SPS, GPS with a carbon sheet and GPS without a carbon sheet. The densities of the obtained samples were analyzed in detail, their mechanical properties were evaluated and microstructural studies were carried out.

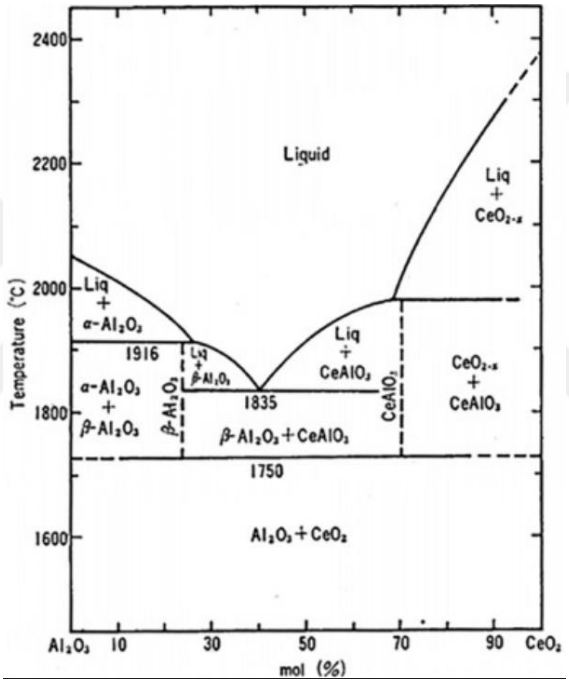

Figure 3.89. *Representative phase diagram of Al_2O_3-CeO_2. (Chang, et al., 2024)*

Studies conducted by Bilgiç (Bilgiç, 2012) reported that when CeO_2 was added to the Al_2O_3 matrix, the $CeAlO_3$ phase was formed, leaving porosity in surface contact with Al_2O_3. In this study, the formation of $CeAlO_3$ phase in ATZ composition and the effect of this phase on mechanical properties were evaluated by XRD, SEM and mechanical tests.

The SPS method was used to understand the sintering behavior of ATZ-3.5Ce composition. SPS provides important information about the sintering behavior of the material, as it provides densification at high temperature and in a short time. The

shrinkage behavior of the sample was followed by the displacement curve and the critical temperatures for the sintering process were determined during the SPS sintering process.

According to fig. 3.90, the temperature at which the displacement curve starts to increase (Tshr) was determined as 1310 °C for ATZ-3.5Ce. This temperature represents the threshold at which the pores of the sample begin to close and the material enters the densification process. The temperature at which the displacement curve remains constant (Tsin) was measured as 1535 °C. This temperature represents the point at which the sample reaches the closest level to full density and the material completes the sintering process. Predetermined parameters were used for the GPS sintering study. Sintering was performed with the same parameters with and without a carbon sheet.

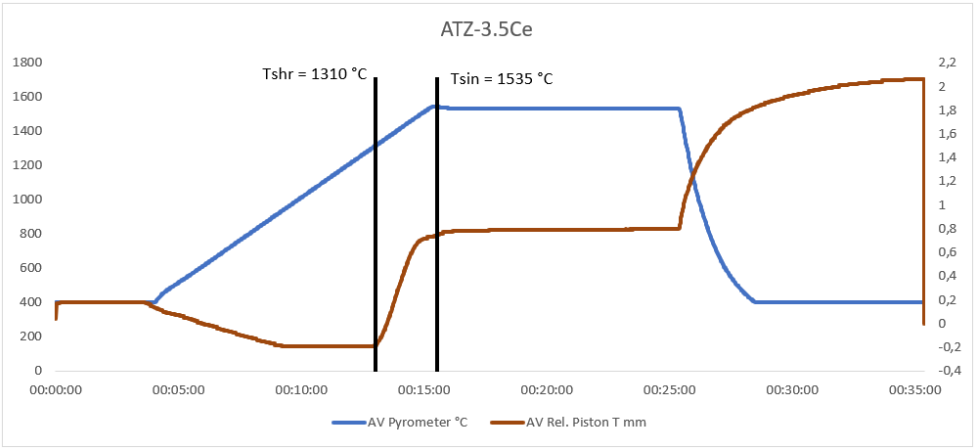

Figure 3.90. *Representative SPS graphic of ATZ-3.5Ce composition*

Table 3.31 shows the relative density (%) values of samples of ATZ-3.5Ce composition produced by three different sintering methods. The sample sintered with the SPS method achieved the highest density by reaching 99.39% relative density. This shows that SPS minimizes porosity by sintering the material quickly and effectively under the influence of high temperature and electrical current. The relative density of the sample sintered with the GPS – carbon sheet was 95.91%. This shows that carbon sheets have a negative effect on the sintering process. The carbon sheet prevented full densification during sintering due to oxygen limitation and increased the porosity level of the sample. The sample sintered with the GPS method without a carbon sheet reached a relative density of 97.55% and a more successful sintering process than the GPS method with a carbon sheet. The sintering atmosphere was more stable and the material was densified more homogeneously when carbon sheet was not used. However, since the GPS method

took longer and under lower pressure than SPS, it could not achieve a density as high as SPS.

Table 3.31. *Sintering methods and relative densities of ATZ-3.5Ce composition*

Sintering Method	Relative Density (%)
SPS	99.39
GPS – Carbon Sheet	95.91
GPS	97.55

Fig. 3.91 compares the backscattered SEM images of ATZ-3.5Ce composition obtained with different sintering methods at 5000x magnification. Fig. 3.91.a shows the image of the SPS sintered sample with the lowest porosity. The additive could not be sufficiently distributed within the structure and formed clusters due to the speed of the SPS method. Fig. 3.91.b shows the image of the sample sintered with the GPS with a carbon sheet, showing high porosity and phase separation. Pores formed at the grain boundaries and a homogeneous structure could not be obtained since the carbon sheet could not fully densify during the sintering process. Fig. 3.91.c shows that the image of the sample sintered with the GPS method without carbon sheet has a better microstructure than fig. 3.91.b. Less porosity was formed at grain boundaries, but certain irregularities in the phase distribution were observed.

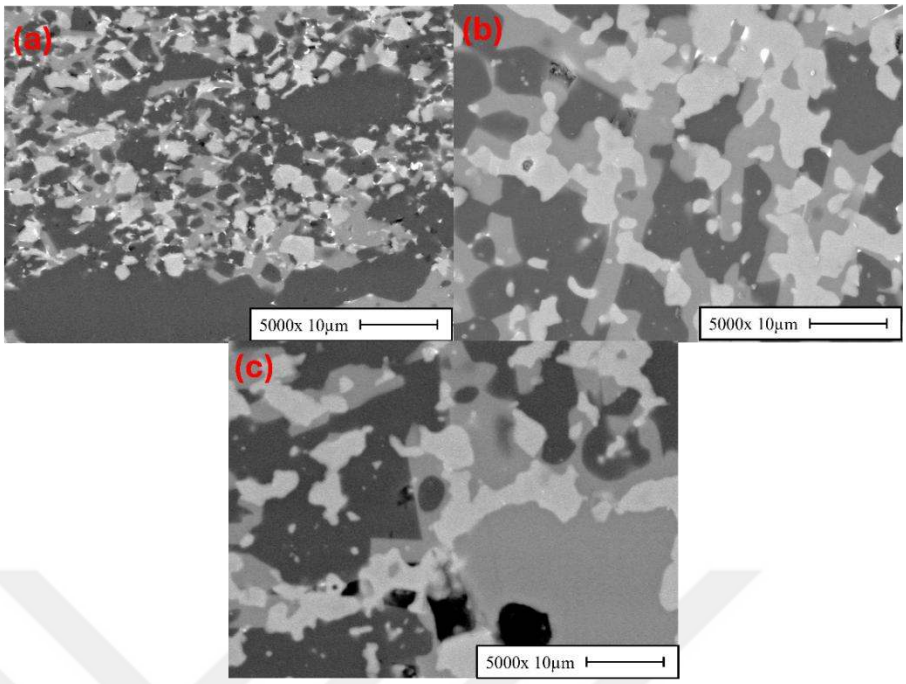

Figure 3.91. *Representative backscattered SEM images taken from polished surface of ATZ-3.5Ce sintered using different methods. (a) SPS, (b) GPS with carbon sheet and (c) GPS without carbon sheet*

Fig. 3.92 shows the XRD analysis, comparing the composition of ATZ-3.5Ce with the composition of ATZ. The ATZ composition (orange curve) consists of the main phases Al_2O_3, TiC and ZrO_2. Some peaks belonging to the carbon (C) phases were also observed, which were related to the carbon sheet or TiC content used in the sintering process.

The ATZ-3.5Ce composition (gray curve) reveals how the CeO_2 addition changes the material's structure. XRD shows that CeO_2 doping reacts with Al_2O_3 forming the $CeAlO_3$ phase. This phase may contribute to stabilizing the microstructure and potentially improving mechanical properties by providing a new oxide contribution to the ATZ composition. It was seen that the new peak belonging to the $CeAlO_3$ phase appears clearly in the ATZ-3.5Ce composition. Besides, other main phases (Al_2O_3, TiC and ZrO_2) in the ATZ composition remained intact, indicating that the overall structure of the material did not change significantly. However, the additive modified the matrix by forming a new phase.

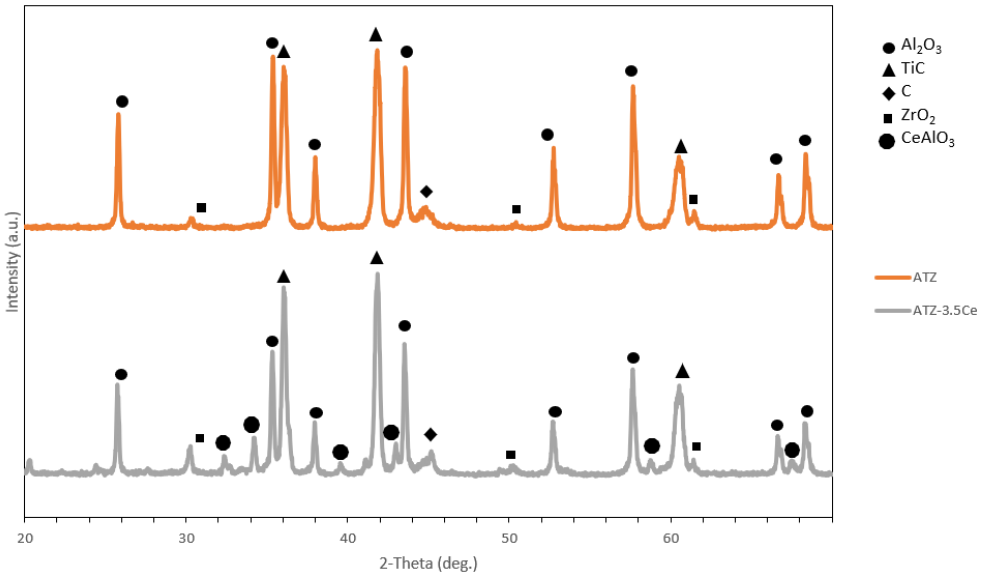

Figure 3.92. *Representative comparison of the XRD spectra of ATZ and ATZ-3.5Ce*

Fig. 3.93 shows the EDS analysis of the ATZ-3.5Ce composition in backscattered mode at 1250x magnification. According to the analysis results, the main components of the composition were Al_2O_3, TiC, and ZrO2 with oxygen (O), which was the highest with a 45.44 wt.%. This confirms that the ATZ matrix was largely Al_2O_3 based. Aluminum (Al) was detected with 29.60 wt.% and titanium (Ti) was detected with 15.06 wt.%. It supports the existence of Al_2O_3 and TiC phases in the ATZ structure. Zirconium (Zr) was detected with 1.87 wt.% indicating the presence of ZrO_2 added to the ATZ composition.

This analysis detected a cerium (Ce) element with 1.55 wt.%. This ratio shows that the CeO_2 contribution in the material after the sintering process was successfully incorporated into the composition and supported the formation of the $CeAlO_3$ phase observed in the XRD analysis. The carbon (C) content was determined to be 6.48 wt.% due to the TiC content and possible carbon residues used in the sintering process.

Element	Weight%	Atomic%
C	6,48	11,18
O	45,44	58,90
Al	29,60	22,75
Ti	15,06	6,52
Zr	1,87	0,43
Ce	1,55	0,23

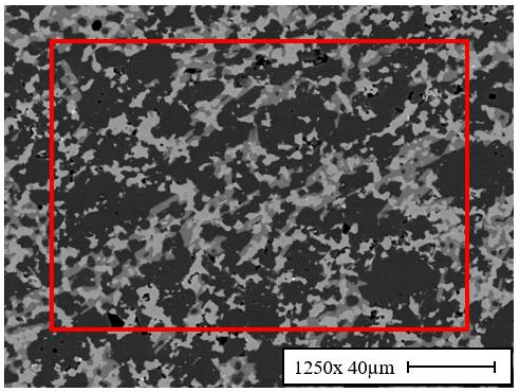

Figure 3.93. *Representative backscattered SEM image and EDS analysis taken from the polished surface of ATZ-3.5Ce*

Table 3.32 compares the mechanical properties (hardness and fracture toughness) of samples of ATZ-3.5Ce composition produced with different sintering methods. Mechanical tests were not performed since the relative density of the sample sintered with the carbon sheet GPS was low.

Table 3.32. *Mechanical properties of ATZ-3.5Ce compositions*

Sintering Method	Hardness (GPa)	Fracture Toughness (MPa $m^{1/2}$)
SPS	18.30	4.77
GPS	16.98	4.58

The hardness of the sample sintered with SPS was measured as 18.30 GPa. However, the fracture toughness of the sample sintered with SPS was measured as 4.77 MPa $m^{1/2}$, which was lower than the sample sintered with the GPS method. The sample sintered with the GPS method reached 16.98 GPa hardness and 4.58 MPa $m^{1/2}$ fracture toughness values. The higher hardness of the sample sintered with GPS can be explained by the longer sintering process and more stable phase formations. The higher fracture toughness indicates that better grain bonding may have been achieved during the GPS sintering. The $CeAlO_3$ phase formed by CeO_2 doping may have improved these mechanical properties.

Fig. 3.94 shows the backscattered SEM images comparing the crack propagation mechanism in SPS and GPS sintered samples of ATZ-3.5Ce composition. Fig. 3.94.a represents the sample sintered with the SPS method and fig. 3.94.b represents the sample sintered with the GPS method. Transgranular and intergranular crack propagation mechanisms were observed in both samples.

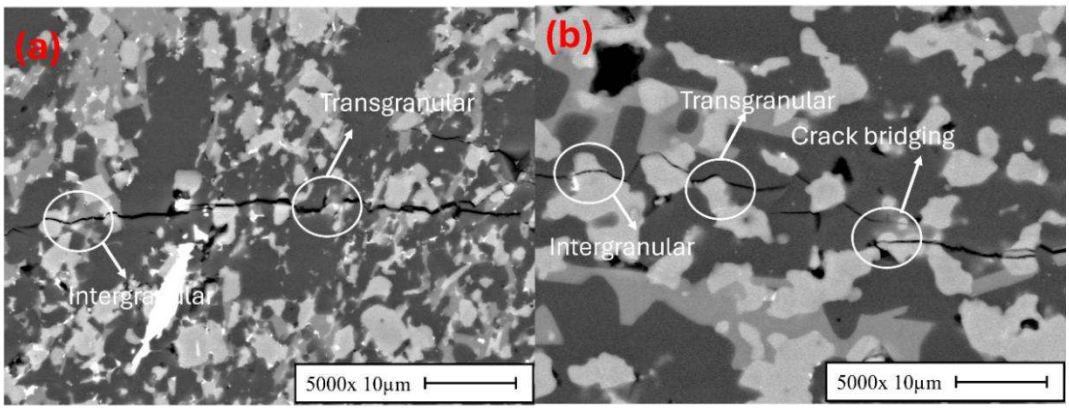

Figure 3.94. *Representative backscattered SEM images taken from polished surface of crack propagation of ATZ-3.5Ce sample, (a) SPS sintered sample, (b) GPS sintered sample*

The SPS method was used to understand the sintering behavior of ATZ-5Ce composition. SPS provides important information about the sintering behavior of the material, as it provides densification at high temperature and in a short time. The shrinkage behavior of the sample was followed by the displacement curve and the critical temperatures for the sintering process were determined during the SPS sintering process.

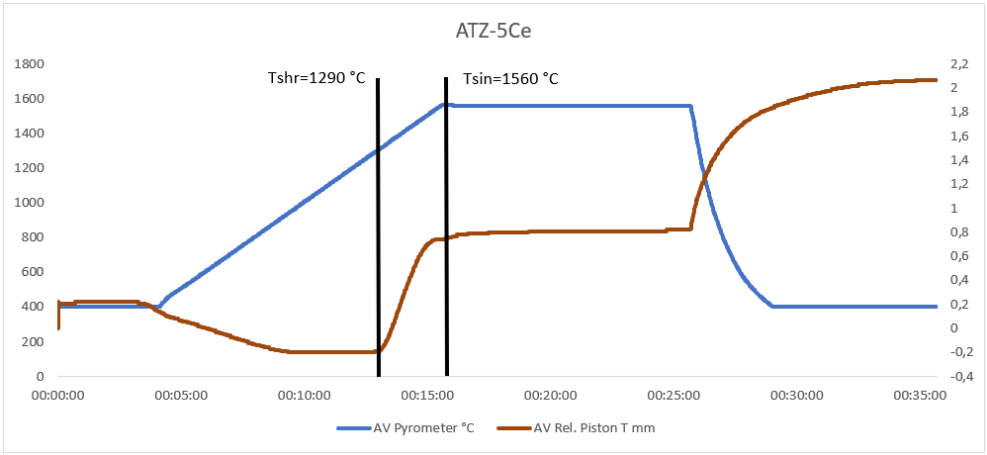

Figure 3.95. *Representative SPS graphic of ATZ-5Ce composition*

According to Fig. 3.95, the temperature at which the displacement curve starts to increase (Tshr) was determined as 1290 °C for ATZ-5Ce. This temperature represents the threshold at which the pores of the sample begin to close and the material enters the densification process. The temperature at which the displacement curve remains constant (Tsin) was measured as 1560 °C. This temperature represents the point at which the

sample reaches the closest level to full density and the material completes the sintering process. Predetermined parameters were used for the GPS sintering study. Sintering was performed with the same parameters with and without a carbon sheet.

Table 3.33 shows the relative density (%) values of samples of ATZ-5Ce composition produced by three different sintering methods. The sample sintered with the SPS method achieved the highest density by reaching 99.12% relative density. This shows that SPS minimizes porosity by sintering the material quickly and effectively under the influence of high temperature and electrical current. The relative density of the sample sintered with the GPS – carbon sheet was 95.55%. This shows that carbon sheets have a negative effect on the sintering process. The carbon sheet prevented full densification during sintering due to oxygen limitation and increased the porosity level of the sample. The sample sintered with the GPS method without a carbon sheet reached a relative density of 96.60% and a more successful sintering process than the GPS method with a carbon sheet. The sintering atmosphere was more stable and the material was densified more homogeneously when carbon sheet was not used. However, since the GPS method took longer and under lower pressure than SPS, it could not achieve a density as high as SPS.

Table 3.33. *Sintering methods and relative densities of ATZ-5Ce composition*

Sintering Method	Relative Density (%)
SPS	99.12
GPS – Carbon Sheet	95.55
GPS	96.60

Fig. 3.96 compares the backscattered SEM images of ATZ-5Ce composition obtained with different sintering methods at 5000x magnification. Fig. 3.96.a shows the image of the SPS sintered sample with the lowest porosity. The additive could not be sufficiently distributed within the structure and formed clusters due to the speed of the SPS method. Fig. 3.96.b shows the image of the sample sintered with the GPS with a carbon sheet showing high porosity and phase separation. Pores formed at the grain boundaries and a homogeneous structure could not be obtained since the carbon sheet could not fully densify during the sintering process. Fig. 3.96.c shows that the image of the sample sintered with the GPS method without carbon sheet has a better microstructure

than fig. 3.96.b. Less porosity was formed at grain boundaries but certain irregularities in the phase distribution were observed.

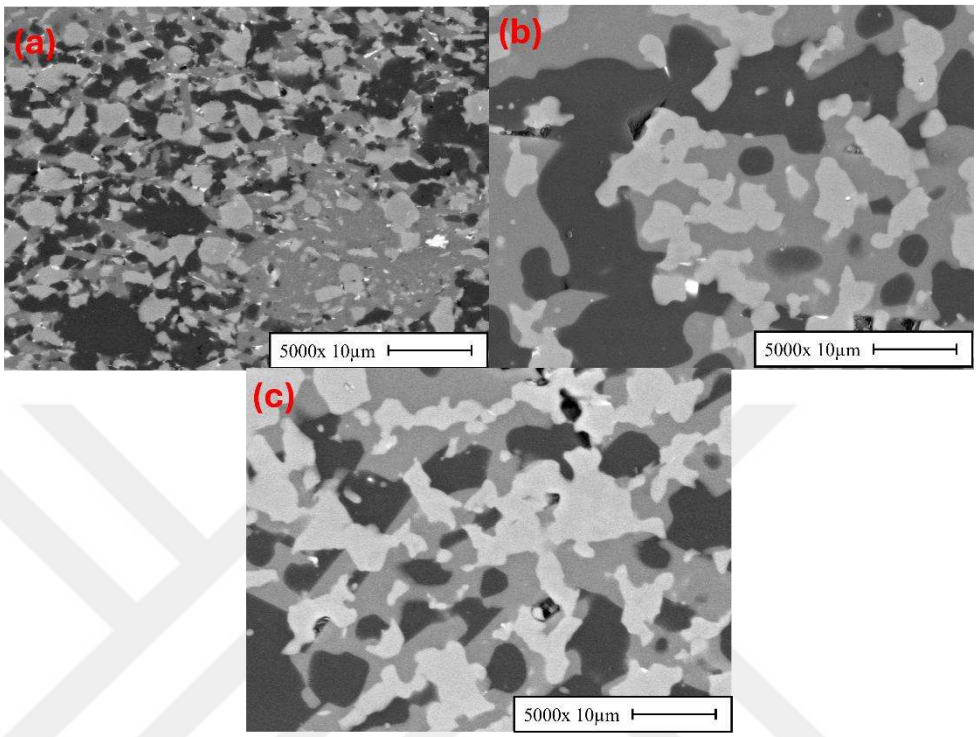

Figure 3.96. *Representative backscattered SEM images taken from polished surface of ATZ-5Ce sintered using different methods. (a) SPS, (b) GPS with carbon sheet and (c) GPS without carbon sheet*

Fig. 3.97 shows the EDS analysis of the ATZ-5Ce composition in backscattered mode at 1250x magnification. According to the analysis results, the main components of the composition were Al_2O_3, TiC, ZrO_2 with oxygen (O), which was the highest with a 43.02 wt.%. This confirms that the ATZ matrix was largely Al_2O_3 based. Aluminum (Al) was detected with 26.19 wt.% and titanium (Ti) was detected with 19.91 wt.%. It supports the existence of Al_2O_3 and TiC phases in the ATZ structure. Zirconium (Zr) was detected with 1.59 wt.% indicating the presence of ZrO_2 added to the ATZ composition.

This analysis detected cerium (Ce) element with 2.91 wt.%. This ratio shows that the CeO_2 contribution in the material after the sintering process was successfully incorporated into the composition and supported the formation of the $CeAlO_3$ phase observed in the XRD analysis. The carbon (C) content was determined to be 6.38 wt.% due to the TiC content and possible carbon residues used in the sintering process.

Element	Weight%	Atomic%
C	6,38	11,44
O	43,02	57,89
Al	26,19	20,90
Ti	19,91	8,95
Zr	1,59	0,38
Ce	2,91	0,45

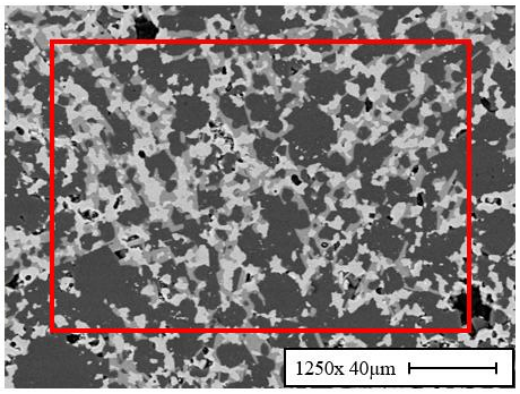

Figure 3.97. *Representative backscattered SEM image and EDS analysis taken from the polished surface of ATZ-5Ce*

Table 3.34 compares the mechanical properties (hardness and fracture toughness) of samples of ATZ-5Ce composition produced with different sintering methods. Mechanical tests were not performed since the relative density of the sample sintered with the carbon sheet GPS was low.

Table 3.34. *Mechanical properties of ATZ-5Ce compositions*

Sintering Method	Hardness (GPa)	Fracture Toughness (MPa $m^{1/2}$)
SPS	17.70	4.95
GPS	16.20	5.5

The hardness of the sample sintered with SPS was measured as 17.70 GPa. However, the fracture toughness of the sample sintered with SPS was measured as 4.95 MPa $m^{1/2}$, which was lower than the sample sintered with the GPS method. The sample sintered with the GPS method reached 16.20 GPa hardness and 5.50 MPa $m^{1/2}$ fracture toughness values. The higher hardness of the sample sintered with GPS can be explained by the longer sintering process and more stable phase formations. The higher fracture toughness indicates that better grain bonding may have been achieved during the GPS sintering. The $CeAlO_3$ phase formed by CeO_2 doping may have improved these mechanical properties.

Fig. 3.98 shows the backscattered SEM images comparing the crack propagation mechanism in SPS and GPS sintered samples of ATZ-5Ce composition. Fig. 3.98.a represents the sample sintered with the SPS method and fig. 3.98.b represents the sample sintered with the GPS method. Transgranular and intergranular crack propagation mechanisms were observed in both samples.

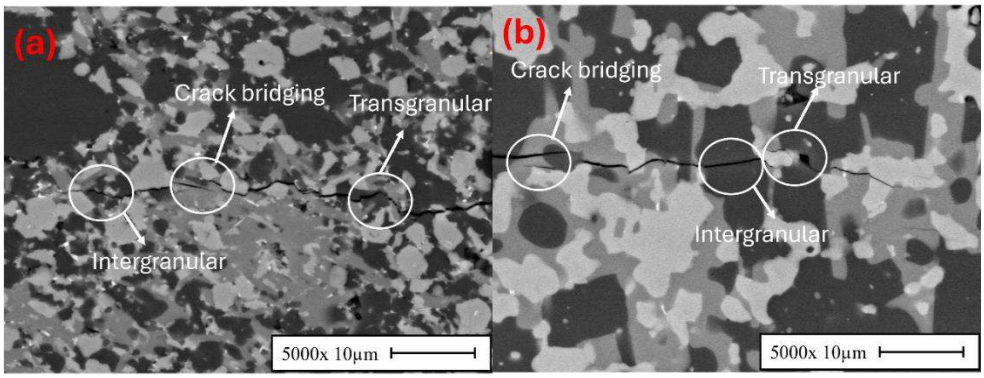

Figure 3.98. *Representative backscattered SEM images taken from polished surface of crack propagation of ATZ-5Ce sample, (a) SPS sintered sample, (b) GPS sintered sample*

In fig. 3.99, the darkest areas correspond to Al_2O_3 matrix, medium-bright grains correspond to TiC and the brightest phase often seen at grain boundaries corresponds to $CeAlO_3$. Ce in the system reacts with Al_2O_3 to form the perovskite phase $CeAlO_3$. The segregation of this phase at boundaries suppressed Al_2O_3/TiC grain growth during GPS at 1900 °C.

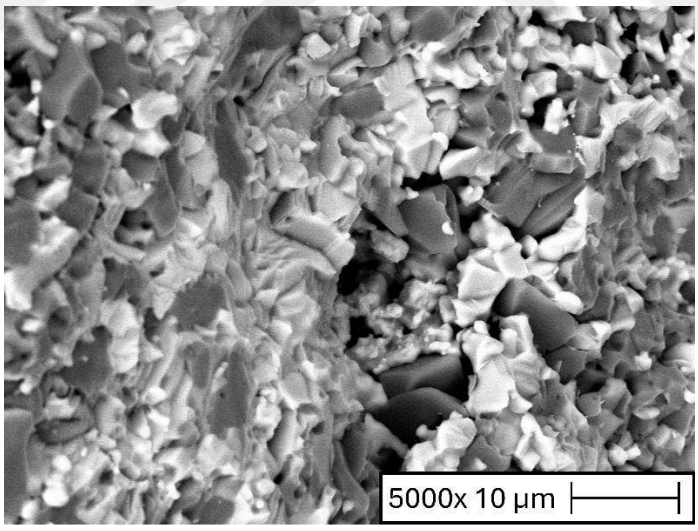

Figure 3.99. *Representative backscattered SEM image taken from the fractured surface of ATZ-3.5Ce*

3.6.6. Comparison of REOs additives

Table 3.35 shows the Tshr, Tsin and ΔT values obtained in the SPS process of the ATZ samples which contain rare earth oxides (Er_2O_3, Yb_2O_3, Y_2O_3, Sm_2O_3, CeO_2) at 3.5

and 5 wt.%. These parameters were important for evaluating the thermal behavior during the sintering process and the effects of additives on the sintering kinetics.

ATZ-Y and ATZ-Yb compositions generally exhibit the highest Tshr and Tsin temperatures. Especially, the ATZ-5Y composition has the highest Tshr value at 1370 °C. This shows that Y_2O_3 and Yb_2O_3 additives initiate the sintering process in the Al_2O_3 matrix at higher temperatures. ATZ-Ce has the lowest Tshr and Tsin temperatures. These additives have a transient liquid phase effect that can initiate sintering at low temperatures. The Tshr value of the ATZ-5Ce occurred at 1290 °C. This shows that the CeO_2 addition accelerates the sintering process and pulls the beginning of the sintering to lower temperatures. ATZ-Sm compositions also show a similar trend to ATZ-Ce. The Tsin value of the ATZ-5Sm was 1570 °C, one of the lowest sintering temperatures among all compositions.

The widest ΔT was observed at 310 °C for the ATZ-5Yb composition. It shows that ATZ-Yb composition continues to densify over a wide temperature range and the sintering mechanism proceeds more gradually. ATZ-Ce compositions have the lowest ΔT (225 °C and 270 °C). This indicates that ATZ-Ce completed the sintering process in a narrower temperature range and faster shrinkage occurred. ATZ-Sm compositions also exhibit relatively low ΔT values. In ATZ-Y composition, an increasing additive ratio decreases ΔT. The ΔT value of ATZ-3.5Y, which was 290 °C, decreased to 270 °C in ATZ-5Y.

As a result, ATZ-Y and ATZ-Yb compositions require higher sintering temperatures but have a wider range. ATZ-Ce and ATZ-Sm can densify at lower sintering temperatures, but the sintering process occurs in a narrower temperature range. Regarding ΔT values, the widest sintering window was observed in the ATZ-Yb composition, while the narrowest sintering window was observed in the ATZ-Ce composition.

Table 3.35. *Tshr, Tsin and ΔT values of REOs added compositions*

Compositions	Tshr (°C)	Tsin (°C)	ΔT (°C)
ATZ-3.5Er	1320	1610	290
ATZ-5Er	1330	1630	300
ATZ-3.5Yb	1350	1650	300
ATZ-5Yb	1330	1640	310
ATZ-3.5Y	1350	1640	290
ATZ-5Y	1370	1640	270
ATZ-3.5Sm	1310	1580	270
ATZ-5Sm	1315	1570	255
ATZ-3.5Ce	1310	1535	225
ATZ-5Ce	1290	1560	270

Table 3.36 compares the relative densities of samples with different weight ratios of rare earth oxides (Er_2O_3, Yb_2O_3, Y_2O_3, Sm_2O_3, CeO_2) added to the ATZ composition by three different sintering methods. The relative density values of the samples produced with SPS, GPS and GPS with carbon sheets were evaluated and the effects of the sintering method and additive on the density were analyzed.

Compositions sintered with the SPS method reached the highest relative density values among all compositions (>98.13%). Especially the composition with Yb_2O_3 additives reached the highest densities. The lowest SPS density belongs th the ATZ-5Y compositions (98.14%). All compositions sintered with the SPS method generally have density values above 98%.

The densities of the compositions sintered with the GPS were lower than those of SPS sintered but higher than the GPS with a carbon sheet. While the ATZ-3.5Yb composition had the highest relative density of 98.32%, the ATZ-5Y composition showed the lowest relative density of 96.16%. It was observed that compositions with Y_2O_3 additives had lower densities in the GPS method. ATZ-Er and ATZ-Ce compositions reached relatively high densities.

All compositions sintered using carbon sheet have the lowest density values. The ATZ-5Y sample had the lowest density with 90.24%. This indicates that the oxygen limiting effect of the carbon sheet causes more porosity in compositions containing Y_2O_3. ATZ-3.5Yb (95.91%) and ATZ-3.5Ce (95.91%) were the highest relative densities.

Table 3.36. *Relative densities of sintered compositions with SPS, GPS and GPS with carbon sheet.*

	Relative Density (%)		
Compositions	**SPS**	**GPS**	**GPS with a carbon sheet**
ATZ-3.5Er	99.95	97.69	95.64
ATZ-5Er	99.97	96.95	94.06
ATZ-3.5Yb	99.99	98.32	95.91
ATZ-5Yb	99.96	97.90	94.86
ATZ-3.5Y	98.90	97.09	94.57
ATZ-5Y	98.14	96.16	90.24
ATZ-3.5Sm	99.56	96.68	95.33
ATZ-5Sm	99.21	95.92	95.18
ATZ-3.5Ce	99.39	97.55	95.91
ATZ-5Ce	99.12	96.60	95.55

Fig. 3.100 compares the microstructural differences of compositions sintered with SPS (left column) and GPS (right column) containing 3.5 wt.% REOs. Fig. 3.100.a and fig. 3.100.b show ATZ-3.5Er, fig. 3.100.c and fig. 3.100.d show ATZ-3.5Yb, fig. 3.100.e and fig. 3.100.f show ATZ-3.5Y, fig. 3.100.g and fig. 3.100.h show ATZ-3.5Sm and fig. 3.100.i and fig. 3.100.j show ATZ-3.5Ce composition. Compositions sintered with the SPS had a more homogeneous structure, while compositions sintered with GPS showed significant porosity and grain growth. It was observed that the grains become larger and intergranular porosities were more in compositions sintered with GPS, while the compositions sintered with SPS consist of smaller grains.

Better densification was achieved with SPS, especially in ATZ-3.5Er (fig. 3.100.a) and ATZ-3.5Yb (fig. 3.100.c). Pores and phase separation at the grain boundaries were evident in compositions (fig. 3.100.b and fig. 3.100.d) sintered with GPS. Grains grow in the ATZ-3.5Yb (fig. 3.100.d). However, it has a more homogeneous distribution compared to other compositions. A significant grain growth and pore formation were observed in the compositions ATZ-3.5Y (fig. 3.100.f). This shows that Y_2O_3 addition leads to more porosity during sintering with GPS.

Similar behaviors were observed in Sm_2O_3 and CeO_2 added compositions. There were larger grains and distinct pores in ATZ-3.5Sm (fig. 3.100.h) and ATZ-3.5Ce (fig. 3.100.j). In fig. 3.100.g and fig. 3.100.i have a denser structure. Phase separation and porosity were more noticeable in ATZ-3.5Ce (fig. 3.100.j).

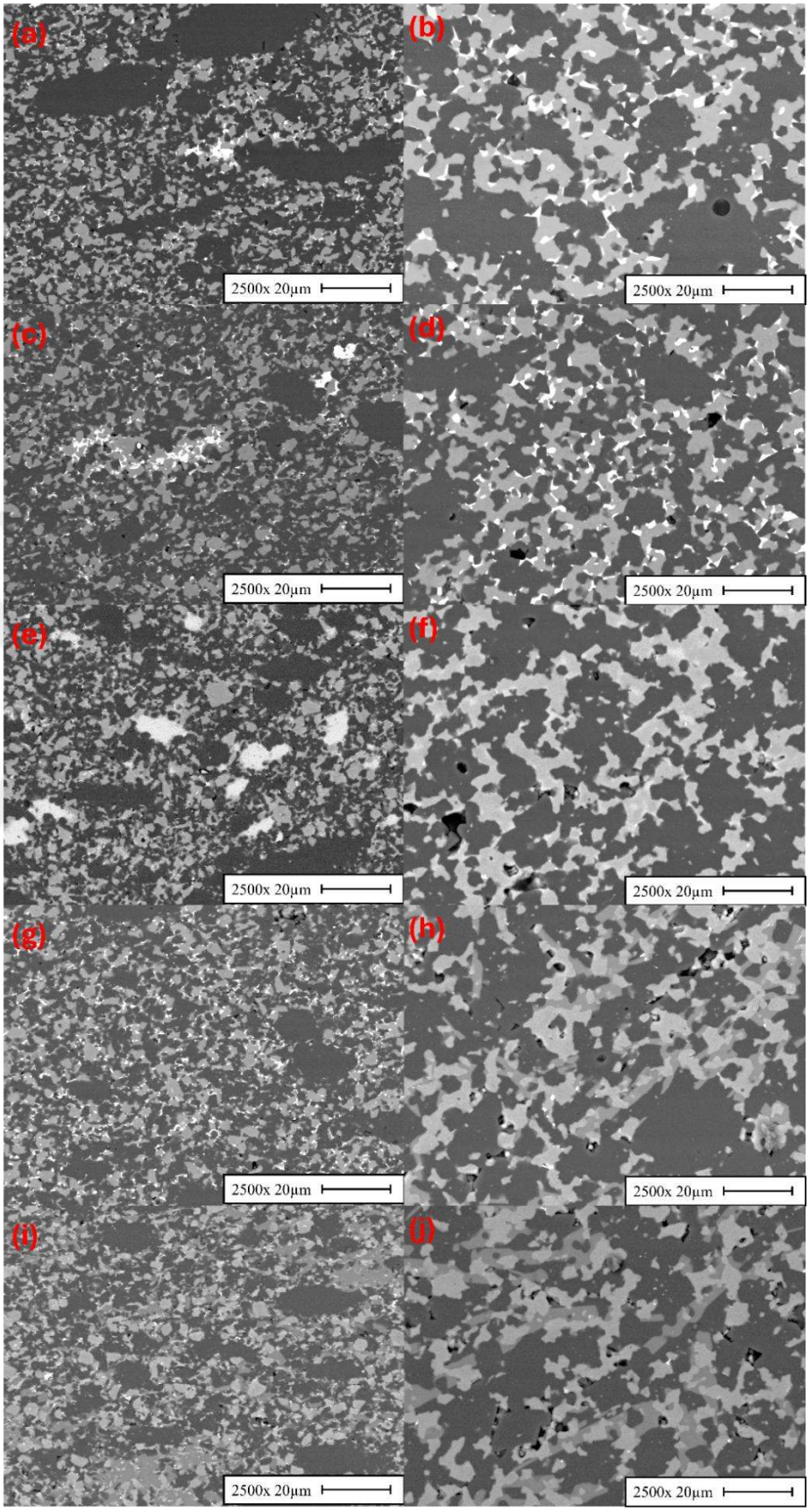

Figure 3.100. *Representative backscattered SEM images taken from polished surface of 3.5wt.% additive contained compositions. The left column shows SPS sintered samples and the right column shows GPS sintered samples.*

Fig. 3.101 compares the microstructural differences of compositions sintered with SPS (left column) and GPS (right column) containing 5 wt.% REOs. Fig. 3.101.a and fig. 3.101.b show ATZ-5Er, fig. 3.101.c and fig. 3.101.d show ATZ-5Yb, fig. 3.101.e and fig. 3.101.f show ATZ-5Y, fig. 3.101.g and fig. 3.101.h show ATZ-5Sm and fig. 3.101.i and fig. 3.101.j show ATZ-5Ce composition. Compositions sintered with the SPS had a more homogeneous structure, while compositions sintered with GPS showed significant porosity and grain growth. It was observed that the grains become larger and intergranular porosities were more in compositions sintered with GPS, while the compositions sintered with SPS consist of smaller grains.

It was seen that porosity was low in ATZ-5Er (fig. 3.101.a) and ATZ-5Yb (fig. 3.101.c), but the additive was not distributed homogeneously in the structure and formed agglomerations. On the other hand, in ATZ-5Er (fig. 3.101.b) and ATZ-5Yb (fig. 3.101.d) compositions the additive was more homogeneously distributed in the structure. Additionally, grain growth and porosity increased. In the ATZ-5Yb (fig. 3.101.d) composition, porosity at grain boundaries was more noticeable compared to ATZ-5Yb (fig. 3.101.c).

When fig. 3.100 was compared with fig. 3.101, the grain growth of the composition containing 5wt.% additive was more noticeable. Porosity increased in compositions sintered with GPS. Compositions sintered with SPS formed denser structures at both additive ratios. It has been noticed that grain growth increases slightly even in SPS compositions containing 5wt.% additive.

Meanwhile the intergranular porosities were less than 3.5wt.% composition sintered with GPS. These porosities increased in the 5wt.% composition. Especially, CeO_2 added ATZ-5Ce (fig. 3.101.j) composition (96.60%) contains more porosity than ATZ-3.5Ce (fig. 3.100.j) composition (97.55%).

This comparison shows that porosity increases in composition sintered with GPS as the additive amount increases. Even in the composition sintered with the SPS, it was observed that the grains grow slightly at the 5wt.% added composition, but still have lower porosity compared to the 5wt.% added composition sintered with GPS.

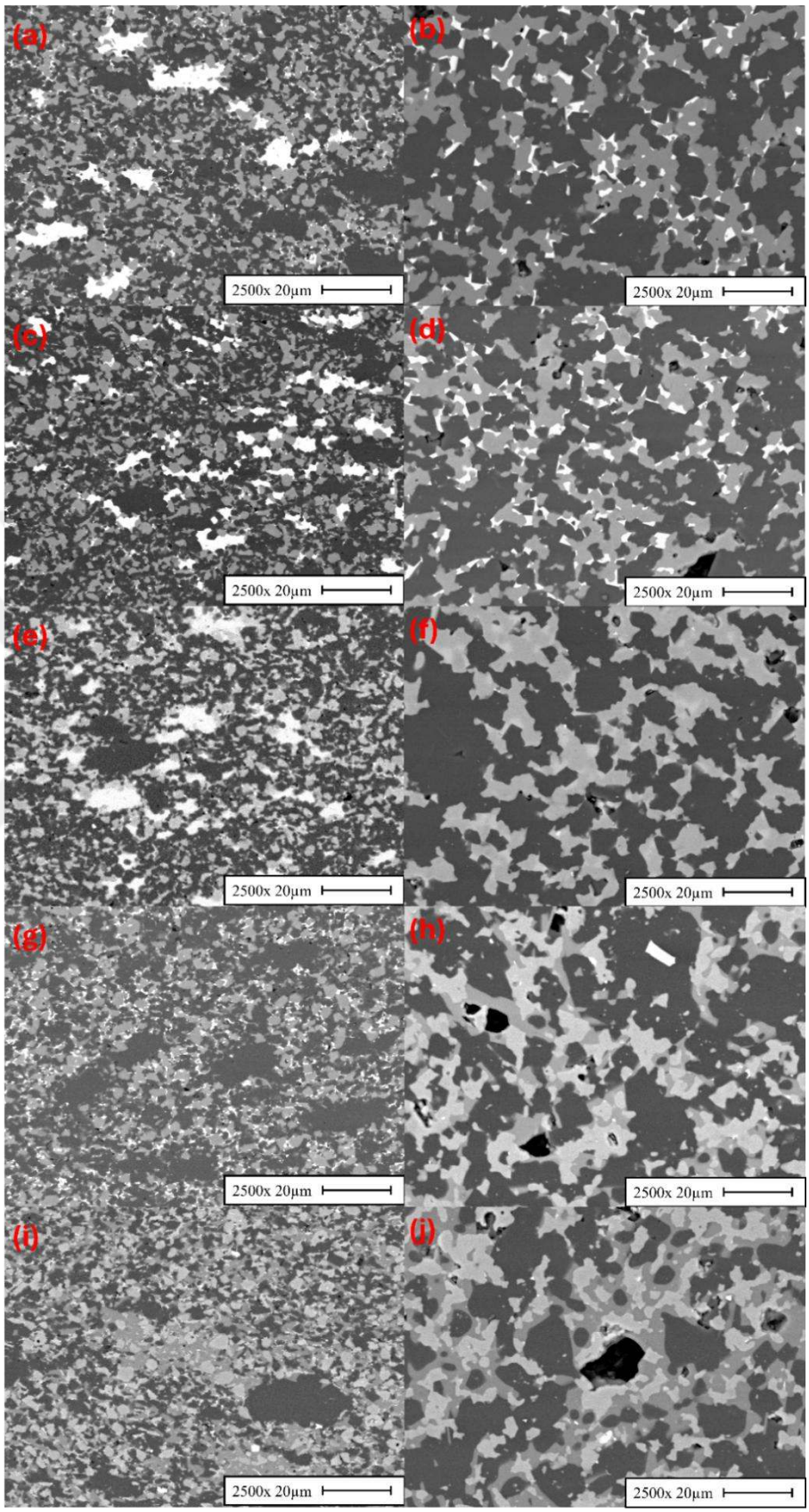

Figure 3.101. *Representative backscattered SEM images taken from polished surface of 5wt.% additive contained compositions. The left column shows the SPS sintered samples and the right column shows the GPS sintered samples.*

Fig. 3.102 presents the XRD results of the composites. No new phases were detected in the ATZ composite without additives which was consistent with studies in the literature. Garnet phases such as $Er_3Al_5O_{12}$, $Yb_3Al_5O_{12}$ and $Y_3Al_5O_{12}$ were formed in ATZ-3.5Er, ATZ-3.5Yb and ATZ-3.5Y (fig. 3.102.b-d-e) compositions and perovskite phases such as $CeAlO_3$ and $SmAlO_3$ were formed in ATZ-3.5Ce and ATZ-3.5Sm (fig. 3.102.c-f) compositions, respectively. Ionic radii play a crucial role in determining the formation of phases in rare earth oxide-doped ATZ composites. The ionic radius of a rare earth oxide influences its crystal structure and compatibility with the host ATZ matrix. Rare earth oxides with similar ionic radii such as ytterbium (0.985 Å), erbium (1.004 Å) and yttrium (1.019 Å), integrate into the lattice and lead to garnet phases. Larger ionic radii like samarium (1.079 Å) and cerium (1.143 Å) result in distinct perovskite phases. The stability of the perovskite structure was defined by the Goldschmidt Tolerance Factor (Guvenc, et al., 2025):

$$t = \frac{r_A + r_O}{\sqrt{2}(r_B + r_O)} \tag{3.1}$$

Where r_A is the radius of the A-site cation, r_B is the Radius of the B-site cation and r_O is the Radius of the O. According to this formula, the tolerance factor of the perovskite phase of ATZ-Ce is t_{Ce} = 0.927 and ATZ-Sm is t_{Sm} = 0.905. Results were in the stable perovskite range (0.8-1.0). (Tiwar, Gergardt and Szutkowska, 2016)

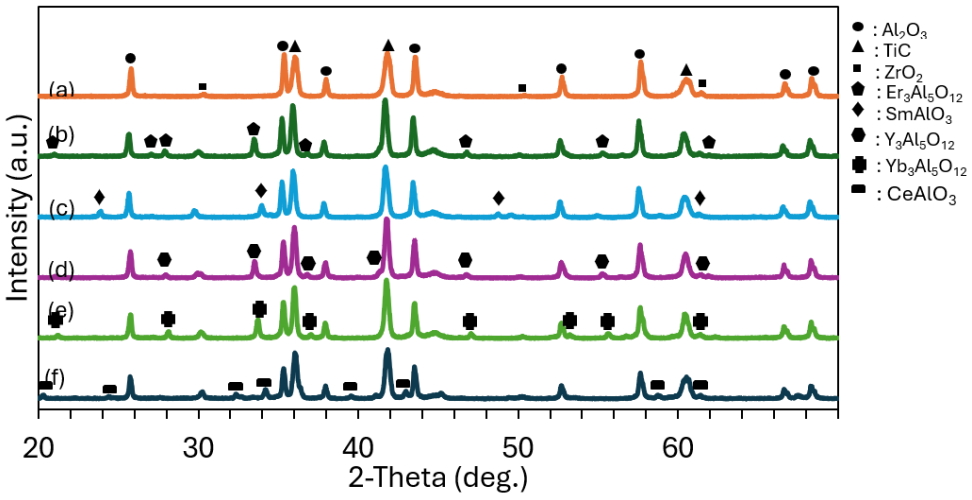

Figure 3.102. *Representative XRD analysis of the 3.5 wt.% compositions. ATZ (a), ATZ-3.5Er (b), ATZ-3.5Sm (c), ATZ-3.5Y (d), ATZ-3.5Yb (e) and ATZ-3.5Ce (f)*

When the hardness values of ATZ-3.5wt.%REOs compositions were examined, the compositions sintered with the SPS have higher hardness than those sintered with GPS. While ATZ-3.5Er (GPS) reaches the highest hardness value (~21 GPa), the ATZ-3.5Ce (GPS) has the lowest hardness value (~16.5 GPa). ATZ-3.5Y (SPS) and ATZ-3.5Ce (SPS) have a medium hardness (~18-19 GPa) while ATZ-3.5Er (SPS) has the lowest hardness (~17 GPa) among the compositions sintered with the SPS. Compositions sintered with GPS generally showed lower hardness and the porosity and grain growth negatively affected the mechanical properties.

Although similar trends were observed in ATZ-5wt.%REOs, some differences in hardness were noteworthy. The ATZ-5Yb (GPS) has the lowest hardness (~16 GPa), while the ATZ-5Er (GPS) again reaches the highest hardness (~21 GPa). ATZ-5Yb (SPS) and ATZ-5Sm (SPS) have the medium hardness (~18-19 GPa) while ATZ-5Er (SPS) has the lowest hardness (~17 GPa). The noteworthy point was that the hardness values in some compositions decrease as the amount of the additive increases.

When two graphics were compared, it was seen that the 3.5wt.% compositions generally have higher hardness than the 5wt.% compositions. Especially in compositions sintered with the GPS the hardness decreased significantly as the additive ratio increased. This is because high additive ratios cause the formation of larger grains and increased porosity at grain boundaries in some compositions. The hardness value difference between 3.5wt.% and 5wt.% was less in SPS sintered compositions, but 3.5wt.% compositions still have higher hardness. In general, SPS offers higher hardness than GPS, while keeping the additive ratio at the optimum level is critical for mechanical properties.

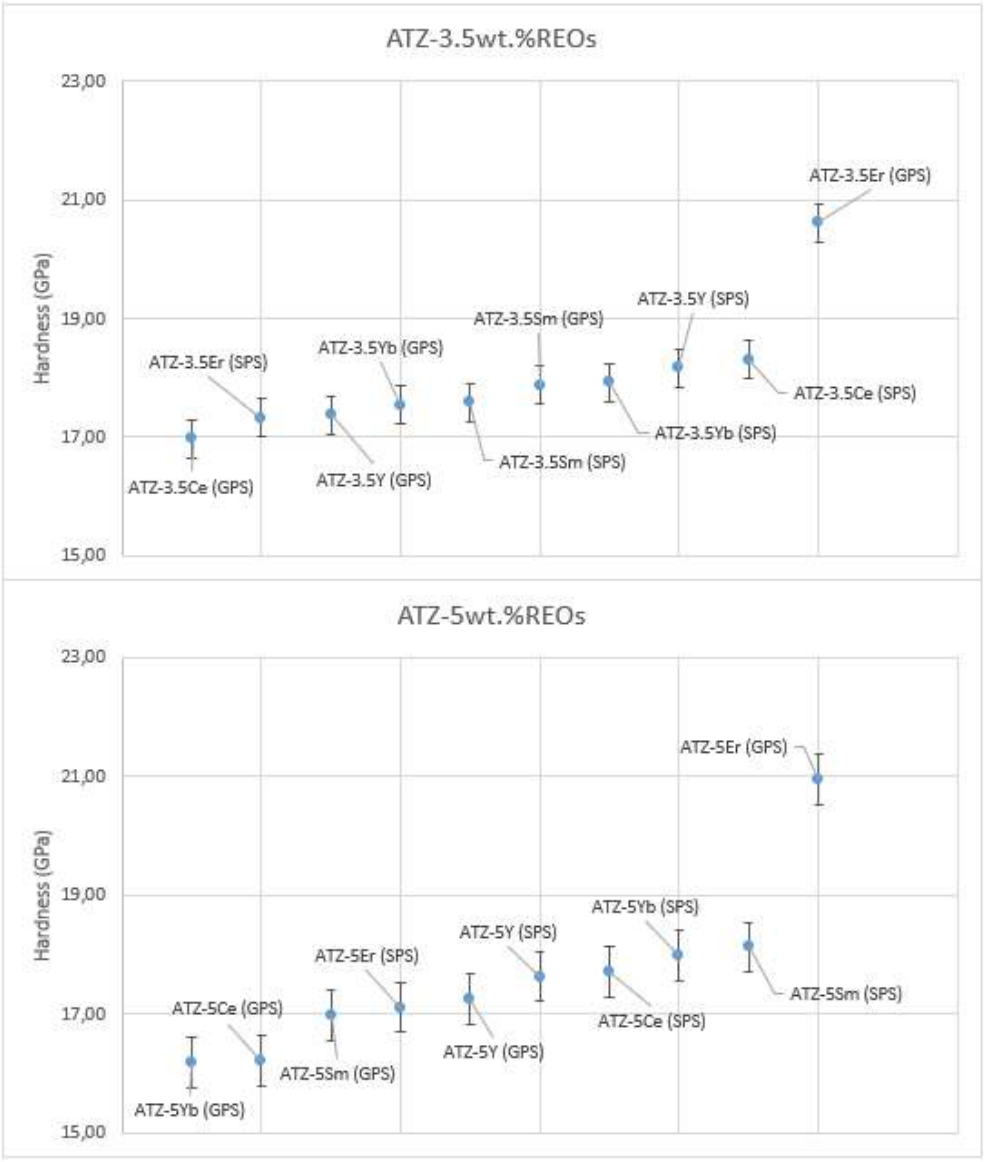

Figure 3.103. *Representative hardness comparison graphic of ATZ-3.5wt.%REOs and ATZ-5wt.%REOs sintered with SPS and GPS*

Fracture toughness comparison graph of ATZ-3.5wt.%REOs and ATZ-5wt.%REOs compositions was given in fig. 3.104. When the fracture toughness of ATZ-3.5wt.%REOs composites was examined, the compositions sintered with the GPS generally showed higher fracture toughness compared to SPS-sintered compositions. The ATZ-3.5Er (GPS) has the highest fracture toughness (~6.5 MPa $m^{1/2}$). In contrast, the ATZ-3.5Y (GPS) has the lowest fracture toughness (~3.5 MPa $m^{1/2}$). ATZ-3.5Ce (SPS) and ATZ-3.5Sm (SPS) exhibited a moderate fracture toughness (~4.5-5 MPa $m^{1/2}$) while ATZ-3.5Yb had the lowest fracture toughness (~4 MPa $m^{1/2}$). The high fracture toughness of GPS-sintered compositions was related to the mechanisms that slow down the crack

propagation due to the formation of second phases and microstructural arrangements at the grain boundaries.

Although similar trends were observed in ATZ-5wt.%REOs compositions, a significant increase in fracture toughness values was noted in some additives. The ATZ-5Ce (GPS) achieved the highest fracture toughness (~6.5 MPa $m^{1/2}$) followed by the ATZ-5Er (GPS) (~6 MPa $m^{1/2}$). For other additives, ATZ-5Yb (GPS) and ATZ-5Sm (GPS) remained at the moderate level (~4.5-5 MPa $m^{1/2}$) while ATZ-5Y (GPS) had the lowest fracture toughness (~3.5 MPa $m^{1/2}$). This difference was more noticeable in SPS-sintered compositions with ATZ-5Ce (SPS) and ATZ-5Sm (SPS) reaching relatively high fracture toughness (~5 MPa $m^{1/2}$) while ATZ-5Y (SPS) and ATZ-5Yb (SPS) have the lowest (~3.5-4 MPa $m^{1/2}$). This shows that the fracture toughness enhancing effects of CeO_2 and Er_2O_3 additives were more noticeable than other additives.

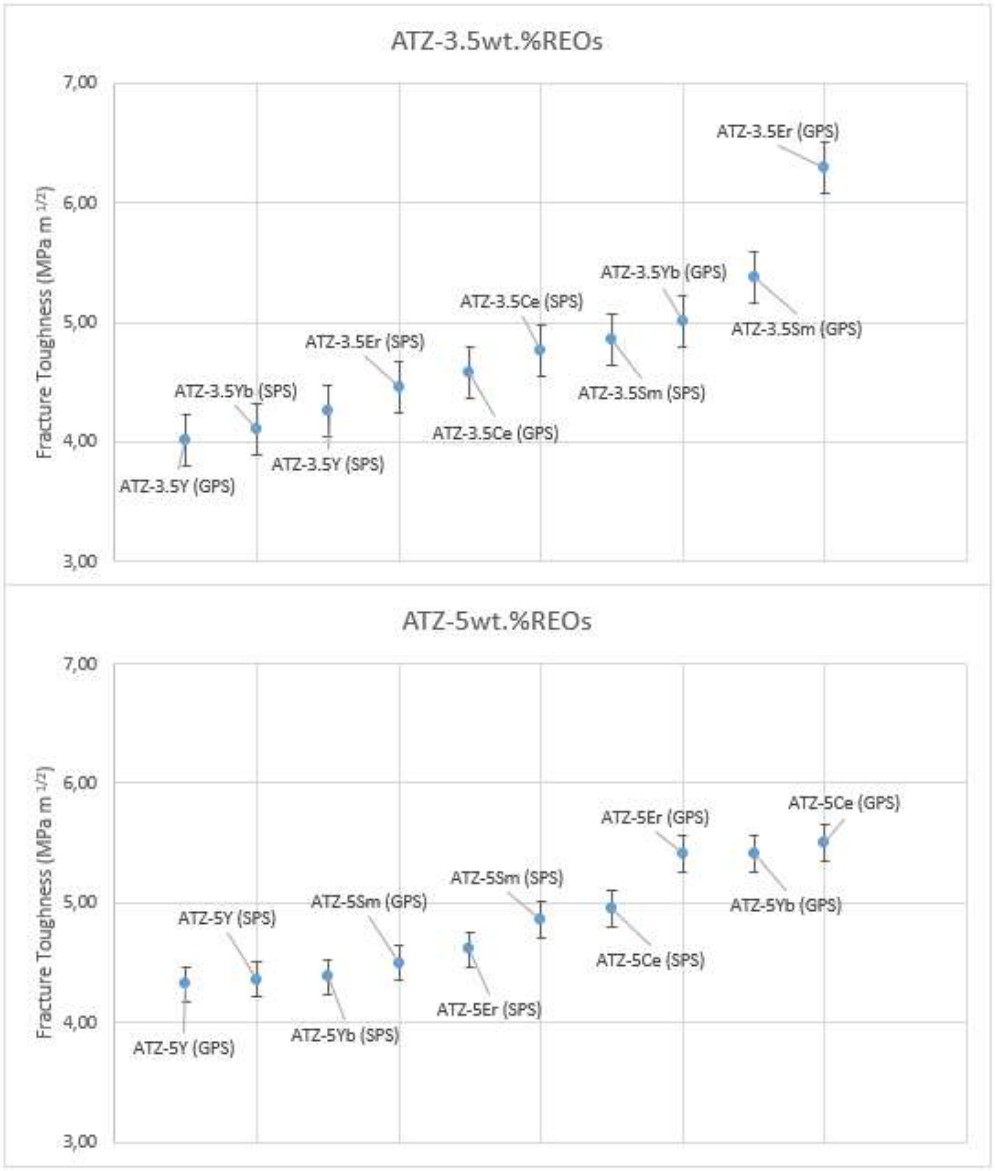

Figure 3.104. *Representative fracture toughness comparison graphic of ATZ-3.5wt.%REOs and ATZ-5wt.%REOs sintered with SPS and GPS*

When comparing two additive ratios, 5wt.% additive generally have higher fracture toughness than 3.5wt.% additive. The increase in the additive ratio significantly improved in fracture toughness especially in compositions containing CeO_2 and Er_2O_3. However, as the additive ratio increased the fracture toughness of compositions containing Y_2O_3 remained lower. This shows that the phase formation mechanism of Y_2O_3 and its effect on the Al_2O_3 matrix differ from other additives. SPS-sintering presents a lower fracture toughness, while the GPS-sintering provides higher fracture toughness for all additive ratios. In summary, Er_2O_3 and CeO_2 additives provided the best result regarding both

hardness and fracture toughness, while the effect of Y_2O_3 additives on improving mechanical properties was limited.

3.7. Granulated ATZ-5Er and ATZ-5Ce sintered with GPS

In the previous study, it was determined that the addition of 5wt% Er_2O_3 and CeO_2 to the ATZ composition improved the mechanical properties more than other additives. Taking this information as a reference, ATZ-5Er and ATZ-5Ce compositions were prepared in granule form. Then, the prepared granules were shaped by pressing and sintered with the GPS regime determined in the previous study. The compositions were compared by sintering at 1800 °C and then at 1900 °C. It was also investigated whether the positions of ATZ compositions in the graphite crucible influenced sintering.

3.7.1. 1800 °C GPS sintered ATZ, ATZ-5Er, ATZ-5Ce

Fig. 3.105 shows the positions of ATZ, ATZ-5Er and ATZ-5Ce compositions in the graphite crucible during sintering with GPS at 1800 °C. The ATZ, ATZ-5Er and ATZ-5Ce compositions were pressed at 192 MPa, 155 MPa and 228 MPa, respectively.

Figure 3.105. *Schematic representation of samples in a graphite crucible sintered at 1800 °C.*

In fig. 3.106 backscattered SEM images of compositions sintered at 1800 °C at 2500x magnification were given. Fig. 3.106.a shows the middle part of the ATZ, fig. 3.106.b shows the edge part of the ATZ, fig. 3.106.c shows the middle part of the ATZ-

5Er, fig. 3.106.d shows the edge part of the ATZ-5Er, fig. 3.106.e shows the middle part of the ATZ-5Ce and fig. 3.106.f shows the edge part of the ATZ-5Ce composition.

When fig. 3.106.a and fig. 3.106.b of the ATZ composition was examined and a relatively homogeneous microstructure was observed in the middle region, while a distinct boundary layer was formed in the edge regions. This boundary layer was related to the phase separation that occurs on the surface because of the effect of the sintering temperature. Additionally, the presence of some microcracks in the central region of the ATZ was noteworthy. This was caused by insufficient sintering temperature and press failure.

When fig. 3.106.c and fig. 3.106.d of the ATZ-5Er composition was examined and it was seen that the Er_2O_3 addition affects the microstructure significantly. The presence of phases with different morphologies accumulated on the surface during the sintering was observed in the edge region while the formation of the second phase was noticeable in the middle region. It was known that Er_2O_3 precipitates in certain regions during sintering and forms $Er_3Al_5O_{12}$ (erbium aluminate garnet phase) and this phase causes heterogeneous distribution in the microstructure. The intense phase separation in the edge region suggests that this composition was sensitive to the sintering temperature and prone to surface phase segregation during sintering.

When fig. 3.106.e and fig. 3.106.f of the ATZ-5Ce composition was examined and it was seen that the effect of CeO_2 addition on the microstructure was different from that of ATZ-5Er. A relatively more homogeneous structure was formed in the middle region, but distinct phase separations were observed at the grain boundaries. It was seen that there was a distinct sintering layer when the edge region was examined. The $CeAlO_3$ perovskite phase condenses on the surface forming a different layer during sintering. In the edge region of the ATZ-5Ce, a layered structure was formed on the surface that underwent phase transformation with the sintering atmosphere.

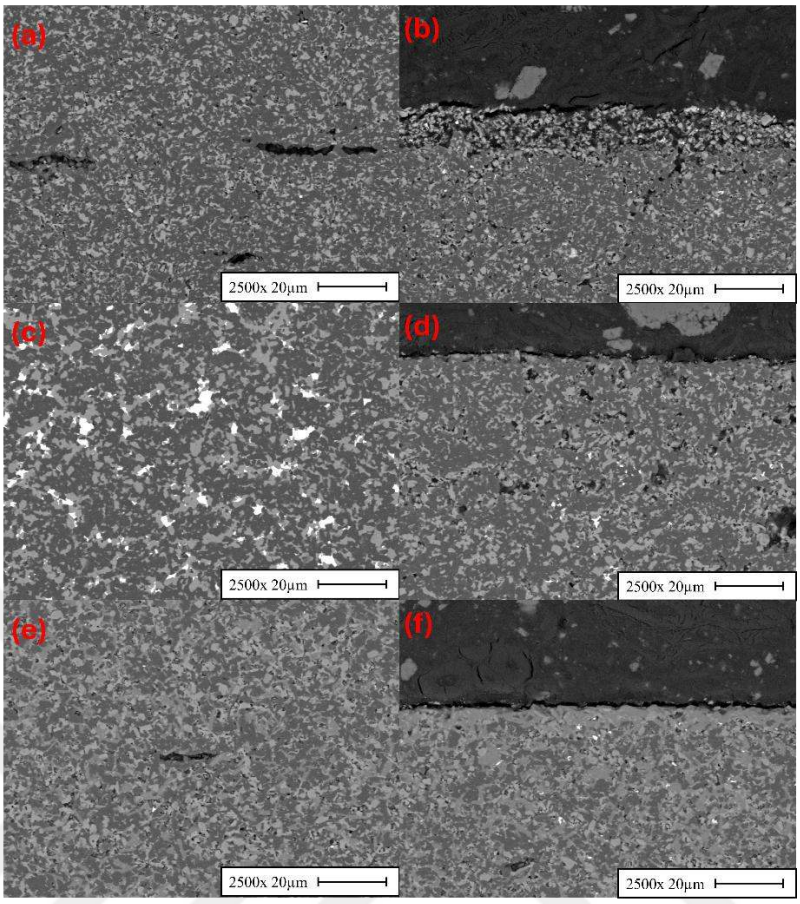

Figure 3.106. *Representative backscattered SEM images taken from polished surface of ATZ, ATZ-5Er and ATZ-5Ce compositions sintered at 1800 °C*

Distinct phase separations and concentrated phases in the edge regions were observed in the ATZ-5Er and ATZ-5Ce compositions, while the ATZ composition exhibited a relatively more homogeneous structure after sintering with GPS at 1800 °C. The Er_2O_3 additive precipitated in certain regions during sintering affecting the homogeneity of the microstructure and phase segregation. Although the CeO_2 additive provides a more stable structure, the different layers in the edge region were noticeable. These results indicate that rare earth oxides may cause surface phase reactions during sintering and determining the optimum temperature and atmosphere conditions was critical.

The relative densities of the compositions that sintered at 1800 °C were given in Table 3.37. The relative density of ATZ composition was 90.80%. This indicates that full densification was not achieved during sintering and the compositions still contain porosity. This shows that the sintering temperature was not sufficient for ATZ. The ATZ-5Er composition reached the highest relative density with 97.77%. Er_2O_3 addition

positively affected the sintering process. It also contributed to the reduction of porosity in the ATZ. The ATZ-5Ce reached a relative density of 91.24%, which was higher than ATZ but lower than ATZ-5Er. This indicates that CeO_2 addition provides a certain contribution to the sintering process but was not sufficient for complete densification.

Table 3.37. *Relative densities of compositions sintered at 1800 °C*

Compositions	Relative Density (%)
ATZ	90.80
ATZ-5Er	97.77
ATZ-5Ce	91.24

In fig. 3.107 compares the hardness and fracture toughness values of ATZ, ATZ-5Er and ATZ-5Ce compositions sintered with GPS at 1800 °C. When evaluated in terms of hardness the ATZ-5Er composition reached the highest hardness value (~20 GPa). This demonstrated that adding Er_2O_3 into the ATZ matrix strengthened the grain boundaries and increased the density. ATZ and ATZ-5Ce compositions showed lower hardness values (~13-14 GPa). Since it was known from previous data that ATZ contains high porosity at low sintering temperature, low hardness was an expected result. The hardness value of ATZ-5Ce was like ATZ and the additive did not significantly increase the hardness. This can be explained by the formation of the $CeAlO_3$ perovskite phase and porosity formation at the grain boundaries.

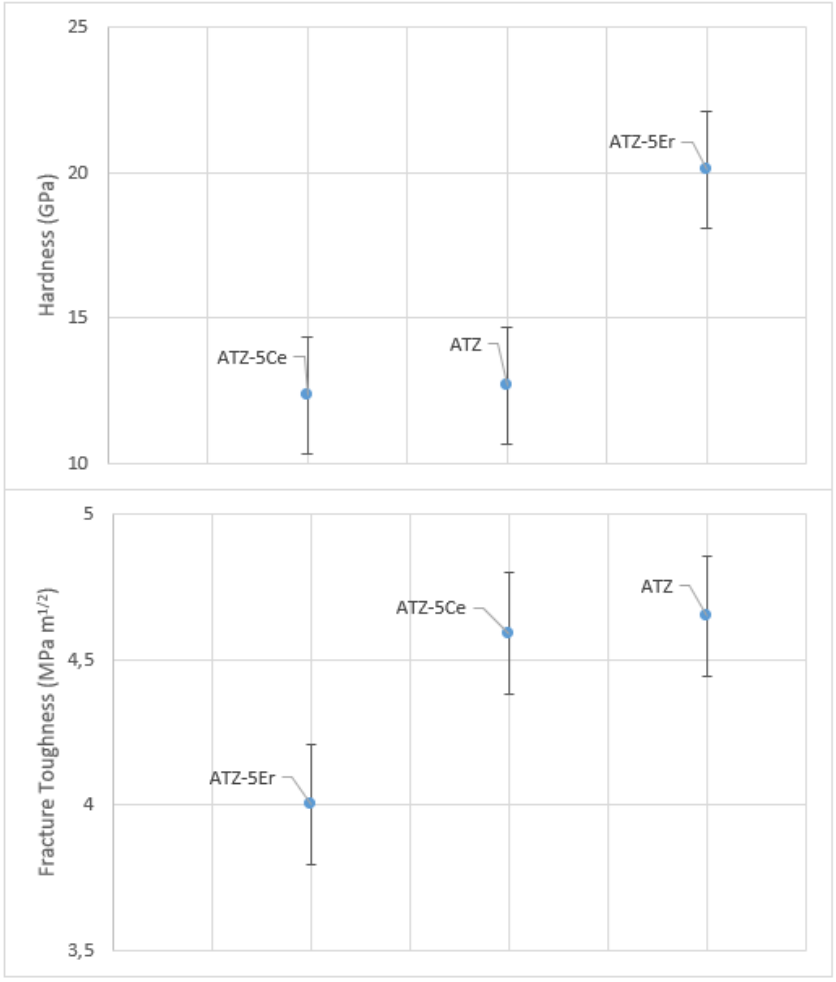

Figure 3.107. *Representative hardness and fracture toughness of ATZ, ATZ-5Er and ATZ-5Ce sintered at 1800 °C*

When evaluated in terms of fracture toughness, ATZ has the highest fracture toughness value (~4.8 MPa $m^{1/2}$). The ATZ-5Ce composition exhibited similar fracture toughness (~4.5 MPa $m^{1/2}$). However, ATZ-5Er showed the lowest fracture toughness value (~4 MPa $m^{1/2}$). The relatively higher toughness of ATZ can be explained by the fact that the pores formed due to low density deflect crack propagation. However, the presence of the $CeAlO_3$ phase in ATZ-5Ce created partial weakness at grain boundaries. It did not completely negatively affect the fracture toughness. In ATZ-5Er, although the hardness was high the low fracture toughness shows that the second phase ($Er_3Al_5O_{12}$) formed after sintering makes the structure more brittle.

3.7.2. 1900 °C GPS sintered ATZ, ATZ-5Er, ATZ-5Ce

Fig. 3.108 shows the positions of ATZ, ATZ-5Er and ATZ-5Ce compositions in the graphite crucible during sintering with GPS at 1900 °C. The ATZ, ATZ-5Er and ATZ-5Ce compositions were pressed at 230 MPa, 183 MPa and 228 MPa, respectively.

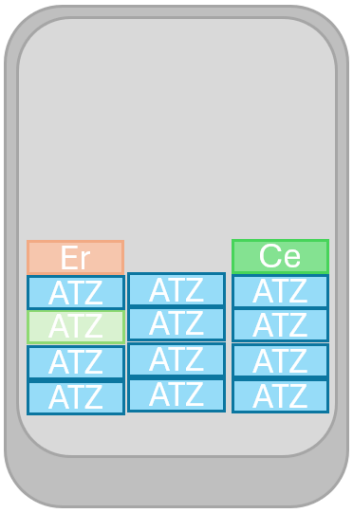

Figure 3.108. *Schematic representation of samples in a graphite crucible*

In fig. 3.109 shows backscattered SEM images of compositions sintered at 1900 °C at 2500x magnification. Fig. 3.109.a shows the middle part of the ATZ, fig. 3.109.b shows the edge part of the ATZ, fig. 3.109.c shows the middle part of the ATZ-5Er, fig. 3.109.d shows the edge part of the ATZ-5Er, fig. 3.109.e shows the middle part of the ATZ-5Ce and fig. 3.109.f shows the edge part of the ATZ-5Ce composition.

When fig. 3.109.a and fig. 3.109.b were examined, it was seen that the microstructure in the middle part was relatively homogeneous but there were obvious pores and cracks. Especially in the fig. 3.109.b porosity occurred due to press failure.

When fig. 3.109.c and fig. 3.109.d were examined and the porosity in the inner part decreases compared to ATZ. The addition of Er_2O_3 to the sintering process improved the density. However, it was noteworthy that there was still a significant phase separation in the edge region (fig. 3.109.d).

Fig. 3.109.e and fig. 3.109.f shows the most obvious differences in terms of microstructure. Some large pores and intense phase separation were noteworthy while a homogeneous structure was observed in the middle region (fig. 3.109.e). However, the most noticeable difference was seen in the edge region (fig. 3.109.f). Excessive sintering

and flow occurred in the edge region, which may be related to the $CeAlO_3$ phase being unstable at high temperatures and disrupting the sintering mechanism by forming a liquid phase. Such phase separations may adversely affect the mechanical improvement of the material.

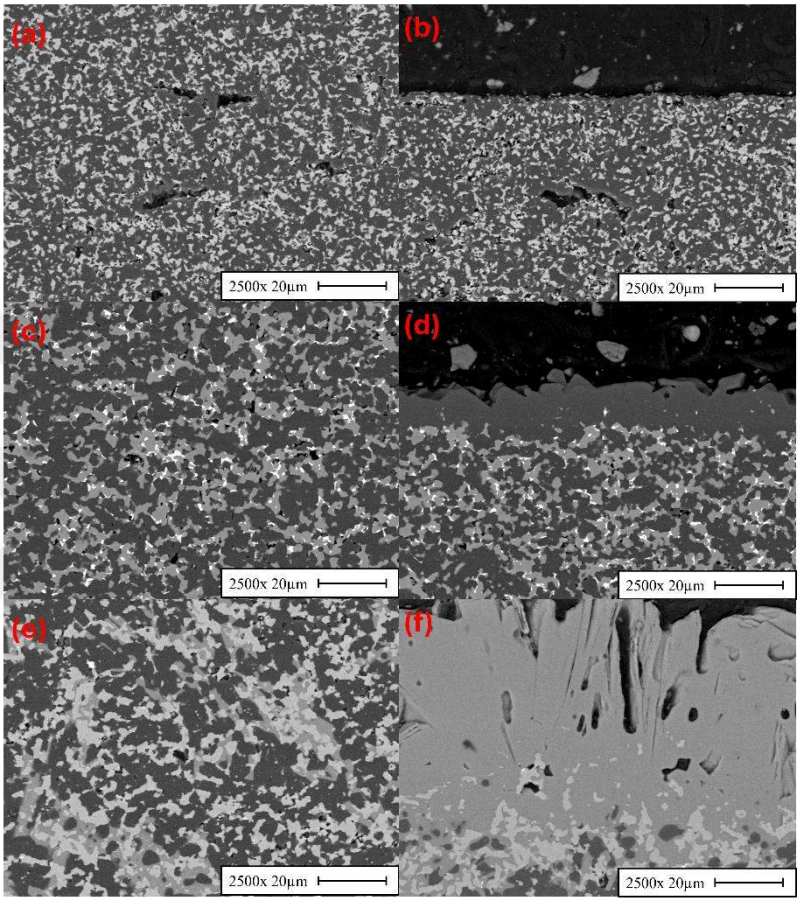

Figure 3.109. *Representative backscattered SEM images taken from polished surface of ATZ, ATZ-5Er and ATZ-5Ce compositions sintered at 1900 °C*

These results show that Er_2O_3 addition improves the sintering process, but attention should be paid to phase separation. Also, it shows that the CeO_2 additive was unstable above certain temperatures and may negatively affect the structural integrity. It was understood that the ATZ composition has densification problems even at high temperatures and requires more optimized parameters for pressing.

The density of ATZ increased from 90.80% at 1800 °C to 96.27% at 1900 °C. This increase shows that temperature plays an important role in closing the pores. The density of ATZ-5Er increased from 97.77% at 1800 °C to 98.36% at 1900 °C. This shows that Er_2O_3 addition increases the sintering efficiency at high temperatures and significantly

reduces the porosity. The density of ATZ-5Ce increased from 91.24% at 1800 °C to 94.47% at 1900 °C. This increase shows that CeO_2 increases densification to a certain extent during the sintering process but was still not as successful as other additives.

Table 3.38. *Relative densities of compositions sintered with full crucible at 1900 °C*

Compositions	Relative Density (%)
ATZ	96.27
ATZ-5Er	98.36
ATZ-5Ce	94.47

In fig. 3.110 the hardness and fracture toughness values of ATZ, ATZ-5Er and ATZ-5Ce compositions sintered with GPS at 1900 °C were compared. As seen in fig. 3.110, ATZ-5Er reached the highest hardness value (~20GPa). Er_2O_3 addition increased the sintering efficiency and created a denser structure. The ATZ composition exhibited a lower hardness value (~18 GPa) than ATZ-5Er when sintered at 1900 °C. ATZ-5Ce has the lowest hardness value (~15-16 GPa). One of the most important reasons for the low hardness of ATZ-5Ce was that the abnormal grains formed during phase separation and sintering negatively affect the integrity of the composite.

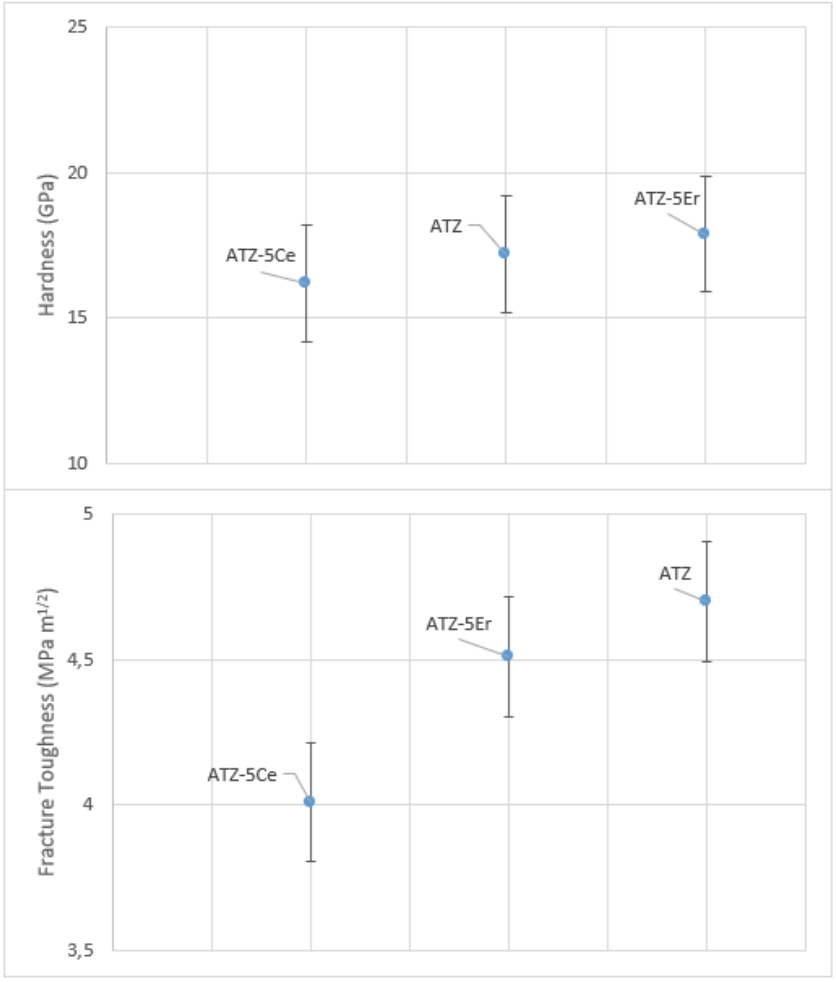

Figure 3.110. *Representative hardness and fracture toughness of ATZ, ATZ-5Er and ATZ-5Ce sintered at 1900 °C*

The ATZ has the highest fracture toughness value (~4.8 MPa $m^{1/2}$). ATZ-5Er has ~4.4-4.5 MPa $m^{1/2}$ and exhibits slightly lower fracture toughness than ATZ. ATZ-5Ce has the lowest fracture toughness with ~4.0-4.1 MPa $m^{1/2}$. The most important reason why the fracture toughness of ATZ-5Ce was the lowest was that the composite becomes brittle due to phase separation and liquid phase flow in the edge regions. Although ATZ-5Er increased the hardness it did not provide as high fracture toughness as ATZ. This was because high density and hardness were inversely proportional to fracture toughness.

3.7.3. 1900 °C GPS sintered at isolated ATZ, ATZ-5Er, ATZ-5Ce

Fig. 3.111 shows the positions of ATZ, ATZ-5Er and ATZ-5Ce compositions in the graphite crucible during sintering with GPS at 1900 °C. The ATZ, ATZ-5Er and ATZ-5Ce compositions were pressed at 448 MPa, 132 MPa and 238 MPa, respectively. The

pressure difference was due to the different geometries of the samples. The green density of all samples was around 60%.

Figure 3.111. *Schematic representation of samples in a graphite crucible sintered at 1900 °C.*

In fig. 3.112 backscattered SEM images of compositions sintered at 1900 °C at 2500x magnification were given. Fig. 3.112.a shows the middle part of the ATZ, fig. 3.112.b shows the edge part of the ATZ, fig. 3.112.c shows the middle part of the ATZ-5Er, fig. 3.112.d shows the edge part of the ATZ-5Er, fig. 3.112.e shows the middle part of the ATZ-5Ce and fig. 3.112.f shows the edge part of the ATZ-5Ce composition.

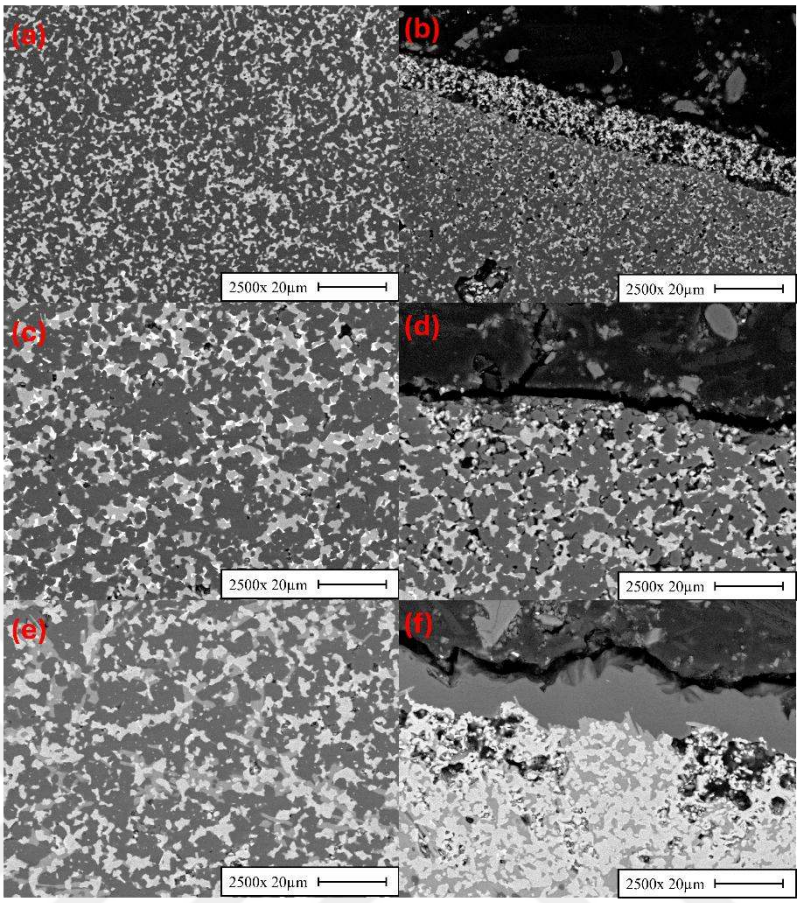

Figure 3.112. *Representative backscattered SEM images taken from polished surface of ATZ, ATZ-5Er and ATZ-5Ce compositions sintered at 1900 °C isolated position.*

The relative density values obtained because of the sintering process at 1900 °C with only one sample in the graphite crucible reveal important findings compared to previous studies. Especially in previous studies where more than one sample was placed in the same crucible at the same temperature, the ATZ reached a relative density of 96.27%, ATZ-5Er 98.36% and ATZ-5Ce 94.47% respectively. However, in this new arrangement ATZ reached 98.60%, ATZ-5Ce 98.20% and ATZ-5Er 97.20% respectively. As symbolized in fig. 3.111, each sample was isolated in the crucible without direct contact with the carbon sheet. This arrangement ensured the gas flow was regular and undesirable chemical reactions with the carbon sheet were prevented. As a result, this new configuration generally provided more effective densification and a more stable structure development.

Table 3.39. *Relative densities of compositions sintered at 1900 °C*

Compositions	Relative Density (%)
ATZ	98.60
ATZ-5Er	97.20
ATZ-5Ce	98.20

In fig. 3.113 the hardness and fracture toughness values of ATZ, ATZ-5Er and ATZ-5Ce compositions sintered with GPS at 1900 °C were compared. As seen in fig. 3.113, ATZ reached the highest hardness value (~19 GPa) and was followed by ATZ-5Er (~17 GPa) and ATZ-5Ce (~17 GPa). This ranking in hardness shows that the undoped ATZ develops a more compact and harder structure, while the additives partially reduce the hardness. This can be explained by the fact that the additives change the structural homogeneity by adding new phases to the matrix.

The table changes when the fracture toughness values were examined. ATZ-5Ce composition reached the highest fracture toughness of about 5.2 MPa $m^{1/2}$. This value was followed by ATZ (~5.0 MPa $m^{1/2}$) and ATZ-5Er (~4.1 MPa $m^{1/2}$). CeO_2 addition positively affected on toughness despite some partial porosity as seen in previous SEM observations.

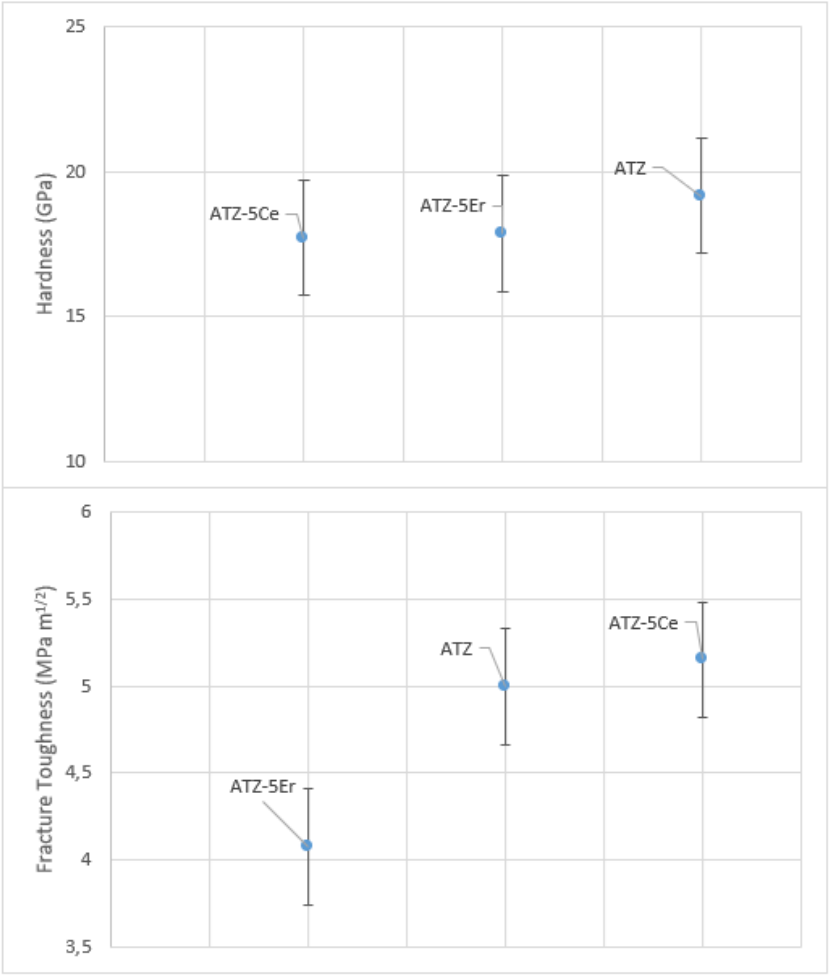

Figure 3.113. *Representative hardness and fracture toughness of ATZ, ATZ-5Er and ATZ-5Ce sintered at 1900 °C*

Isolated sintering of the samples provided an overall improvement in mechanical properties as well as density. However, this improvement developed in different directions depending on the type of contribution. While CeO_2 addition increased fracture toughness, Er_2O_3 addition affected the hardness relatively less but kept the toughness at a limited level.

3.7.4. 1900 °C GPS sintered ATZ, ATZ-5Er, ATZ-5Ce additive ones between ATZs

In fig. 3.114, it was seen that direct contact with the ground in the graphite crucible was cut off by dummy samples and the compositions containing additives were positioned between the ATZ without additives and the dummies.

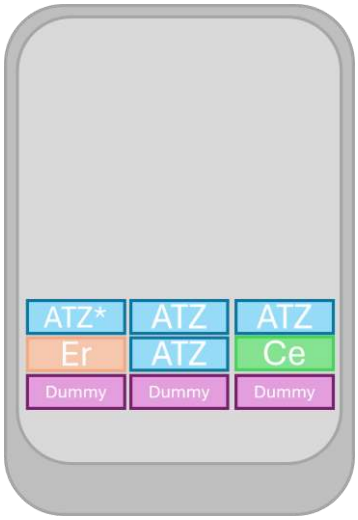

Figure 3.114. *Schematic representation of samples in a graphite crucible sintered at 1900 °C.*

In fig. 3.115 backscattered SEM images of compositions sintered at 1900 °C at 2500x magnification were given. Fig. 3.115.a shows the middle part of the ATZ, fig. 3.115.b shows the edge part of the ATZ, fig. 3.115.c shows the middle part of the ATZ-5Er, fig. 3.115.d shows the edge part of the ATZ-5Er, fig. 3.115.e shows the middle part of the ATZ-5Ce and fig. 3.115.f shows the edge part of the ATZ-5Ce composition.

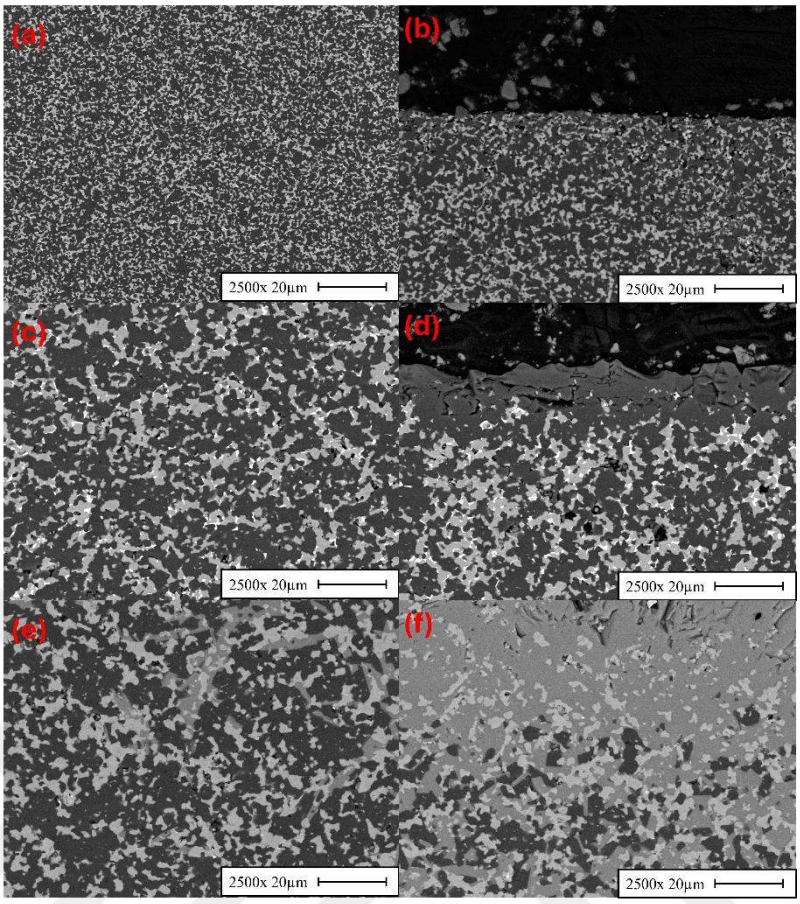

Figure 3.115. *Representative backscattered SEM images taken from polished surface of ATZ, ATZ-5Er and ATZ-5Ce compositions sintered at 1900 °C between positions.*

In Table 3.40, the obtained relative density values show that the sintering success was quite high. ATZ composition reached almost full density with 99.47%. This value shows that the microstructure has minimum porosity and highly optimized sintering conditions. ATZ-5Er composition also exhibited high density with 98.76%. The 98.35% value measured for ATZ-5Ce was quite high but it suggests that the CeO_2 additive can provide less density than Er_2O_3. These results show that dummy samples play an important role in balancing the heat transfer during sintering and preventing the direct interaction of the additive contained samples with the graphite surface.

Table 3.40. *Relative densities of compositions sintered with dummy at 1900 °C*

Compositions	Relative Density (%)
ATZ	99.47
ATZ-5Er	98.76
ATZ-5Ce	98.35

In fig. 3.116 the hardness and fracture toughness obtained in between sintering setup were compared. As seen in fig. 3.116, the ATZ-5Er sample reached the highest hardness value (~20 GPa). The ATZ composition, although it does not contain additives, shows a very high hardness of approximately 19 GPa. This value has increased compared to the results in the previous setups and shows that the appropriate sintering environment was effective. The ATZ-5Ce sample shows a slightly lower hardness (~18 GPa) than the other two compositions due to the CeO_2 doping, causing phase separation or edge-diffusion induced structural porosity at high temperatures.

When the fracture toughness values were examined, the ATZ-5Ce sample exhibits the highest value (~5.5 MPa $m^{1/2}$). This remarkable result indicates that the CeO_2 additive activates crack deflection or crack bridging mechanisms in the microstructure. The ATZ-5Er composition ranks second with approximately 5.2 MPa $m^{1/2}$. Although this value was quite good, its advantage in hardness was not fully reflected in fracture toughness. The ATZ composition has the lowest fracture toughness (~4.6 MPa $m^{1/2}$). It still exhibits proper performance compared to many ATZ ceramics in the literature.

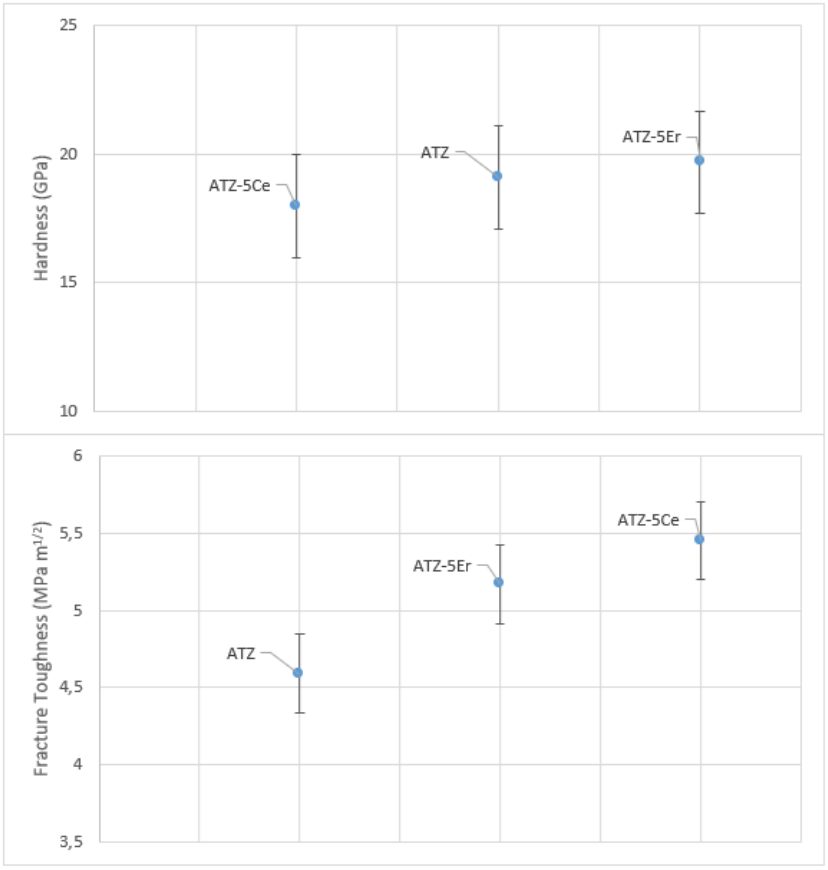

Figure 3.116. *Representative hardness and fracture toughness of ATZ, ATZ-5Er and ATZ-5Ce sintered at 1900 °C between positions.*

This sintering setup ensured that the ceramics containing additives were isolated from the effects of the high temperature crucible and sintered in a homogeneous and inert environment. It was observed that the values of both hardness and fracture toughness improved and the effects of the additives became clearer. ATZ-5Er provided the best performance in hardness, while ATZ-5Ce provided the highest value of fracture toughness. This shows that each additive type affects the mechanical properties with different additive mechanisms and the optimization may vary depending on the additive type and the sintering atmosphere. In conclusion, optimizing sintering in graphite with careful placement allowed the additive oxides to function fully and led to significant improvement in mechanical properties.

4. CONCLUSIONS

The characterization of the commercial products study examined three different commercial ceramic inserts (C1, C2 and C3). SEM analyses determined that the C2 product exhibited a homogeneous, fine-grained and regular TiC particle distribution, resulting in the highest hardness value among the products examined. The C1 sample demonstrated the highest fracture toughness despite its coarser and heterogeneous microstructure, while the C3 sample showed high hardness but lower fracture toughness. These results indicate that variations in microstructural and chemical properties directly affect mechanical performance and can explain differences in industrial preferences.

In the "Determination of Al_2O_3 and TiC Content in Composition" section, the mechanical properties, microstructural behavior and sintering processes of Al_2O_3–TiC composites were investigated comparatively with similar studies in the literature. Compositions with four different TiC contents (20–55 wt.%) were prepared. The analyses indicated that the particle size of the starting powders played a significant role in achieving a homogeneous microstructure. The SPS method provided advantages over the HP method frequently used in the literature. Density values obtained were close to theoretical values. T20 and T30 compositions with lower TiC contents achieved relatively higher densities and limited pore formation. Mechanical tests showed that the highest hardness (~20.85 GPa) and fracture toughness (~5.11 MPa $m^{1/2}$) values were achieved in the T55 composition. These results indicate that varying TiC contents significantly affect the mechanical and microstructural properties of the composites.

The study carried out under the title of "Effects of Sintering Parameters" evaluated the effects of different sintering parameters on the density, microstructure and mechanical properties of Al_2O_3-TiC composites were evaluated. Samples sintered at 1875 °C and 1900 °C for varying durations were analyzed. Higher temperatures and extended sintering times generally led to increased density and a more homogeneous microstructure. Samples sintered at 1900 °C for 60 minutes provided the most favorable results in terms of density and microstructural homogeneity. Additionally, the addition of 3.5 wt.% and 5 wt.% ZrO_2 positively influenced the sintering process by increasing density and reducing porosity. These findings suggest that ZrO_2 addition enhances mechanical properties and microstructural stability by controlling grain growth. Proper optimization of sintering temperature, duration and additive content was therefore critical for Al_2O_3–TiC composites.

In the section titled “Effect of Pressing Pressure and Sintering Crucible,” the effects of different pressing pressures and sintering crucible materials on density, microstructure and mechanical properties of Al_2O_3–TiC–3.5 wt.% ZrO_2 composites were investigated. A significant increase in green density values was observed with increasing pressing pressure. Density and microstructural homogeneity improved markedly at 350 MPa, while pressures above 500 MPa slightly decreased density and potential microcrack formation. In sintering studies using BN and graphite crucibles, graphite crucibles exhibited lower chemical interaction with the samples. Thinner and more homogeneous layers formed in samples sintered in graphite crucibles. Overall, an optimum pressing pressure in the 200–350 MPa range and graphite crucibles produced superior microstructure and high-density values.

In the study carried out under the title of “Prototype Production with GPS and Resintering” different sintering arrangements were investigated to improve the density and microstructural properties of ATZ composition. In the first stage, high densities were achieved in individual samples with the controlled use of carbon sheets. However, negative effects of increasing the amount of carbon sheets were observed in trials for prototype production. More positive results in terms of density were obtained by completely removing the carbon sheets and using dummy samples instead. Especially in samples reaching 99% relative density, high hardness (~20 GPa) and fracture toughness (~4.97 MPa $m^{1/2}$) values were achieved. These findings reveal that optimizing sample setups and using a carbon sheet in the sintering process was critical in improving ATZ composites’ performance.

In the section titled “Effect of Rare Earth Oxide Additives,” the addition of various rare earth oxides (Er_2O_3, Yb_2O_3, Y_2O_3, Sm_2O_3, CeO_2) to ATZ composites was examined to improve mechanical properties and microstructural behavior. Composites containing these oxides at 3.5 wt.% and 5 wt.% were evaluated for their effects on sintering kinetics, grain growth and density. Analyses indicated that samples sintered with the SPS method achieved higher densities and superior microstructures than those produced by GPS. However, increasing additive ratios led to higher porosity and more pronounced grain growth, particularly in GPS-sintered composites. Y_2O_3 and Yb_2O_3 additions initiated sintering at higher temperatures and enabled densification over a wide temperature range, while CeO_2 and Sm_2O_3 additions accelerated densification at lower temperatures within a narrower range. These findings indicate that the type and amount of REOs significantly

affect sintering behavior and mechanical properties and underscore the importance of careful additive optimization in material design.

In the study carried out under the title of “Granulated ATZ-5Er and ATZ-5Ce Sintered with GPS” the effects of sintering of granulated composites formed with 5 wt.% Er_2O_3 and CeO_2 additions to ATZ compositions by the GPS method on the density, microstructure and mechanical properties were investigated. Different effects of the additives were observed in the sintering processes carried out at 1800 °C and 1900 °C temperatures. Er_2O_3 doped (ATZ-5Er) composites exhibited high sintering efficiency and a dense microstructure, reaching the highest hardness values (~20 GPa). However, these composites have relatively lower values in terms of fracture toughness (~4 MPa $m^{1/2}$). In CeO_2 added (ATZ-5Ce) composites, it was observed that phase separation and large grain structures formed during sintering disrupted the integrity of the material and negatively affected the hardness (~15-16 GPa). However, it was determined that the liquid phase formed by the CeO_2 added increased the fracture toughness (~4.5 MPa $m^{1/2}$), especially despite the porosity in the edge regions. These results reveal that the type of rare earth oxides and the sintering temperature play a critical role in the mechanical properties and microstructure of ATZ composites prepared in granular form and sintered by the GPS method.

Generally evaluated, this study has revealed in detail the importance of different compositions, sintering parameters and additives used in improving the mechanical and microstructural properties of Al_2O_3-TiC based ceramics. Especially by adding rare earth oxides and applying different sintering methods, high-performance ceramic materials that can compete with conventional commercial products have been developed. These results highlight the importance of further research and optimization studies to improve the performance of ceramic inserts in industrial applications.

5. FURTHER WORKS

Future research should extend the current material development to actual machining trials. In particular, the optimized ATZ composition must be evaluated under representative industrial cutting conditions to assess tool life, wear mechanisms and workpiece surface finish. Due to their high hardness and wear resistance Al_2O_3-based ceramic tools are already used for machining hardened steels. Quantitative metrics such as flank a crater wear rate, cutting force and temperature and machined surface roughness must be measured under varying speeds and feeds and under dry versus lubricated conditions.

REFERENCES

Askeland, D. R., and Wright, W. J. (2016). *The Science and Engineering of Materials Seventh Edition.* Boston: Cengage Learning.

ASTM-311. (n.d.). *Standard test method for the density of powder metallurgy (PM) materials containing less than two percentage porosity.*

Ayas, E. (2003). *Al_2O_3-TiC/TiCN Kompozit Malzemelerin Üretim Yöntemleri.* Fen Bilimleri Enstitüsü Seramik Mühendisliği Anabilim Dalı.

Barsoum, M. W. (2020). *Fundamentals of Ceramics Second Edition.* CRC Press.

Bilgiç, B. Z. (2012, Haziran). Al_2O_3-ZrO_2-CeO_2 Kompozitlerinin Spark Plasma Sinterleme (SPS) Yöntemi ile Üretimi ve Karakterizasyonu. *Yüksek Lisans Tezi*. İstanbul, Türkiye: İstanbul Teknik Üniversitesi.

Cai, K., McLachlan, D., Axen, N., and Manyatsa, R. (2002). Preparation, microstructures and properties of Al_2O_3-TiC Composites. *Ceramic International*, 217-222.

Callister Jr, W. D., and Rethwisch, D. G. (2014). *Materials Science and Engineering An Introduction 9E.* John Wiley and Sons, Inc.

Carter, C. B., and Norton, M. G. (2007). *Ceramic Materials Science and Engineering* . Springer.

Chae, K. W., and Kim, D. Y. (1993). Effect of Y_2O_3 Additions on the Densification of Al_2O_3-TiC Composite. *Journal of American Ceramic Society*, 1857-1860.

Chang, C., Liu, Y., Guo, W.-M., Long, Y., Duan, X. M., Jia, D. C., and Lin, H. T. (2024). Effect of Al_2O_3-CeO_2 molar ratio on mechanical properties of SiC ceramics. *Ceramics International*, 5032-5037.

Charles, E., and Evans, A. (1976). Fracture toughness determination by indentation. *J. Am. Ceram. Soc.*, 371-372.

Chen, L., and Kny, E. (2000). Reaction hot-pressed sub-micro Al_2O_3+TiC ceramic composite. *International Journal of Refractory Metals & Hard Materials*, 163-167.

Chung, D. D. (2010). *Composite Materials Science and Applications Second Edition.* London: Springer-Verlag.

Cutler, R. A., and Hurford, A. C. (1988). Pressureless-sintered Al_2O_3-TiC Composites. *Materials Science and Engineering*, 183-192.

Deng, J., Can, T., and Sun, J. (2005). Microstructure and mechanical properties of hot-pressed Al_2O_3/TiC ceramic composites with the additions of solid lubricants. *Ceramic International*, 249-256.

Ezugwu, E., and Tang, S. (1995). Surface abuse when machining cast iron (G-17) and nickel-base superalloy (Inconel 718) with ceramic tools. *Journal of Materials Processing Technology*, 63-69.

Fabrichnaya, O., and Seifert, H. (2010). Thermodynamic assessment of the ZrO_2-Yb_2O_3-Al_2O_3 system. *CALPHAD: Computer Coupling of Phase Diagrams and Thermochemistry*, 206-214.

Fei, Y., Huang, C., Liu, H., and Zou, B. (2014). Mechanical properties of Al_2O_3-TiC-TiN ceramic tool materials. *Ceramic International*, 10205-10209.

Goldstein, A., and Singurindi, A. (2000). Al_2O_3/TiC Based Metal Cutting Tools by Microwave Sintering Followed by Hot Isostatic Pressing. *J. Am. Ceram. Soc.*, 1530-1532.

Grigoriev, S. N., Fedorov, S. V., and Hamdy, K. (2019). Materials, properties, manufacturing methods and cutting performance of innovative ceramic cutting tools - a review. *Manufacturing Rev*, 18.

Grigoriev, S. N., Volosova, M. A., Peretyagin, P. Y., Seleznev, A. E., Okunkova, A. A., and Smirnov, A. (2018). The Effect of TiC Additives on Mechanical and Electrical Properties of Al_2O_3 Ceramic. *Applied Sciences*, 2385.

Groover, M. P. (2010). *Fundamentals of Modern Manufacturing Materials, Processes, and Systems 4th edition.* John Wiley and Sons, Inc.

Guvenc, C. M., Toso, S., Ivanov, Y. P., Saleh, G., Balci, S., Divitini, G., and Manna, L. (2025). Breaking the boundaries of the Goldschmidt Tolerance Factor with ethylammonium lead iodide perovskite nanocrystals. *ACS Nano*, 1557-1565.

Herbell, T., and Glasgow, T. (1978). Effect of attrition milling on the reaction sintering of silicon nitride. *Ninetinth Annual Meeting of the American Ceramic Society*.

Karwa, D. R. (2006). *A Text Book of Machine Design.* New Delphi: Laxmi Publications Ltd.

Kasuriya, S., and Atong, D. (2006). Effect of sintering temperature and additives on properties of Al_2O_3-TiC composites. *Asian Symposium on Materials and Processing.* Bangkok, Thailand: The Japan Society of Mechanical Engineers.

Kingery, W. (1963). *Ceramic Fabrication Processes.* Cambridge: MIT Press.

Kulik, V., Kulik, A., Ramm, M., and Makarov, Y. (2004). Modeling of SiC-matrix composite formation by isothermal chemical vapor infiltration. *Journal of Crystal Growth*, 333-339.

Lakiza, S., and Lopato, L. (2006). Phase diagram of the alumina-zirconia-samaria system. *Journal of American Ceramic Society*, 3516-3521.

Lakiza, S., and Lopato, L. (2008). Phase diagram of the Al_2O_3-ZrO_2-Er_2O_3 system. *Journal of the European Ceramic Society*, 2389-2397.

Liu, N., Shi, M., Xu, Y., You, X., Ren, P., and Feng, J. (2004). Effect of starting powders size on the Al_2O_3-TiC composites. *International Journal of Refractory Metals & Hard Materials*, 265-269.

Lü L., L. M. (1995). Modeling of the mechanical-alloying process. *Journal of Materials Processing Technology*, 539-546.

Mao, D., Li, J., Guo, S., and Mao, Z. (1997). Study of abrasion behavior of an advanced Al_2O_3-TiC-Co ceramic. *Wear*, 153-159.

Meir, S., Kalabukhov, S., and Hayun, S. (2014). Low temperature spark plasma sintering of Al_2O_3-TiC composites. *Ceramic International*, 12187-12192.

Özerdem, E., and Ayas, E. (2015). Fabrication and microstructural stability of spark plasma sintered Al_2O_3/$Er_3Al_5O_{12}$ eutectic. *Ceramics International*, 12869-12877.

Rahaman, M. N. (2003). *Ceramic Processing and Sintering Second Edition.* New York: Marcel Dekker.

Richerson, D. W., and Lee, W. E. (2018). *Modern Ceramic Engineering Properties, Processing, and Use in Design.* New York: CRC Press.

Shackelford, J. F. (2023). *Introduction to Materials Science for Engineers Ninth Edition.* Pearson Education Limited.

Smith, W., and Hashemi, J. (2019). *Foundations of Materials Science and Engineering Sixth Edition.* McGraw-Hill Educations.

Sun, L., Zhou, C., Du, T., Wu, Z., Lei, Y., Li, J. and Wang, J. (2021). Directionally solidified $Al_2O_3/Er_3Al_5O_{12}$ and $Al_2O_3/Yb_3Al_5O_{12}$ eutectic ceramics prepared by optical floating zone melting. *Journal of Inorganic Materials*, 652-658.

Suryanarayana, C. (1999). *Non-Equilibrium Processing of Materials.* United Kingdom: Pergamon.

Suryanarayana, C. (2004). *Mechanical Alloying and Milling.* New York: Marcel Dekker.

Taşdemir, S., Yıldız, B. K., Işık, E., and Tür, Y. K. (2023). Exploring Microstructure and Bending Strength of Al_2O_3 Ceramics Doped with Sm_2O_3 Rare-Earth Oxide: Impact of Volume Ratios and Sintering Temperatures. *The Black Sea Journal of Sciences*, 1581-1594.

Tiwar, A., Gergardt, R. A., and Szutkowska, M. (2016). *Advanced Ceramic Materials.* New Jersey: John Wiley and Sons, Inc.

Wang, Z., Yi, M., Zheng, K., Chen, Z., Xiao, G., and Xu, C. (2023). Synthesis and characterization of Al_2O_3-TiC-ZrO_2 ceramics with intragranular nanostructure by spark plasma sintering. *Applied Ceramic Technology*.

Xing, Y., Deng, J., Li, S., Yue, H., Meng, R., and Gao, P. (2014). Cutting performance and wear characteristics of Al_2O_3/TiC ceramic cutting tools with WS_2/Zr soft-coating and nano-textures in dry cutting. *Wear*, 12-26.

Yang, H., and Roberts, S. (2005). Gas pressure sintering of Al_2O_3/TiCN composite. *Ceramic International*, 1073-1076.

Yin, Z., Huang, C., Yuan, J., Zou, B., Liu, H., and Zhu, H. (2015). Cutting performance and life prediction of an Al_2O_3/TiC micro-nano-composite ceramic tool when machining austenitic stainless steel. *Ceramic International*(41), 7059-7065.

Yin, Z., Huang, C., Zou, B., Liu, H., and Zhu, H. (2013). Preparation and characterization of Al_2O_3/TiC micro-nano-composite ceramic tool materials. *Ceramic International*, 4253-4262.

You, X., Si, T., Liu, N., Ren, P., Xu, Y., and Feng, J. (2005). Effect of grain size on thermal shock resistance of Al_2O_3-TiC ceramics. *Ceramics International*, 33-38.

Youssef, H. A. (2016). *Machining of Stainless Steels and Super Alloys Traditional and Non Traditional.* Alexandria: John Wiley and Sons, Ltd.

Youssef, H. A., and El-Hofy, H. (2008). *Machining Technology Machine Tools and Operations.* CRC Press.

Zhang, C., Ling, G., and Li, J. (2005). Ultra-toughened Al_2O_3-TiC-Co ceramic. *Composites Part A: applied science and manufacturing*, 715-718.

Zhang, Z., Ai, Y., Zhong, X., Zhuang, Y., Sheng, J., Ni, J. and Yang, K. (2022). Formation mechanism of Al_2O_3-YAG amorphous ceramic coating deposited via atmospheric plasma spraying. *International Journal of Applied Ceramic Technology*, 1518-1528.

Zmak, I., Jozic, S., Curkovic, L., and Filetin, T. (2025). Alumina-Based Cutting Tools - A Review of Recent Progress. *Materials*, 2813.

CURRICULUM VITAE

ORCID ID: 0009-0002-8745-8534

Name Surname : Ahmet Oğuzhan Turhan

Foreign Language : English

Education and Professional Background:

- 2012-2017, Adnan Menderes University, Engineering Department, Mechanical Engineering
- 2017-2018, Purchasing officer, Schott Orim Cam San. Ve Tic. A.Ş.
- 2018-2018, Import officer, Etimag Etiket Matbacılık Ambalaj San. ve Tic. A.Ş.
- 2019-2024, 2244 Industrial PhD scholarship, TÜBİTAK – MDA İleri Teknoloji Seramik A.Ş.
- 2024-, Mechanical engineer, MDA İleri Teknoloji Seramik A.Ş.

Publications and/or Scientific/Artistic Activities:

- 2024, Oral and Poster presentation, IMMC2024